Centre for Astrophysics Research
Department of Physics, Astronomy and Mathematics
School of Physics, Engineering and Computer Science
University of Hertfordshire

The Nature of Compact Sources Selected by LOFAR

Author:

Jones CHILUFYA

Supervisor:

Professor Martin John HARDCASTLE

Submitted to the University of Hertfordshire in partial fulfilment of the degree of Master of Science by Research.

November 2022

Abstract

Radio-loud active galactic nuclei (RLAGN) produce jets on large scales heating their local environments and preventing the hot phase of baryonic matter from cooling hence slowing or halting galaxy formation and evolution; a model popularly known as AGN feedback. To understand this model, new views of low-luminosity compact RLAGN inhabiting massive galaxies have been obtained using the new LOw Frequency ARray (LOFAR) northern-sky radio survey LoTSS (LOFAR Two Metre Sky Survey) to study RLAGN in the local Universe at low frequencies (150 MHz). In this thesis, I investigate low-luminosity compact RLAGN selected from LoTSS first Data Release (DR1) in an attempt to reveal their radio morphologies and the physical scales at which they affect the inter-galactic medium (IGM) of the host galaxy on sub-kpc scales. We have conservatively selected 55 low-luminosity compact RLAGN based on LoTSS DR1 within redshift range $0.03 < z < 0.1$. I show using high-frequency Jansky Very Large Array (VLA) observations that only 9 out of 55 objects show extended radio emission ($1-3$ kpc), 43 are compact at the limiting angular resolution of 0.35 arcsec (corresponding to projected maximum physical sizes of < 1 kpc), while 3 are undetected. The extended objects display a wide range of radio morphologies on smaller angular scales: doubles (3), two-sided jets (3), one-sided jets (2), and complex (1). I discuss their radio spectra which range from steep to flat and/or inverted radio spectra ($-1.31 < \alpha < 0.36$) and span the range seen in various compact RLAGN such as compact symmetric objects (CSOs), compact steep spectrum (CSS) sources, and gigahertz peaked-spectrum (GPS) sources. Assuming synchrotron self-absorption (SSA) models for flat and/or inverted radio spectrum sources, I predict the physical sizes of 35 RLAGN to be between $2-53$ pc. On their position on the power-linear size ($P - D$) diagram, we see that these objects populate the bottom left lower-end of the diagram; this position corresponds to the low-radio power CSOs. Finally, I compare their radio properties with those of the Fanaroff-Riley class 0 ('FR0') sources. Interestingly, some of the compact RLAGN presented in this thesis show extended radio emission in the second Data Release (DR2) images; these appear to be in fact the radio cores of low-luminosity yet extended Fanaroff-Riley (FRI/FRII) sources that could populate the right-lower end of the $P - D$ diagram, limited by LOFAR's surface brightness. Could we be underestimating the sizes of some of these compact objects? Continued VLBI observations of LOFAR sources could help us answer this question, which in turn will help us further understand AGN feedback.

DECLARATION

I declare that

1. No part of this work is being submitted concurrently for another award of the University or any other awarding body or institution. This thesis contains a substantial body of work that has not previously been submitted successfully for an award of the University or any other awarding body or institution.
2. Except where indicated otherwise in the submission, the submission is my own work and has not previously been submitted successfully for any award.
3. The work contained in this thesis is original and was supervised by Professor Martin John Hardcastle of the University of Hertfordshire at the Centre for Astrophysics Research (CAR).

Jones Chilufya

"My goal is simple. It is a complete understanding of the universe, why it is as it is, and why it exists at all." – Stephen Hawking.

Acknowledgments

First and foremost, I would like to thank my principal supervisor, Prof. Martin Hardcastle, for allowing me to kick-start my career in astronomy. These works could not have been possible without him. My sincere gratitude goes to him for being patient and taking the time out of his busy schedule to sit down with me and explain basic concepts throughout my studies. In the same capacity, I would like to thank Dr. Jonathon Pierce, particularly during my earlier work with CASA.

Secondly, I would like to acknowledge the financial support of the Newton-funded "Development in Africa with Radio Astronomy" (DARA)[1] which made my stay and studies in the UK comfortable despite the earlier funding challenges due to the COVID-19 pandemic.

Finally, I would like to express my sincere gratitude to my parents Maggie Mwelwa- and Peter Chilufya, for always sharing their unprecedented support and wisdom in all facets of life. To them, I am forever indebted. *Lesa alemipala nokumicingilila mulifyonse.*

I dedicate this thesis to my late siblings Erika (b. 1985); Chiti (b. 1987); Chikombola (b. 1993); and Morris Ng'andwe (b. 2000). I love you and miss you guys!

Jones Chilufya

[1] https://www.dara-project.org/

Table of Contents

List of Figures

List of Tables

Chapter 1

Introduction

1.1 Motivation

Since the emergence of radio astronomy in the 20th century (Jansky, 1933), radio observations have revealed a large number of previously unknown phenomena. In particular, they allowed the study of celestial objects such as Active Galactic Nuclei (AGNs), revealing phenomena at radio wavelengths not visible at any other wavelength (e.g. Peterson, 1997). Since the discovery of the most common class of AGNs by Seyfert (1943), AGNs have been found to be among the most powerful objects in the observable universe, with $\sim$10% of galaxies emitting extremely intense light at their centres (e.g. Peterson, 1997; Ho et al., 1997; Krolik, 1999) over portions of the electromagnetic spectrum. This phenomenon is driven by in-falling material onto a super-massive black hole (SMBH; e.g. Krolik, 1999; Di Matteo et al., 2003) centre. In terms of their radio properties, AGNs can be classed either as radio-loud AGNs (RLAGN) or radio-quiet AGNs (RQAGN) (e.g. Begelman et al., 1984; Kellermann et al., 1989). The observed distinction between the two subsets of AGN populations is characterised by their radio luminosities, jets, and the lobes they inflate. RLAGN produce these properties on larger scales, whereas the production of jets and lobes in RQAGN is normally thought to be almost negligible (e.g Wilson and Colbert, 1995; Lin et al., 2010; Panessa et al., 2019). The radio emission from these jets in RLAGN (collectively radio galaxies, blazars, and radio-loud quasars) is a result of the synchrotron process (Burbidge, 1956). The radio morphology of the emission is mostly determined by the interaction of jets and the environments in which they propagate extending over the host galaxy on kiloparsec (kpc) scales and sometimes propagating to much larger distances beyond the galaxy they inhabit out to megaparsec (Mpc) scales (e.g. Willis et al., 1974; Ghisellini et al., 1993; Machalski et al., 2008; Delhaize et al., 2021).

The first observation of emission resulting from a jet (Curtis, 1918) paved the way for extensive stud-

ies of RLAGN's jets and the effects they have on their environments. The jets from powerful RLAGN ($L_{1.4} > 10^{25}$ W Hz^{-1}) are considered key to understanding many astrophysical phenomena such as in their role in the epoch of reionization (e.g. Fan et al., 2006; Hassan et al., 2017; Bosch-Ramon, 2018), understanding the physics at the centre of a SMBH (e.g. Brandt and Alexander, 2010; Meier, 2012), testing models of general relativity (e.g. Blandford and Narayan, 1992; Valtonen et al., 2008), understanding the inter-galactic medium (IGM) in the early universe (e.g. Barkana and Loeb, 2007), probing the nature of dark matter (e.g. Gorchtein et al., 2010; Peirani et al., 2017), and, most important to our context, in the understanding of the so-called AGN feedback. Feedback models are important to modern models of galaxy formation and evolution (e.g. Croton et al., 2006; Fabian, 2012; Hardcastle and Croston, 2020) as they are thought to provide the energy required to stop or slow massive galaxies from forming by heating their local environments thus preventing the cooling of the hot gas responsible for star formation (SF).

To test AGN feedback models, a clear understanding of RLAGN is required from high flux density populations down to low flux density populations as well as from the local Universe out to high redshifts. The invention of high-resolution, highly sensitive telescopes such as the Karl Jansky Very Large Array (VLA) and the LOw Frequency ARray (LOFAR; van Haarlem et al., 2013) will play a crucial role in studying faint RLAGN. New views of RLAGN populations are expected to be provided by sky surveys such as the MeerKAT International GHz Tiered Extra-galactic Exploration survey (MIGHTEE; Jarvis et al., 2016), the Very Large Array Sky Survey (VLASS; Villarreal Hernández and Andernach, 2018), and the LOFAR survey of the Northern sky, the LOFAR Two-metre Sky Survey (LoTSS; Shimwell et al., 2019). LoTSS (currently the radio survey with the largest number of catalogued sources) offers high-sensitivity and high-resolution imaging of extragalactic sources both of star-forming galaxies (SFGs) and RLAGN. LOFAR's new generation capabilities have allowed for the study of RLAGN's structures at much lower frequencies, providing a high population of low-luminosity RLAGN.

1.2 This thesis

In this thesis, my main focus is the study of low-luminosity RLAGN; I take a systematic look at the LOFAR AGN population.

In Chapter 2, I review the general literature on AGNs and discuss both theoretical and observational aspects relevant to the subject matter, whereas Chapter 3 is concerned with the methodology in the reduction and calibration of the VLA data used in the thesis.

I investigate (Chapter 4) low-luminosity compact RLAGN selected from the LOFAR AGN population based on LoTSS DR1 using VLA observations, and discuss their nature with respect to various compact RLAGN such as CSO, GPS, CSS, and FR0 sources.

In Chapter 5, I discuss VLA objects showing extended radio emission in LoTSS DR2 images. I make necessary conclusions in the final Chapter and plan follow-up science (Chapter 6).

Throughout this thesis, I have assumed a ΛCDM cosmological model with cosmological parameters: $H_0 = 70$ km s^{-1} Mpc^{-1}; $\Omega_{m0} = 0.3$; $\Omega_{\Lambda 0} = 0.7$. The definition of the radio spectrum is given by $S_\nu \propto \nu^\alpha$.

Chapter 2

The literature

2.1 Active galaxies

The observable universe is populated by powerful, luminous, and energetic objects amongst which are AGNs. These objects dominate the electromagnetic (EM) spectrum in part or even across all wavelengths by their emission from their central compact regions, a quality that has attracted astronomers to study them extensively in multi-wavelength observations (e.g. radio, X-ray, and gamma-ray observations; Peterson, 1997; Beuchert, 2017). They are mainly driven by accretion onto the SMBH centre that is more than a million times heavier than our Sun (e.g. Woltjer, 1959; Liang and Liu, 2003; Peterson, 2015). Surrounding the SMBH is an accretion disk and perpendicular to this, relativistic outflows of plasma can form on either side in the presence of strong magnetic fields (e.g. Blandford et al., 2019). These relativistic plasma outflows are what are commonly termed *jets* and can propagate far beyond the galaxies they inhabit (e.g. Blandford et al., 2019). However, due to surface brightness limitations, only a small number ($\sim$10%) of galaxies are classified as AGNs, whereas the remaining number of galaxies are classified as 'normal' (e.g. Ho et al., 1997; Peterson, 1997); the total emitted energy from normal galaxies emanates from individual stars and can be observed in the visible and infrared (IR) wavelength range (e.g. Oemler, 1979). Besides high luminosities over a wide range of frequencies, AGNs' emission can be highly variable (e.g. Mushotzky, 1982; Ulrich et al., 1997) on large time scales down to small time scales (i.e. from years to hours) which proves the fact that their emission originates from compact regions (e.g. Krolik, 1999; Peterson, 2015).

In the radio range and as mentioned in Chapter 1, AGNs can be divided into RLAGN and RQAGN (e.g. Begelman et al., 1984; Kellermann et al., 1989). At least $\sim$10% of AGNs are RLAGN and are associated with the production of jets on larger scales [from parsec (pc) up to Mpc] while the remaining number

(∼90%) of AGNs are RQAGN; the production of jets in these objects is thought to be almost negligible (e.g. Kellermann et al., 1994, 2016). Here, it is important to classify RLAGN and one approach is to define it in terms of the radio-loudness (e.g. Kellermann et al., 1989). Kellermann et al. consider the ratio in luminosities (radio to optical; $R_{r-o} = L_r/L_o$) in selecting RLAGN over RQAGN. For instance, RLAGN are thought to be $\sim 10^3$ times brighter in terms of their radio emission ($R_{r-o} \sim 10-1000$) than RQAGN ($R_{r-o} \sim 0.1-10$) while the boundary between the two sources is set around $R_{r-o} \sim 10$ (Kellermann et al., 1994). Examples of RLAGN include radio galaxies, blazars, and radio-loud quasars while RQAGN are mostly Seyferts, some quasars (radio-quiet), and low-ionization nuclear emission-line regions (LINERs). For recent reviews on these objects see e.g. Heckman and Best (2014).

In this thesis, however, the definition of RLAGN for our objects (Chapter 4) is restricted to AGN with an excess of radio emission over what would be expected on the basis of their star formation rate (SFR) alone. Fig. 2.1 shows an AGN schematic and some of the features shown in this diagram are the groups in which AGNs can be placed; mainly based on their different emission properties (Krolik and Di Matteo, 2000). In principle, the type of AGN class we *see* depends on the angle of view (e.g. we are looking down on the jet with blazars), the production of significant emission, and the power of the central engine (e.g. Blandford and Rees, 1974; Rowan-Robinson, 1977; Scheuer and Readhead, 1979; Barthel, 1989; Antonucci and Miller, 1985).

In the next subsection, I discuss some AGN classes relevant to future discussions in this thesis and later, I briefly describe the AGN unification scheme in reference to Fig. 2.1.

2.1.1 Classes

Multi-wavelength observations have contributed significantly to the better understanding and exploration of AGNs as a whole. This is partly due to the thermal and non-thermal emissions from AGNs that dominate the electromagnetic spectrum (e.g. Begelman, 1994). In this section, I summarise different AGN classes i.e. Seyferts, blazars, quasars, LINERs, and radio galaxies. However, we should note that the distinction in AGN classes is unclear and their categories entirely depend on observational characteristics (particularly in the optical and radio regimes) such as their spectral shape, luminosity, or morphology. A wider review of AGN classes is given by, for example, Krolik and Di Matteo (2000) and Hardcastle and Croston (2020) give an excellent summary of RLAGN.

2.1.1.1 Seyfert galaxies

Seyferts are the most common type of AGNs. They were first discovered by Seyfert (1943) and show strong optical emission lines. They normally live in spiral galaxies and are mostly selected based on their strong emission lines which emanate from the nucleus. However, absorption features can also be used to classify them using X-ray observations (e.g. Singh et al., 2011). There are two types of Seyfert galaxies: type 1 and type 2. Seyfert 1s have broad optical emission lines while Seyfert 2s show narrow optical

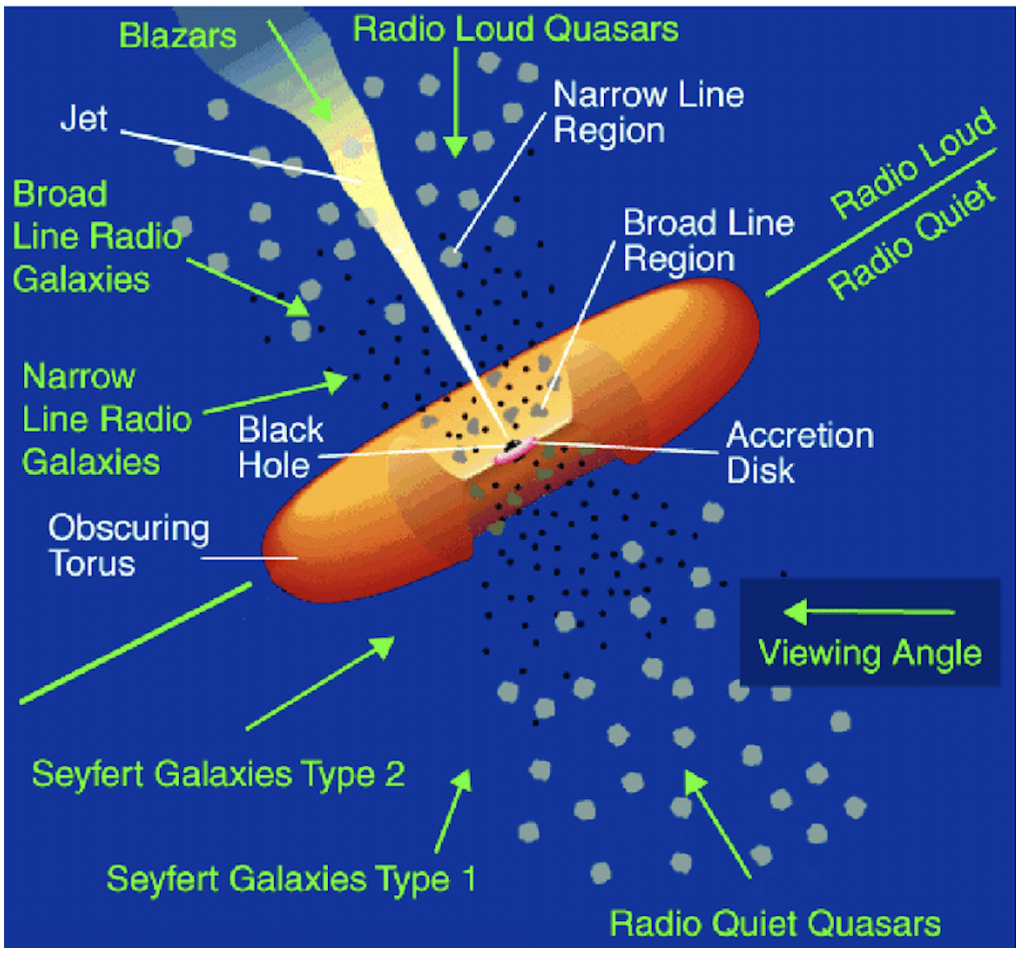

Figure 2.1: An AGN schematic by Urry and Padovani (1995) highlighting major components of different classes of AGNs following unification. The diagram is not to scale.

emission lines (e.g. Khachikian and Weedman, 1974). Further distinctions between the two types of galaxies can also be associated with their continuum emission; the continuum emission level in Seyfert 1s is stronger than in Seyferts 2s (e.g. Lawrence, 1987). Recent studies have, however, shown that the continuum emitting region for type 1 Seyferts is smaller in size compared to their counterpart type 2s (e.g. Nelson et al., 1996; Malkan et al., 2017).

With the exception of a few galaxies, Seyferts are mostly classified as RQAGN. A further subclass of populations of Seyfert galaxies exist and below, I briefly look at narrow-line Seyfert 1s (NLS1s) and their subclass, radio-loud narrow-line Seyfert 1s (RL-NLS1s).

- **NLS1s** – this is a subclass of Seyfert 1s which show "narrower" broad emission lines than typical Seyfert 1s (Osterbrock and Pogge, 1985). Their black hole masses are low and show large accretion rates close to the Eddington limit (e.g. Xu and Komossa, 2010a,b; Viswanath et al., 2019). Osterbrock and Pogge (1985) found that the basic features of NLS1s are such that, for example, their Balmer lines (e.g. Hβ) are below 2000 km/s at FWHM[1]. Their intensity line ratios between

[1] Full Width at Half Maximum.

[OIII] λ5000 and Hβ is smaller than the lower limit of 3 and they show stronger ionization emission lines [FeII] than typical Seyfert type 2 galaxies. In addition, NLS1s have been observed to show steeper (soft and hard) X-ray spectral indices ($\alpha \approx -2.13$) than "normal" Seyfert 1s ($\alpha \approx -1.34$) (e.g. Boller et al., 1996; Brandt et al., 1997). They are also considered to be associated with young AGNs at their early evolutionary stage in comparison to other Seyferts (e.g. Mathur, 2000); for an extensive review see, for example, Boller (2000). Komossa et al. (2006) in their recent studies have found that ∼7% of NLS1s are RLAGN (a brief discussion is given below) that is RL-NLS1s.

- **RL-NLS1s** – these possess the same features as RLAGN (e.g. blazars; Yuan et al., 2008, see also Section 2.1.1.2 for a summary on blazars) but show lower BH masses (e.g. Chen et al., 2015). The main difference from RLAGN is that RL-NLS1s are typically compact with physically small projected sizes extending up to 100 kpc (e.g. Doi et al., 2012); these properties are comparable to those seen in CSO, CSS, and GPS sources – see Sec. 2.1.1.6 on the description of these objects.

2.1.1.2 Blazars

These objects are characterised by strong continuum emission lines at a range of wavelengths (radio to gamma-rays; e.g. Zhang et al., 2001; Rani et al., 2013). As shown in Fig. 2.1, the radio emission from blazars is strongly oriented at small angles towards the observer's view. It has been suggested that their emission display various radio morphologies (e.g. Wardle et al., 1984; Giroletti et al., 2004). Using their optical emission lines (equivalent widths), Blazars like Seyferts can be subdivided into various classes. In the case where blazars display weak or no emission lines, they are referred to as *BL Lac* objects, after the AGN BL Lacertae (e.g. Padovani and Giommi, 1995). However, in the case where broad emission lines are present, blazars are called *flat-spectrum radio quasars* (FSRQs). We also have blazars that are classed as *optically violent variables* (OVVs). These are blazars with high optical variability (e.g. Gopal-Krishna et al., 2011; Gaur et al., 2012). We can unify some subclasses of blazars with radio AGNs (e.g. Xiong et al., 2015). A concise historical context is given by e.g. MacLeod and Andrew (1968), Schmidt (1968), Visvanathan (1969), and Oke and Gunn (1974)

2.1.1.3 Quasars

Quasi-stellar radio sources (quasars; Schmidt, 1963) are one of the two largest classes of AGNs (with Seyferts). They are the most distant and luminous class of AGNs (Schmidt, 1968) and can be grouped into radio-loud quasars (RLQs) and radio quiet-quasars (RQQs). Like Seyfert galaxies, quasars show similar optical properties and can be separated from other AGN classes based on their optical magnitudes (e.g. Schmidt and Green, 1983).

2.1.1.4 LINERs

LINERs (Heckman, 1980) are low-radio power AGNs. They show weak nuclear line emission (e.g. González-Martín et al., 2006) and cover the lower end of the AGN luminosity distribution function (both in the radio and γ-ray regime) partly due to their low luminosity in the core regions (e.g. Gallimore et al., 2006). Given that LINERs show no other AGN emission properties has resulted in an ongoing debate on whether they are in fact AGN or not (e.g. Heckman and Best, 2014) in part due to the fact that there is an overlap with *low-excitation radio galaxies* (LERGs)[2]. This is because both LINERs and LERGs are characterised by the presence of low-ionization line emission in their spectra and show weak or no emission lines at high excitation levels. LERGs, however, are more powerful than LINERs and show strong radio emission, whereas LINERs display weaker or non-detectable radio emission (see e.g. Ho, 2008, for reviews).

2.1.1.5 Radio galaxies

Radio galaxies can be distinguished on the basis of their optical line emission. Some show strong line emission (e.g. *high-excitation radio galaxies*: HERGs) while others present weak or no optical emission lines (e.g. LERGs) – I comment on the LERG/HERG dichotomy in Sec. 2.1.1.6.

Those that display strong line emission can be subdivided into broad- and narrow-line radio galaxies (BLRGs and NLRGs respectively). Their radio emission can extend over kpc up to a few Mpc scales. They share similar properties with radio-loud Seyferts; they differ with regard to where they live that is radio galaxies typically live in elliptical galaxies as opposed to spiral galaxies which host most radio-loud Seyferts. The Fanaroff-Riley type 1 and type 2 (FRI and FRII respectively) galaxies are the most common example of radio galaxies (Fanaroff and Riley, 1974, see Fig. 2.2 for examples of FRI/II objects). The classification of radio galaxies into FRI/FRII traditionally depends on their radio morphology and surface brightness. Regarding radio morphology, the ratio of the length between two points with the highest intensity to the whole emission (usually defined by R) is the factor that distinguishes the two types that is $R < 0.5$ for FRIs and $R > 0.5$ for FRIIs. The radio structure in FRIs is described by strong two-sided jets, disappearing into their surroundings while strong one-sided jets extending from the radio core and surrounded by two radio lobes characterise FRIIs. In terms of surface brightness, FRIs are centre-brightened while FRIIs are edge-brightened. The observed radio luminosity dividing line as seen by Fanaroff-Riley is around $L_{178\ \mathrm{MHz}} \sim 10^{25}$ W Hz^{-1}. However, this dividing line is complex to ascertain; an overlap of FRI/II objects has been observed on both parts of the radio luminosity regime (e.g. Gopal-Krishna and Wiita, 2000; Mingo et al., 2019). The FRI/II dichotomy is further discussed in Sec. 2.2.2.

[2] See Sec. 2.1.1.6 and 2.1.2 for a discussion on LERGs.

2.1.1.6 Other radio galaxy classifications

It is also worth commenting on other classes of radio galaxies such as LERGs and HERGs (e.g. Hine and Longair, 1979; Tasse et al., 2008). HERGs show strong emission lines and are mostly FRIIs. They include quasars selected in the optical (and show similar spectra to BLRGs dominating continuum emission) as well as include both BLRGs and NLRGs with similar optical spectra with those of respectively, Seyfert 1s and Seyfert 2s (e.g. Laing et al., 1994). However, what is seen in LERGs is the absence of strong continuum emission. LERGs are mostly FRIs; a significant number of FRIIs have also been reported (e.g. Hardcastle and Worrall, 2000; Mazoochi et al., 2022). The differences in high excitation lines (e.g. [OIII]) in HERGs and LERGs have been observed in optical, X-ray, and mid-IR wavebands (respectively e.g. Chiaberge et al., 2002; Hardcastle et al., 2006; Hardcastle et al., 2009). Regarding accretion onto their respective central SMBHs, HERGs show higher (between 1 and 10%) Eddington-scaled accretion rates (hence radiatively efficient: RE) (e.g. Best and Heckman, 2012), in comparison, LERGs accrete well below 1% of their Eddington-scaled accretion rates (hence radiatively inefficient: RI). In addition to these differences, LERGs inhabit richer environments (e.g. Hardcastle, 2004; Mingo et al., 2014) compared to HERGs. For a wider review see e.g. Hardcastle et al. (1998a), Hardcastle (2004), Hardcastle et al. (2006), and Hardcastle and Croston (2020).

Other interesting compact objects relevant to this study are CSO, CSS, and GPS sources. These luminous (10^{25} W Hz^{-1} at 1.4 GHz) yet compact objects are defined on the basis of their radio spectrum (see Chapter 4 Sec. 4.5.1 for a further discussion). They show a spectral turnover at gigahertz (GHz) frequencies (i.e. GPSs) or a peak at megahertz (MHz) frequencies (i.e. CSSs). They are all small in physical scales extending up to $\sim$20 kpc (CSSs) in projected physical scales while GPS sources extend up to a maximum of $\sim$1 kpc in projected physical size. CSOs are much smaller compared to GPSs/CSSs with projected maximum linear sizes of only a few 100 pc. Their small physical sizes have led to the idea that they are the smaller versions of extended objects and represent the AGN evolution in the early stage (e.g. Kunert-Bajraszewska et al., 2010). For recent reviews see e.g. O'Dea and Saikia (2021).

Additionally, there has been an emergence of unresolved RLAGN numerically dominating the local Universe at low frequencies. These objects are sometimes termed 'FR0' sources. This comes from the fact that they share similar features with FRIs, but without the extended emission seen in typical FRI sources. A detailed review is presented by, for example, Baldi and Capetti (2010), Sadler et al. (2014), and Baldi et al. (2015, 2016). A further discussion of these sources is also given in Sec. 4.5.4 of Chapter 4.

In the above sections, I have described various classes of AGNs and in the next section, I briefly describe how these AGN classes have been unified under the standard model presented in Fig. 2.1.

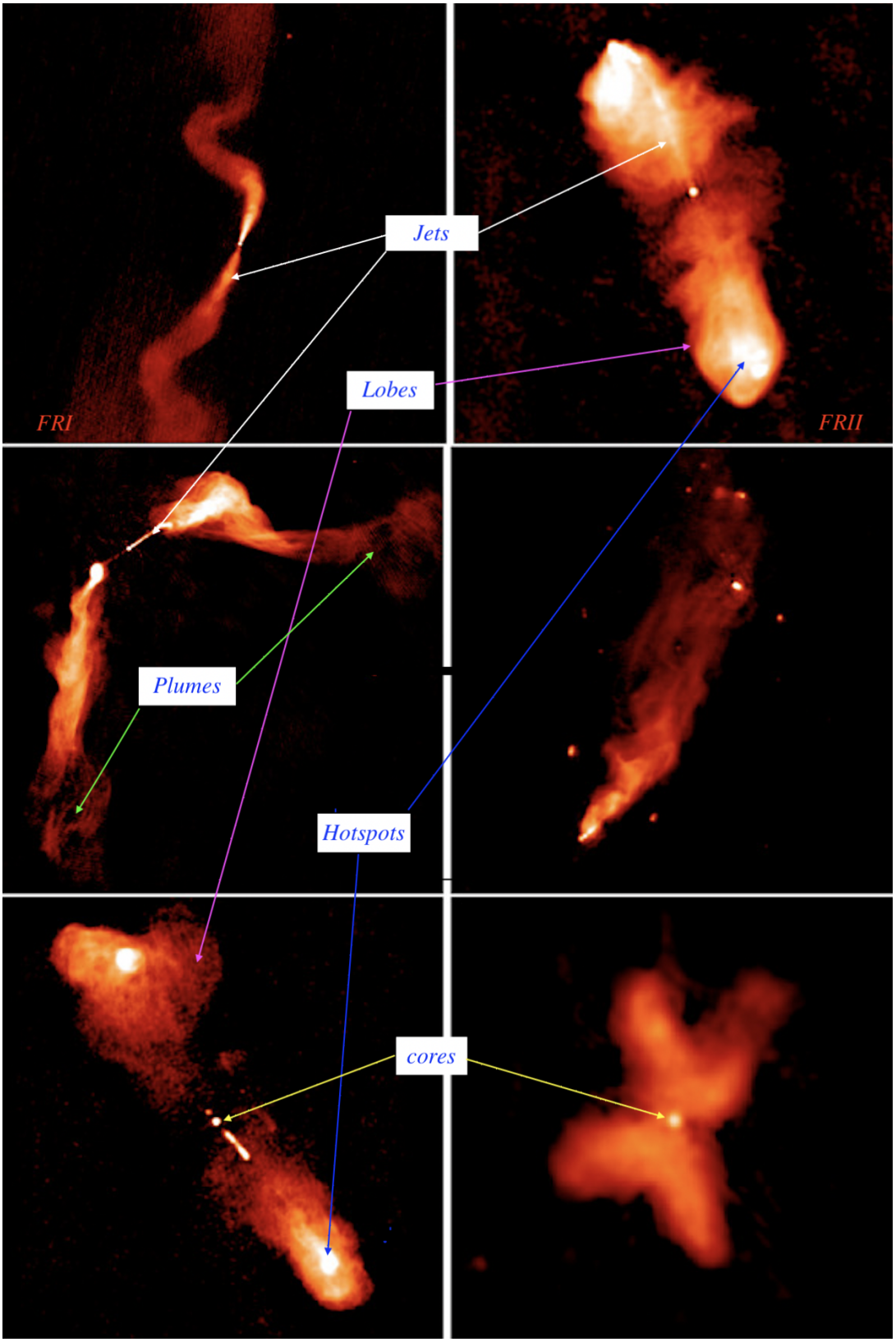

Figure 2.2: Images examples of radio galaxies. The top panels represent the FR class: *left* is the FRI source, 3C 31 while on the *right* is 3C 98, the FRII source. Middle panels: *left* is 3C 465, the wide-angle tail source, and on the *right* is NGC 6109, the head-tail/narrow-tail angle source. The bottom panels: on the *left* is 3C 219, the double-double source while on the *right* is 3C 315, the core-restarting source. Well-collimated jets can be seen in 3C 31, 3C 98, and 3C 465 while 3C 98, 3C 465, and 3C 219 show strong bright spots (hotspots). This Figure is extracted from Hardcastle and Croston (2020).

2.1.2 AGN unification phenomenon

In the previous sections, I have highlighted how AGN classifications are mainly associated with their observed properties. Attempts to unify these different classes of AGNs (e.g. Blandford and Rees, 1974; Rowan-Robinson, 1977; Scheuer and Readhead, 1979; Barthel, 1989) under the current model (Fig. 2.1) has been an ongoing issue. The preferred AGN phenomenology interpretation has been linked to the black hole-accretion disk paradigm (e.g. Antonucci and Miller, 1985; Lawrence, 1987; Antonucci, 1993; Urry and Padovani, 1995). This favoured interpretation is what is believed to account for the compactness and the high luminosity features observed in some AGNs.

A brief discussion on the unification model by Urry and Padovani (1995) based on two assumptions thus (1) the AGN's emitting components and (2) the AGN's angle of view with respect to the observer follows here. However, it is very important to note that this unification scheme does not work for all AGNs; I comment on this and the implication in unifying RLAGN in Sec. 2.1.2.1 based on the works of e.g. Hardcastle and Croston (2020).

As in Fig. 2.1, it is assumed that all AGNs have a central SMBH of mass $\gtrsim 10^6$ $M_\odot$ (e.g. Woltjer, 1959; Liang and Liu, 2003; Peterson, 2015) which is the source of the high luminosity observed in AGNs; this high luminosity is due to the release of the gravitational potential energy from the central SMBH. Surrounding the SMBH is an accretion disk (e.g. Szuszkiewicz et al., 1996) that rotates around it. The material in the accretion disk accumulates and loses its angular momentum, falling onto the centre of the SMBH hence, powering it. The energy associated with the spin of the SMBH or the rotating accretion disk results in the ejection of highly collimated outflows of relativistic plasma on either side[3] of the SMBH perpendicular to the accretion disk (e.g. Narayan and Yi, 1994), transporting material at relativistic speeds from the central regions of the SMBH to distances away on kpc (and sometimes Mpc) scales. In the radio regime, the identification criterion for these highly collimated outflows of plasma (*jets*; Burbidge, 1956) on such scales is due to the synchrotron process[4] – the gyration of relativistic charged particles (e.g. electrons, positrons, or protons) as they interact with magnetic fields (e.g. Begelman et al., 1984).

Energised photons are emitted by the accretion disk (a source of thermal radiation up to temperatures of $\sim$30 000 K, e.g. Malkan and Sargent, 1982) ionising the hot gas above it to form *broad-line regions* (BLRs; e.g. Grier et al., 2017) within the *torus* (Krolik and Begelman, 1986) while the *narrow-line regions* (NLR; e.g. Ho, 2008) forms farther away from BLRs. In the BLR, high-velocity dense clouds of matter (with distances of the order of $\sim$10 light days) orbit above or below the disk and display broad emission lines in the optical while in the NLR, these dense clouds of matter (which are larger up to a few hundred pc than those in BLR) move at lower velocities and exhibit narrow-line emission (e.g. Peterson, 1997; Osterbrock and Ferland, 2006). Located in the plane of the accretion disk (and outside the BLR) away from the centre of the SMBH is the obscuring structure of gas or dust (i.e. the

[3] Or both sides (e.g. Blandford and Payne, 1982).
[4] See Sec. 2.2.1.1 on the theory of synchrotron emission.

torus). X-ray observations (e.g. Markowitz et al., 2014) have revealed that the torus is a clumpy region with different densities obscuring the BLR and the accretion disk from the view of the observer and 're-radiates' emission from the central engine in infrared observations (e.g. Nenkova et al., 2008).

With regard to the observer's angle of view of the AGN, various AGN classes can be unified into a single entity by considering mainly the system's orientation regarding the line of sight (e.g. Antonucci and Miller, 1985). Properties such as the radio-loudness, radio power, and the optical spectra (e.g. Lawrence, 1987; Antonucci, 1993; Urry and Padovani, 1995) can be taken into consideration. Another property, nuclear luminosity, was added (e.g. Tadhunter, 2008) to account for LINERs. These authors have argued that the variation in the classification of AGNs comes down to the observation angle. For example, at smaller angles (typically $< 10°$), the torus does not obscure the BLR so we *see* type 1 AGNs (BL Lacs and FSRQs) dominating the line of sight. At this angle, the jets from type 1 AGNs align well with the observer. However, at large observing angles, we see the torus hiding the BLR from the line of sight (due to radiation absorption by either the gas or dust in the torus) and we observe type 2 AGNs (i.e. narrow-line FRI/FRIIs, and type 2 Seyferts). It is also thought that (independent of the system's orientation) the radio-loud parent population of FRIs and BL Lacs is the same on the basis of their extended radio emission properties (e.g. Wardle et al., 1984; Antonucci and Ulvestad, 1985) while FRIIs are generally considered to be the progenitors of FSRQs. However, this idea is somewhat untrue (e.g. Kharb et al., 2010) following observations that have revealed that some BL Lacs show radio morphologies resembling those of FRIIs (e.g. Bondi et al., 2001).

2.1.2.1 Comments on AGN unification

Although the AGN unified scheme proposed by Urry and Padovani (1995) provides an accepted model for most classes of AGN, the orientation-based scheme poorly accounts for the distinctions we see between radio-loud and radio-quiet AGNs and the link to the more powerful yet compact CSS/GPS sources. To incorporate these sources, some parameters (e.g. SMBH spin, BH mass, luminosity, and accretion rates) can be considered (e.g Meier, 2002; Fanidakis et al., 2011). For example, CSS/GPS objects can be unified with RLAGN by considering their evolution; this comes from the idea that suggests that these objects are young AGN sources (e.g. Bicknell et al., 1997; O'Dea, 1998) and could evolve into the more powerful and extended FRI/FRII sources depending on their jet and luminosity evolution (e.g. Kunert-Bajraszewska and Labiano, 2010). Regarding the unification of radio-quiet AGNs, particularly in the local Universe, properties such as the geometry of the central absorber, galaxy evolution, and intrinsic differences in AGN populations can be considered (e.g. Beckmann and Shrader, 2012; Heckman and Best, 2014).

Further complications arise from the fact that not all AGNs are intrinsically the same, particularly RLAGN. Besides the fact that the orientation-based unification scheme by Urry and Padovani (1995) explains well the differences between type 1 and 2 Seyferts (the difference, as suggested by Antonucci, 1993, between the two types is mainly down to the line of sight that can be explained with regard to the obscuring torus),

the AGN orientation-based unification scheme of RLAGN (which by observation can be separated into HERGs and LERGs) proposed by, for example, Barthel (1989)[5], does not account for LERGs. Until recently, it was unclear on whether LERGs intrinsically did not have NLRs or were heavily obscured that we can not *see* them – and so can not be unified with quasars which always show NLRs – while showing standard features of AGN activity, however, mid-IR and X-ray observations have revealed that there is no such evidence (respectively e.g. Whysong and Antonucci, 2004; Hardcastle et al., 2006) thus their nuclear emission (in the optical and X-ray) all come from the active jets only (e.g. Hardcastle and Worrall, 2000). Therefore, LERGs show no signs of an accretion disk, a torus, BLRs, nor NLRs that effectively radiate emission (e.g. Hardcastle et al., 2007; Hardcastle and Croston, 2020) and can not be unified under the standard model (Fig. 2.1) of Urry and Padovani (1995).

Interestingly, Hardcastle et al. (1998a) suggested that most RLAGN in the local Universe are LERGs hence, we have to treat them separately as non-unified sources, and doing so could solve the low-redshift problem (Barthel, 1989) in the unification of RLAGN if we also consider BLRGs as low-luminosity quasars. In addition to the discussion given on HERGs/LERGs in Sec. 2.1.1.6, Table 2.1 summarises the unification of LERGS (RI) and HERGs (RE) based on the works of Hardcastle and Croston (2020) and references therein.

Table 2.1: Unification model for RLAGN. Adapted from Hardcastle and Croston (2020).

	Jet at large angles to the line of sight	**Intermediate angles**	**Jet closely aligned to line of sight**
Radiatively inefficient (RI)	LERGs (FRI or FRII)	LERGs (FRI or FRII)	BL Lacs
Radiatively efficient (RE)	NLRGs (some FRI, mostly FRII)	BLRGs or lobe-dominated or steep-spectrum quasar (some FRI, mostly FRII)	Core-dominated, flat spectrum or OVV quasar

2.2 Radio-loud AGN: theory and observation

In the previous sections, I highlighted examples of RLAGN (e.g. BL Lacs, OVVs, RLQs, FRI, and FRIIs). I discuss the FRI and FRII objects further in Sec. 2.2.2.2 while the theory and observational properties of RLAGN as a whole follow below.

2.2.1 Theory

RLAGN physics is important for modelling the emission and absorption mechanisms from specific regions of AGN. The mechanism that produces radiation when say, an electron, interacts with say, an ion, is known as *free-free emission* ('FFE') or *Bremsstrahlung*. FFE plays many important roles, including the generation of AGN X-ray emissions (e.g. Longair, 2011). The reverse process of FFE is called free-free absorption ('FFA'). FFA plays an important role in type 2 AGNs where the dusty torus significantly

[5] Barthel developed the first model that suggested that looking at the radio galaxy pole-on results in BLRGs or Quasars (i.e. we *see* BLRs and an accretion disk) while looking at it edge-on results in NLRGs (we *see* NLRs). This model, however, breaks down in part due to the absence of low-redshift FRII quasars (e.g. Hardcastle, 2004).

absorbs the emission from the central region of the SMBH − In this thesis, I have deferred FFA models and their effects on our low-luminosity compact RLAGN to the near future. In this Section and also in Chapter 4, therefore, I only address synchrotron self-absorption (SSA). The derivations that follow below are based on the work of Longair (2011).

2.2.1.1 Synchrotron physics

The major contribution of emission in RLAGN is *synchrotron radiation*. A charged particle produces synchrotron radiation upon interacting with magnetic fields causing it to accelerate due to the Lorentz force given by the gyrofrequency (ν_g) thus

$$\nu_g = \frac{eB}{2\pi\gamma m_e} \tag{2.1}$$

where m_e is the mass of the electron, the magnetic field strength is represented by B, and $\gamma = (1 - \frac{v^2}{c^2})^{-1/2}$, the Lorentz factor of the electron. The energy loss rate, under which a charged particle q accelerates perpendicular ($a_\perp$) and parallel ($a_\parallel$) to the lab coordinate system is

$$-\left(\frac{dE}{dt}\right)_{rad} = \frac{q^2\gamma^4}{6\pi\epsilon_0 c^3}\left(|a_\perp|^2 + \gamma^2|a_\parallel|\right) \tag{2.2}$$

where ϵ_0 is the permittivity of free space. However, the charged particle always accelerates perpendicular to the velocity vector thus $|a_\parallel| = 0$ and Eq. 2.2 reduces to

$$-\left(\frac{dE}{dt}\right) = \frac{q^2\gamma^4}{6\pi\epsilon_0 c^3}|a_\perp|^2. \tag{2.3}$$

Taking $a_\perp = evB\sin\alpha/\gamma m_e$ for the centripetal acceleration of a relativistic charged particle, Eq. 2.3 can be expressed as

$$-\left(\frac{dE}{dt}\right) = \frac{e^4B^2}{6\pi\epsilon_0 c m_e^2}\frac{v^2}{c^2}\gamma^2\sin^2\alpha \tag{2.4}$$

which is the total radiation loss rate. We can recast Eq. 2.4 into a more useful expression by introducing the quantity $c^2 = 1/(\mu_0\epsilon)$ thus

$$-\left(\frac{dE}{dt}\right) = 2\left(\frac{e^4}{6\pi\epsilon_0^2 c^4 m_e^2}\right)\frac{v^2}{c^2}c\left(\frac{B^2}{2\mu_0}\right)\gamma^2\sin^2\alpha \tag{2.5}$$

where the first term in brackets on the right-hand side of Eq. 2.5 is the Thomson cross-section while the second term in brackets is the energy density of the magnetic field defined respectively as

$$\sigma_T = \frac{e^4}{6\pi\epsilon_0^2 c^4 m_e^2} \tag{2.6}$$

and

$$U_{mag} = \frac{B^2}{2\mu_0}. \tag{2.7}$$

We can recast the total energy loss rate (Eq. 2.5) using Eq. 2.6 and Eq.2.7 while taking the ultra-relativistic limit $v \to c$ to give

$$-\left(\frac{dE}{dt}\right) = 2\sigma_T c U_{mag} \gamma^2 \sin^2\alpha \tag{2.8}$$

which applies to electrons with pitch angle α. Thus for an isotropic distribution of α defined by $p(\alpha)d\alpha = \frac{1}{2}\sin\alpha \mathrm{d}\alpha$, the electron probability distribution, we can integrate Eq. 2.8

$$-\left(\frac{dE}{dt}\right) = 2\sigma_T c U_{mag} \gamma^2 \left(\frac{v}{c}\right)^2 \frac{1}{2} \int_0^\pi \sin^3\alpha \mathrm{d}\alpha \tag{2.9}$$

which results in

$$-\left(\frac{dE}{dt}\right) = \frac{4}{3}\sigma_T c U_{mag} \left(\frac{v}{c}\right)^2 \gamma^2. \tag{2.10}$$

This is expected for a single electron with high energy assuming the probability density is evenly spread in all directions for pitch angle α. We can see clearly from Eq. 2.10 that the total radiation loss rate directly relates to the energy of the particle squared. This implies that since $\gamma = E/m_e c^2$, electrons with the highest energy lose energy faster from synchrotron radiation. The emission spectrum for a single electron can be shown using the derivations of Longair to be

$$j(\nu) = 2\pi j(\omega) = \frac{\sqrt{3}e^3 B \sin\alpha}{4\pi\epsilon_0 c m_e} F\left(\frac{\nu}{\nu_c}\right) \tag{2.11}$$

where the function $F(\nu/\nu_c)$ is a constant (see Longair, 2011, for details), $j(\omega)$ is the spectrum emissivity of a single electron defined as

$$j(\omega) = \frac{\sqrt{3}e^3 B \sin\alpha}{8\pi^2\epsilon_0 c m_e} F\left(\frac{\omega}{\omega_c}\right) \tag{2.12}$$

and ν_c is the critical frequency[6] given by

$$\nu_c = \frac{3}{2}\gamma^2 \left(\frac{eB}{2\pi m_e}\right). \tag{2.13}$$

The power-law distribution of an ensemble of electrons is given by

$$N(E) = \kappa E^{-p} \tag{2.14}$$

where κ is the normalization of the electron energy spectrum and p is the power law index. The total synchrotron emissivity $J(\nu)$ is then determined if we integrate over electron energies between E_{min} and E_{max} ($= \gamma^2 m_e c^2$) while utilising Eq. 2.13 to yield

$$J(\nu) = \frac{\sqrt{3}e^3 B \sin\alpha}{4\pi\epsilon_0 c m_e} \int_{E_{min}}^{E_{max}} F(x) N(E) dE. \tag{2.15}$$

[6]For a single charged particle, its emission peaks strongly around this frequency.

Here, $F(x)$ is the spectrum of a single charged particle and $x = \omega/\omega_c = \nu/\nu_c$[7] at ultra-relativistic speeds. Integrating Eq. 2.15 over energy and pitch angle,

$$J(\nu) = \frac{\sqrt{3}e^3 B\kappa}{4\pi\epsilon_0 c m_e}\left(\frac{3eB}{2\pi\nu m_e^3 c^4}\right)^{(p-1)/2} a(p), \tag{2.16}$$

where

$$a(p) = \frac{\pi}{2}\frac{\Gamma\left(\frac{p}{4}+\frac{19}{12}\right)\Gamma\left(\frac{p}{4}-\frac{1}{12}\right)\Gamma\left(\frac{p}{4}+\frac{5}{4}\right)}{(p+1)\Gamma\left(\frac{p}{4}+\frac{7}{4}\right)} \tag{2.17}$$

is a constant and Γ is a gamma−function.

We can recast Eq. 2.16 as

$$J(\nu) \propto \kappa\nu^{-\frac{p-1}{2}} B^{\frac{p+1}{2}} \tag{2.18}$$

which shows that for a power-law synchrotron spectrum, electron energy distributions follow a power-law relation. In astronomy, the definition of α (the spectral index) of a source is conveniently expressed in terms of the power-law index (p) thus $\alpha = (p-1)/2$ which is expressed in the form of the observed flux density (S) at an observing frequency (ν) by

$$S_\nu \propto \nu^\alpha. \tag{2.19}$$

Note that we have not presumed the sign of α in Eq. 2.19; a common convention in radio astronomy.

In a synchrotron emitting source, electrons can sometimes re-absorb the radiation they produced on their way out of the plasma. This phenomenon is known as *synchrotron self-absorption* (SSA; see Kellermann, 1966, for details). Using the derivations of Longair, the SSA absorption coefficient (χ_ν) can be shown to be

$$\chi_\nu = \frac{\sqrt{3}e^3 c}{8\pi^2\epsilon_0 m_e} k B^{(p+2)/2}\left(\frac{3e}{2\pi m_e^3 c^4}\right)^{p/2} b(p)\nu^{-(p+4)/2} \tag{2.20}$$

where

$$b(p) = \frac{\sqrt{\pi}}{8}\frac{\Gamma\left(\frac{3p+22}{12}\right)\Gamma\left(\frac{3p+2}{12}\right)\Gamma\left(\frac{p+6}{4}\right)}{\Gamma\left(\frac{p+8}{4}\right)} \tag{2.21}$$

is a constant. The result in Eq. 2.20 tells us that for a synchrotron emitting source, there is a turnover in the spectrum of the source at a frequency, say ν_t, which occurs at an optical depth described by $\tau_{SSA} = 1$. During observations, when the central frequency, say ν, is greater than ν_t, the result corresponds to an optically thick medium (i.e. $\tau_{SSA} > 1$) and the opposite (i.e. $\nu < \nu_t$) results in an optically thin medium (i.e. $\tau_{SSA} < 1$). This analysis will play an important role in Chapter 4 (Sec. 4.5.2).

[7] Also, $\omega_c = 2\pi\nu_c$.

2.2.2 Observation: components and morphology

2.2.2.1 Components

It will be useful in future sections to briefly discuss the observed components of RLAGN (see Fiq 2.2) in relation to the observed radio spectra. These components are *jets*, *cores*, *hotspots*, and *lobes* and are discussed based on a historical context given by, for example, Bridle and Perley (1984) and Perley et al. (1984). Other components of RLAGN such as *plumes*, *wings*, *tails*, *haloes*, and *bridges* will not be discussed considering our objects (Chapter 4) are too compact to show these features.

- **Jets** – these are a significant part of emission in RLAGN. Historically, a jet is defined as a *narrow* feature of a radio source that is at least a few times longer than its width. The observed spectral index values for jets range between $-1.0 \leq \alpha \leq -0.5$ while their emission spans the kpc scale and sometimes the Mpc scale.
- **Cores** – these are observed coincident to the centre of their host galaxy and generally show flat and/or inverted radio spectra, i.e. $\alpha > 0$. Cores are unresolved on arcsecond scales (with sizes up to a few kpc scales) and VLBI imaging (e.g. Ros and Pérez-Torres, 2012) show that they are the synchrotron self-absorbed components of larger extended structures (jets or lobes).
- **Hotspots** – these are compact bright regions that are typically observed to lie in radio lobes and usually associated with classical doubles; high luminosity sources with symmetrical double lobes (e.g. Leahy and Williams, 1984). They show flat spectral indices between $-0.5 \leq \alpha \leq 0$ and are compact (maximum projected physical size of up to a few kpc).
- **Lobes** – these show steeper radio spectra ($\alpha < -0.7$) and their structures are comparatively very large extending up to kpc scales. Usually, lobes can be seen in powerful radio sources at both ends of a radio jet typically symmetrically configured on both sides away from the central core region.

2.2.2.2 Morphology

In addition to the discussion given in Sec. 2.1.1.5, RLAGN are known to show a range of radio morphologies (see Fig. 2.2) and in this section, I look at the radio morphologies of FRI/FRIIs which have proven to be robust in the classification of RLAGN based on their extended radio emission and radio luminosity.

- **FRIs** – these are typically low-luminosity ($L_{178} < 10^{25}$ W Hz^{-1}) sources and show extended radio emission in the form of jets that are usually two-sided and interact with external environments away from their galactic centre out on kiloparsec scales. FRIs are centre-brightened. An example of an FRI object is the 3C 31 source shown in Fig. 2.2.

- **FRIIs** – these objects usually show highly collimated one-sided radio jets, due to orientation and relativistic beaming which have significant effects on their appearance; if the relativistic jet is directed towards the observer, the radiation will appear brighter and the apparent size will appear more compact than if the jet was pointed away from the observer. These jets end up in radio lobes (which are usually large up to kpc scales) with bright spots which make them appear edge-brightened. The luminosities of FRIIs are typically greater than 10^{25} W Hz^{-1} at 178 MHz. The jets of FRIIs interact with the external environment on kpc (and sometimes on Mpc) scales. See Fig. 2.2 for an FRII source e.g. 3C 98.

These two categories of FR sources have been widely studied, however, the link between radio jet morphology and black hole accretion modes has been a topic of debate (e.g. Best and Heckman, 2012; Mingo et al., 2014; Hardcastle, 2018a). In the next section, I look at some properties that attempt to explain the Fanaroff & Riley (FR) dichotomy.

2.2.3 The FR dichotomy

Fanaroff and Riley proposed a scheme of classifying RLAGN on the basis of their morphology and radio power. Since then, a number of attempts to explain the differences between the FR classes have been put forward. Some of these are (1) the disparities in the properties of the IGM on interaction with the jets of FRI/II sources (e.g. Kakiichi et al., 2018) and (2) the differences in the properties of the central engine in the galaxies they inhabit (e.g. Giovannini et al., 2002).

The first point supports the idea which proposes that the type of radio morphology we observe is due to interaction between jets and the IGM (e.g. Gopal-Krishna and Wiita, 2000). The second point arises from the fact that FRIs show higher black hole masses than FRIIs (e.g. Ghisellini and Celotti, 2001) which supports the idea that most FRIIs, particularly those classified as HERGs, accrete material onto their central SMBH at higher Eddington-scaled accretion rates than FRIs (e.g. Meier, 1999; Marchesini et al., 2004; Garofalo et al., 2010). Another interesting argument arises in terms of the differences in the contents of jets (e.g. Celotti and Fabian, 1993); the fact that FRIs possess lower-radio powers on average compared to FRIIs means that they are in direct contact with their environments hence, their jets lose their relativistic speeds due to entrainment of various particles as they permeate their surroundings causing them to slow down (e.g. Laing, 1994) on kpc scales while the jets of FRIIs remain relativistic throughout (e.g. Bicknell, 1995); probably because most FRIIs live in poor environments – I comment on this point in the next paragraph. However, despite the differences in radio luminosity as seen in Sec. 2.2.2.2, it has also been observed that luminosities for some FRI and FRII objects overlap at high frequencies (e.g. Gopal-Krishna and Wiita, 2000) and low frequencies (e.g. Mingo et al., 2019) with some sources displaying hybrid characteristics between the FR classes (e.g. Gawroński et al., 2006; Stroe et al., 2022).

Following up on points (1) and (2), the variation in the properties of radio jets, radio luminosities, and radio morphologies between the two FR classes is in part associated with differences in the properties of

their environments (e.g. Miraghaei and Best, 2017). FRIs are associated with optically bright elliptical galaxies and live in rich galaxy clusters while FRIIs are associated with 'normal' elliptical galaxies, are typically isolated, and live in poor group environments. However, this is not entirely true as observational evidence for high redshift ($z \sim 0.5$) FR sources (e.g. Hill and Lilly, 1991) suggest that both FR classes live in rich cluster environments. Attempts to reconcile the differences between the two FR populations have been drawn from observation of the differences in accretion modes and based on this, the idea that FRIIs are expected to eventually evolve into FRIs has been suggested (e.g. Maraschi and Rovetti, 1994; Wang et al., 2011).

In addition to the discussion, the emergence of a population of unresolved/compact RLAGN numerically dominating the local Universe will provide a better picture in understanding the FR dichotomy. The fact that some of these compact RLAGN (e.g. FR0s) have been linked to FRIs but without the extended emission seen in FRI sources is interesting in itself and further studies of the so-called FR0s will expand our knowledge on the FR dichotomy as well as improve our understanding of AGN feedback – I summarise AGN feedback models in the next section.

2.3 AGN feedback models

As mentioned earlier, one of the challenges that arise in unifying AGNs is their role in the formation and evolution of galaxies through the process known as *AGN feedback*. See e.g. Croton et al. (2006) and Hardcastle and Croston (2020) for reviews.

The time required for AGNs to evolve (e.g. Smolčić et al., 2009; Fabian, 2012; Best et al., 2014) has a direct consequence on the growth of SMBHs and on SF (see Silk and Rees, 1998; Di Matteo et al., 2005). The effects of AGN activity on the intercluster medium (ICM) as well as the luminosity function of AGNs (e.g. Rigby et al., 2011; Bharadwaj et al., 2014) can be explained by AGN feedback models. It has been shown (analytically and to some extent observational – see below) that the jets of powerful RLAGN (e.g. FRI/IIs) have an effect on their surroundings when they transport galactic outflows (various gas phases) on galactic scales (e.g. Morganti et al., 2005a,b) which results in either slowing or entirely stopping the hot gas responsible for SF from cooling (e.g. Somerville and Davé, 2015; Hardcastle and Croston, 2020). Here I summarise the two favoured AGN feedback models: the radiative (quasar) and the kinetic (radio) mode.

- **Quasar mode:** this AGN feedback model is largely based on simulations (e.g. Richardson et al., 2016) which provide a working mechanism that agrees with other galaxy formation and evolution models. This mode introduces the idea were galaxy mergers play a significant role in AGN activity. This theorises that galaxies interact with each other to merge into one big galaxy. This merging results in the disruption of the galactic bulge which triggers AGN activity; probably due to high accretion rates or the direct depositing of matter onto the AGN core as a result thereof. The radiating winds driven by mergers sweep through galactic environments heating up the cold gas

responsible for SF and so slowing (and sometimes halting) stars from forming. This process, if it occurs, takes place primarily in high redshift ($z \sim 2$) and very luminous (RE) AGNs (quasars; e.g. Harrison, 2017)

- **Radio mode:** there is evidence based on observation (e.g. Best et al., 2006; Fabian, 2012) for this heating mechanism which occurs in the cold central regions of galaxy clusters. The centre of rich galaxy clusters is expected to be colder (due to cool molecular clouds responsible for SF) than their outer regions, however, the input energy from jets of powerful RLAGN permeate through the ICM, generating hot bubbles and heating up the fuel (halo gas) responsible for the cooling of these clouds hence regulating the rate of accretion consequently slowing or entirely halting SF. Observational evidence, therefore, makes this the preferred working mechanism in the local Universe.

The test of AGN feedback models has primarily been associated with powerful RLAGN; however, the energy input that low-luminosity compact RLAGN deposit into their environments is as yet unknown. There seems to be a vast majority of low-luminosity compact RLAGN, particularly in the local Universe, and they should be given the attention they deserve if we are to fully comprehend AGN feedback models.

2.4 Radio interferometry

Not much information was known about radio galaxies and their emission until the advent of radio interferometry (Ryle, 1952) which enabled us to detect and study them. However, it was not until observations such as those of Northover (1973) on the radio galaxy 3C 66 that a more detailed study of radio jets was revealed. This laid the foundation for understanding radio jets' origins, dynamics, and energetics.

Radio interferometry is the use of many individual dishes that can be spread over a large area to function as a large-single telescope. By definition, the angular resolution of an interferometer is represented mathematically as

$$\theta = \frac{\lambda}{\mathrm{B_{max}}} \tag{2.22}$$

where the wavelength is represented by λ and $\mathrm{B_{max}}$ represents the maximum separation between two telescopes/dishes (baseline). Using radio interferometry, the highest angular resolution down to the sub milli-arcsecond range can be achieved, enabling high resolution observations over wider observation bandwidths. The high resolution that interferometers provide, therefore, allowed for the discovery of celestial objects such as RLAGN.

2.4.1 Theory of a two-element interferometer

To understand how interferometers work, I summarise in this Section the theory behind the two-element interferometer which is the simplest example that shows how large-scale interferometers operate. The

derivations presented here come from the work of Thompson et al. (2017).

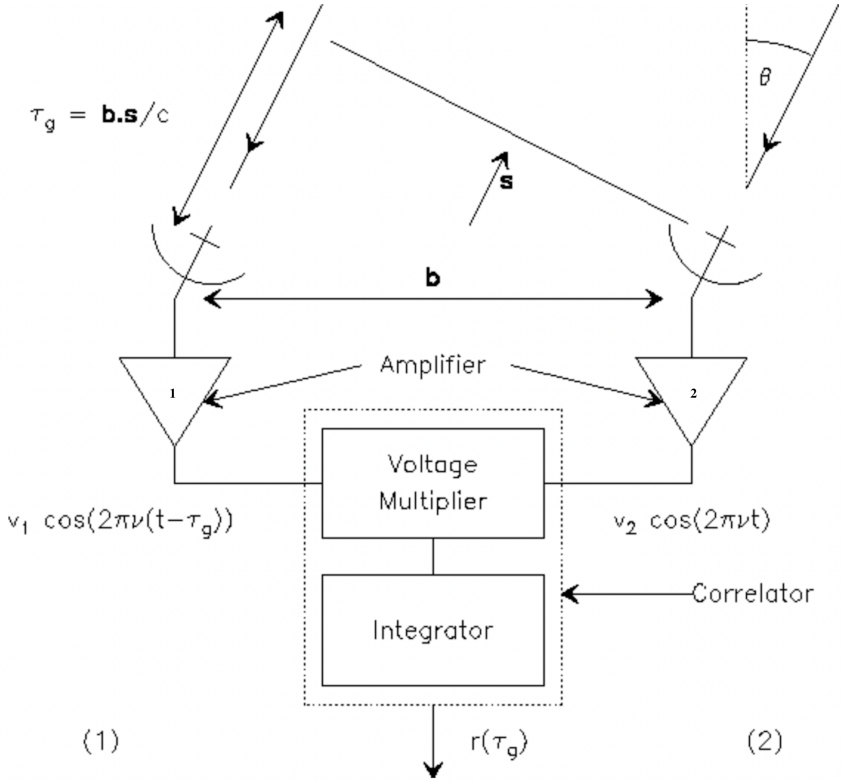

Figure 2.3: The two-element interferometer schematic diagram. The Figure is an adaption from Taylor et al. (1999).

A source in the sky is observed by both telescopes, however, the radiation of the object is recorded by the first (1) telescope with respect to the second (2) with a geometrical delay[8] τ_g thus

$$\tau_g = \frac{\vec{\mathbf{b}}.\hat{\mathbf{s}}}{c} \tag{2.23}$$

where $\vec{\mathbf{b}}$ is the separation between the two telescopes, $\hat{\mathbf{s}}$ is the source directional unit vector, and c is the speed of light. We can define the phase ϕ in relation to the geometrical delay in Eq. 2.23 as

$$\phi = \omega\tau_g = \frac{2\pi}{\lambda}\vec{\mathbf{b}}.\hat{\mathbf{s}} \tag{2.24}$$

where $c = \lambda v$ and in this case, λ is the observing wavelength. The voltages (V_1 and V_2) induced by the source's radiation is given by $V_1 = \mathrm{v_1}\cos(2\pi\nu(\mathrm{t} - \tau_\mathrm{g}))$ and $V_2 = \mathrm{v_2}\cos(2\pi\nu\mathrm{t})$ which when correlated results in

$$\langle V_1 V_2 \rangle = \langle V\cos(\omega\mathrm{t})\cos(\omega(\mathrm{t} - \tau_\mathrm{g}))\rangle \tag{2.25}$$

where $V = \mathrm{v_1 v_2}$ for the same source and $\omega = 2\pi\nu$. In this case, the time average is represented by the angled brackets. Applying some algebra to Eq. 2.25 and taking into consideration that ωt averages to

[8] The term geometrical delay comes from the fact that the delay relies on the relative position of the antennas and the source in the sky.

zero in faster oscillations, we get

$$\langle V_1 V_2 \rangle = \left(\frac{V^2}{2}\right) \cos(\omega \tau_{\rm g}) \tag{2.26}$$

the final correlator output. As the position of the antennas relative to the sky changes due to the Earth's rotation, the source direction with respect to the baseline vector $\vec{\mathbf{b}}$ also changes which results in a sinusoidal variation (*fringes*) of the correlator response. Therefore, the correlator casts patterns of fringes of period $(2\pi\vec{\mathbf{b}'}.\hat{\mathbf{s}})$ onto the sky. The vector $\vec{\mathbf{b}'}$ is defined by $\vec{\mathbf{b}'} = \frac{\vec{\mathbf{b}}}{\lambda}$. The elements of the interferometer can generally measure both even and odd fringes which leads to

$$V' = \langle V_1 V_2^* \rangle = \frac{V^2}{2}[\cos(\omega\tau_g) - i\sin(\omega\tau_g)] = \frac{V^2}{2} e^{-2\pi i \vec{\mathbf{b}'}.\hat{\mathbf{s}}} \tag{2.27}$$

the complex fringe. Integrating this equation over the source size results in

$$V(\vec{\mathbf{b}'}) = \int\int_{\Omega} I(\hat{\mathbf{s}}) e^{-2\pi i \vec{\mathbf{b}'}.\hat{\mathbf{s}}} d\hat{\mathbf{s}} \tag{2.28}$$

the Van Cittert-Zernike theorem. In this case, Ω is the area of the source and $I = V^2/2$. Expressing the baseline coverage in terms of (u, v) coordinates[9], and the distribution of the source in terms of directional cosines (l, m), Eq. 2.28 can be represented in a useful two-dimensional Fourier transform thus

$$V(u, v) = \int\int_{\Omega} I(l, m) e^{-2\pi i(ul+vm)} dl\ dm \tag{2.29}$$

which is one of the fundamental equations in interferometry for measured visibilities $V(u, v)$. Eq. 2.29 tells us that the visibility V is a Fourier transform of the sky brightness distribution.

Sampling many (u, v) points, therefore, enhances the sky brightness distribution reconstruction, and to achieve this, many telescopes with different separations can be combined to form interferometers. Examples of such facilities include high resolution interferometers such as LOFAR and the VLA; I introduce these two telescopes in the next subsections. These two radio interferometers have delivered extraordinary results in the investigation of celestial objects such as RLAGN.

2.4.2 LOFAR

The LOw-Frequency ARray (LOFAR) is a facility built by the Netherlands Institute for Radio Astronomy (ASTRON). Its stations have reached a baseline of about 100 km in the Netherlands and consist of about 25 000 antenna dipoles concentrated in 52 stations, currently spread over ∼7 European countries. For radio observations, LOFAR is one of the largest interferometers in the world, offering high sensitivity and wide bandwidth observations at very low frequencies (120−168 MHz). One of the greatest capabilities of

[9] In radio astronomy, (u, v) coordinates refer to spatial frequencies (or wavelengths) of radio signals arriving at each antenna. Here the u-axis represents the east-west direction, whereas the north-south direction is represented by the v-axis (see Chapter 4 of Thompson et al., 2017). We can use these coordinates to calculate the interferometric baseline between two or more antennas to improve the uv coverage; the sensitivity of a radio telescope to large- and small-scale radio emission.

LOFAR is carrying out deep extragalactic large northern sky surveys at these frequencies. The LOFAR Two-meter Sky Survey (LoTSS; see respectively Chapters 4 and 5 on a summary of the first and second data release) has provided large extragalactic samples for a wide area at low frequencies both of RLAGN and SFGs (Shimwell et al., 2019, 2022).

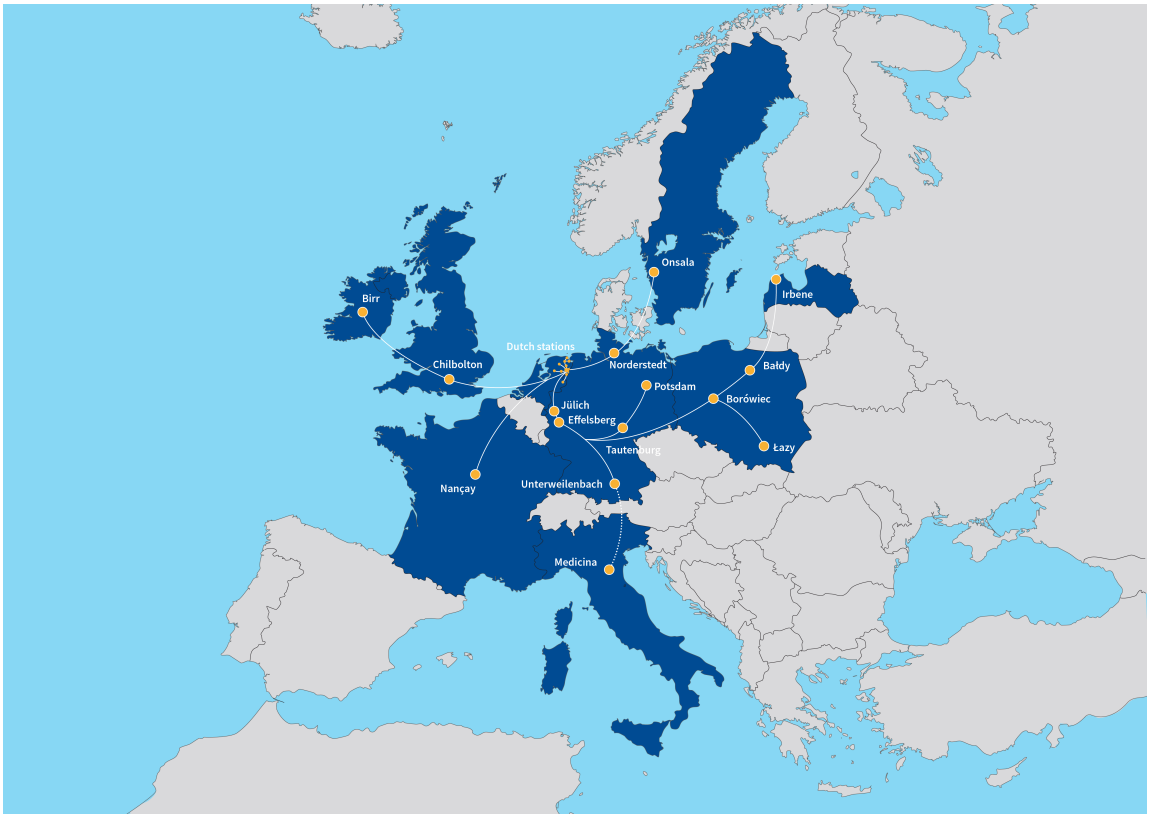

Figure 2.4: LOFAR stations across Europe. Credit: ASTRON.

2.4.3 The VLA

The Karl G. Jansky Very Large Array (herein referred to simply as the VLA) is an interferometer located in New Mexico, USA. It is managed by the National Radio Astronomy Observatory (NRAO). It comprises 28 (27 operational and 1 spare) parabolic single dishes (25 metres in diameter) capable of observations between 1 and 50 GHz. These antennas are mounted on a 'Y' shaped rail track allowing for a variety of array configurations (i.e. A, B, C, or D-configurations). It can be arranged in its most extended form with an array maximum antenna separation of up to 36 km (the A-configuration) or in its most compact array configuration (the D-configuration) with a maximum array antenna separation of up to 1 km. This flexibility enables us to *zoom* in and out to observe radio galaxies. The D-configuration allows us to detect diffuse emission, whereas the A-configuration allows for the detailed study of compact structures in radio galaxies. With multiple receivers available, the VLA's resolution depends on the observing frequency.

Figure 2.5: The Y-shaped VLA antennas are placed on rails to accommodate various array configurations, i.e. A, B, C, or D configurations. Credit: NRAO.

2.5 Project aim

In the present chapter, I have discussed various classes of AGNs, their unification, and their impact on galaxy formation and evolution. This thesis aims at studying the nature of low-luminosity compact RLAGN selected from the LOFAR AGN population and I hope to answer this aim with high-resolution VLA observations of these sources.

Chapter 3

The methodology

As mentioned in Chapter 2 (Sec. 2.4.1), the goal of recording observations with interferometers is to ensure that the true sky brightness is recovered by Fourier transforming the sampled visibilities. However, these visibilities contain uncorrelated signals that lead to amplitude and phase errors. To correct these errors which are also mixed with signals from other sources, a procedure known as *data reduction* has to be implemented. Data reduction consists of inspecting and flagging bad data, correcting phase and amplitude errors (calibration), reconstructing the true distribution of the sky brightness (deconvolution), and finally, but not always necessary, using a model of the image produced by deconvolution to further improve errors in phase and amplitude of the visibilities (self-calibration).

This Chapter briefly explores general VLA data reduction techniques using the Common Astronomy Software Applications (CASA). A summary of these procedures is represented by a flow chart in Sec. 3.1.6. The version of CASA used throughout this thesis is CASA 6.3.0.48.

3.1 CASA

CASA[1], developed by a group of international scientists of the National Radio Astronomical Observatory (NRAO)[2], the European Southern Observatory (ESO)[3], the National Astronomical Observatory of Japan (NAOJ)[4], the CSIRO Australia Telescope National Facility (CSIRO/ATNF)[5] and the Netherlands

[1] https://casaguides.nrao.edu/
[2] https://public.nrao.edu/
[3] https://www.eso.org/public/
[4] https://www.nao.ac.jp/en/about-naoj/
[5] https://www.csiro.au/en/about/facilities-collections/atnf

Institute for Radio Astronomy (ASTRON)[6] is an astronomical software package designed to reduce advanced radio astronomical observations from telescopes such as the VLA. The software is written in PYTHON[7] and C++[8] and consists of a range of data reduction tools that can be implemented interactively under an IPYTHON interface. This also gives the user an added advantage to running a set of commands at one time using a PYTHON script both interactively and non-interactively.

In the succeeding sections, I describe in detail CASA's set of commands and tools used for reduction procedures on VLA data used in this thesis.

3.1.1 Basic Data Inspection

Before data calibration, it is imperative to first inspect and establish the nature of the data as well as take into consideration any information provided by the observer during observations. For the VLA data used in this thesis, this information is accessed online by downloading the observer log[9]. Before data calibration, all reported issues should be taken into consideration.

3.1.1.1 List Observations

To determine the nature of the data, LISTOBS (list observations) task is used. This task lists all the information such as the name of the observer, date and time of observation, total integration time, number of spectral window IDs used, amplitude calibrator, phase calibrator(s), polarization calibrator, target sources, and so on.

3.1.1.2 Plot Antenna Positions

It is important to plot the configuration of the interferometer by using the task, PLOTANTS. This information is important in picking a reference antenna for data reduction techniques usually chosen from the middle of the configuration. After running PLOTANTS, our data was observed in the most extended array configuration, the A-configuration. This configuration is important for observations of compact sources.

3.1.1.3 Basic Data Editing

The final step in basic data inspection is data editing. Any issues reported from the observer's log (eg. faulty antennas) can be edited out using the task FLAGDATA. The setup scan, usually the first scan, is also

[6] https://www.astron.nl/
[7] https://www.python.org/
[8] https://cplusplus.com/
[9] http://www.vla.nrao.edu/cgi-bin/oplogs.cgi

edited out. In the final editing, it is common practice that initial samples ($\leq$10s) from the beginning of each scan be flagged as well (called quack flagging).

3.1.2 Radio Frequency Interference (RFI) Mitigation

After basic data inspection and editing based on a priori information, it is useful to further inspect the data using the data visualization tool PLOTMS. Plotting the data in amplitude versus time (or versus frequency) is a good idea to see if there are any obvious issues with the data. At this point, any amplitude spikes caused by Radio Frequency Interference (RFI) dominating a few spectral window IDs can be removed by the Hanning-smooth algorithm, which removes Gibbs ringing, using the task HANNINGSMOOTH[10]. A new MS file is created by this task. It is strongly recommended to back up your data using the task FLAGMANAGER before running the Hanning-smooth algorithm. Further RFI excision can be followed up with automated FLAGDATA in-built tasks such as TFCROP, before data calibration, and RFLAG, which works on calibrated data only.

3.1.3 Data Calibration

At this stage, we can begin calibrating the data by choosing a convenient reference antenna to be used throughout the entire calibration process. We can achieve this by various methods, one of which is setting the y-axis in PLOTMS to ANTENNA2. Antennas with missing data blocks are bad choices for a reference antenna. Also, it is standard to choose a reference antenna from the middle of the array.

To understand the calibration process better, the observed visibility V is presented in terms of frequency (f) and (u, v) coordinates thus

$$V_{i,j}(u, v, f) = b_{ij}(t)[B_j^*(f, t)]g_i(t)g_j(t)V_{i,j}(u, v, f)e^{i[\theta_i(t)-\theta_j(t)]} \tag{3.1}$$

here,

- g_i and θ_i are complex gains (i.e. amplitudes and phase portions) generally determined separately and,
- B_i is the complex bandpass (i.e. the equipment response of the receiver to specific signals at a certain frequency).

The general calibration process as seen from Eq. 3.1 is therefore deriving a series of corrections from calibrator sources which are then applied to science targets.

[10] https://casa.nrao.edu/docs/taskref/hanningsmooth-task.html

3.1.3.1 A Priori Antenna Position Corrections

The first data corrections to be derived are antenna positions using the task GENCAL. Recall from Sec. 3.1.3 Eq. 3.1 that the visibility V is a function of the (u, v) coordinates, knowing the exact positions of the VLA antennas is helpful in correctly correlating for each signal for a good estimation of the final image. The task GENCAL automatically looks for these corrections if antenna positions were updated into the NRAO online database[11] after the observation date.

3.1.3.2 Initial Flux Density Scaling

After correcting for antenna positions, we need to find all calibrator models using the task SETJY. Here, we provide a flux density value for the primary calibrator and at a later stage, transfer the flux density scaling to secondary and polarization calibrators. This is to determine the amplitude antenna gains (g_i from Eq. 3.1). Using SETJY, we locate the VLA standard model (at C-band) 3C286_C.im for our flux calibrator 3C286. We then apply this flux density standard solution with the task PERLEY-BUTLER 2017 (Perley and Butler, 2017).

3.1.3.3 Initial Phase Calibration

This step is usually carried out before solving for the bandpass. The task GAINCAL is used. Here we need to correct for phase variations before solving for the bandpass itself. This is to prevent de-correlation due to data averaging as phase variations occur on the bandpass calibrator from scan to scan at different elevations which may affect the final bandpass solution. Only a portion of middle channels (for a reasonable signal-to-noise ratio) is chosen from which to derive gain corrections. A small solution interval is also preferred to track phase changes.

3.1.3.4 Delay Calibration

The next step in building up to bandpass calibration is delay calibration. In this step, we solve antenna-based delays again using the task GAINCAL while choosing a convenient reference antenna. During this process, phase variations introduced by these delays against the frequency channel in each spectral window are corrected and this is achieved by avoiding channels at the edges of each spectral window as they may have low sensitivity.

[11] http://www.vla.nrao.edu/astro/archive/baselines/

3.1.3.5 Bandpass Calibration

Once the delays are corrected, we can proceed with solving the complex bandpass. The task used for this stage is BANDPASS. The main purpose here is to compensate for variations in receiver instrument response at specific frequencies. This calibration process hence involves measuring and correcting the parts of the gains that depend on frequency (B_i; Eq. 3.1). Since the bandwidth is split into channels, frequency variations will occur as the signals are transmitted partly due to frequency-dependent effects. To solve this problem, the solution interval is set such that all solutions for all times are combined while respecting scan boundaries. This accounts for variations of phase and amplitude with frequency.

3.1.3.6 Gain Calibration

In this step, we now derive complex antenna gain corrections (i.e. g_i and θ_i; Eq. 3.1). We achieve this by first deriving complex gain solutions for the amplitude calibrator and then deriving complex gain solutions for the phase calibrator (a position in the sky closer to the target). This way, we can determine appropriate solutions for the target source. We also derive complex gain corrections of the polarization calibrator.

3.1.3.7 Scaling the Amplitudes

The final stage of deriving calibration solutions is obtaining the true flux densities of phase and polarization (secondary) calibrators. The task FLUXSCALE is used to produce a properly-scaled amplitude gain calibration table for secondary calibrators. Since we determined the flux density of the primary (amplitude) calibrator (see Sec.3.1.3.2), we use this as our reference to compute the true flux density of the secondary calibrator.

3.1.3.8 Applying Calibration

Once all gain calibration solutions have been derived, the final stage is applying these solutions first to calibrator sources themselves (nearest interpolation), then to the target sources (linear interpolation). This is achieved by the task APPLYCAL. The results computed by this task are stored in the so-called CORRECTED_DATA column.

3.1.4 Preparing Calibrated Data for Imaging

The next stage after data calibration procedures described in Sec. 3.1.3 is preparing data for imaging (see Sec.3.1.4.1). However, traces of bad data may still be noticed. At this stage, we can utilise an

auto flagging tool in FLAGDATA's task, RFLAG. This task only works on calibrated data by utilising the CALIBRATED_DATA column. If bad data is still noticed, we can flag it interactively using PLOTMS.

Finally, we can split out sections of the data (target sources) from the measurement set's CORRECTED_DATA column using the task SPLIT in readiness for imaging. We can also take advantage of this task to average the data in time and/or in channel in order to save computation time. Once the target sources are split, we can utilise the STATWT task to correct data weights for the new measurement set (MS). This corrects for the effects due to relative noise scatter arising from flagging.

3.1.4.1 Data Imaging

Having split the target data, the CORRECTED_DATA column now becomes the new DATA column in our measurement set. Imaging in CASA utilises the task TCLEAN. This deconvolves the dirty beam (DB) from the image. We know that the visibility data V and the sky brightness (I) are Fourier transform pairs therefore, we can recast Eq. 2.29 as

$$I(l,m) = \int V(u,v)e^{[2\pi i(ul+vn)]}dudv \tag{3.2}$$

where u and v are baseline coordinates in wavelength units and m and l are sky directional cosines relating to the right ascension (l) and declination (m) for most VLA observations.

Imaging in CASA makes use of the task TCLEAN. This algorithm was first published by Högbom (1974). It deconvolves radio astronomy images by assuming that the sky (image) consists of a series of point sources. Högbom presented this algorithm to operate iteratively in the image plane and distinguish between real structures and sidelobes on the dirty map (DM) using the DB. To summarise their work, the algorithm works as follows:

1. find and compute the brightest value in the image,
2. then subtract the DB from the position of the brightest value.
3. Repeat (1) and (2) until the brightest value is indistinguishable from the noise level.

Several extensions and variations to the Högbom algorithm have been developed ever since. For example, the Clark (1980) algorithm (used in this thesis) presents the idea of cycles (major and minor cycles) to address the issues of computational time in performing the Högbom algorithm. This was achieved by introducing Fast Fourier Transforms (FFTs). Essentially, minor cycles work exactly like the procedure discussed in the Högbom algorithm. However,

1. only a beam area with the highest exterior sidelobe is selected,
2. points in the dirty image brighter than the beam's outermost sidelobe are selected then

3. the procedure outlined in the Högbom algorithm is performed using both the points and the beam selected in (1) and (2).

The major cycle proceeds by transforming and removing the so-called "clean" components computed in the minor cycle from the residual map in a single step using the FFT.

A few other settings have to be determined before data imagining can be implemented with TCLEAN. It is important to choose convenient imaging parameters for our split target sources. Some of the image parameters that we need to determine are CELL SIZE, IMSIZE, GRIDDER, DECONVOLVER, THRESHOLD, NITER, and WEIGHTING. To determine the CELL SIZE, we can capitalise on using the task PLOTMS in determining the maximum baseline (B_{max}) by plotting the amplitude versus uvwave (units of wavelengths) and pick the highest uv distance. Then we take advantage of Eq. 2.22 (angular resolution of an interferometer) to compute the angular size of each pixel (cell size) in our image. Effective cleaning can be achieved across the synthesized beam if we use 3-5 pixels (N_p). Therefore, building on Eq. 2.22, we can compute the cell size as:

$$\text{cell size} \approx \frac{180}{\pi N_p} \times \frac{\lambda}{B_{max}(\lambda)} (\text{arcsec}). \tag{3.3}$$

Next we determine the image size, IMSIZE. A good image size is one that is divisible by 2, 3, 5, and 7 (i.e. an image size of the order $2^n \times 10$, where n is an integer). A good image size would therefore be, 80, 160, 320, 640, 1280, 2560, or 5120. The image size should be large enough to remove PSF sidelobes and not too large enough to compromise deconvolution performance.

To determine the choice of a deconvolution algorithm, DECONVOLVER, the source and interferometer configuration have to be considered. For our data observed in the A configuration, it is expected that the source is a compact source hence choosing the CLARK or HÖGBOM method should work just fine. A rule of thumb is if the total bandwidth divided by the central frequency is less than 10% ($BW/v_c < 10\%$), choose the CLARK algorithm, otherwise choose the MTMFS algorithm. For extended sources, we can consider choosing the MULTISCALE[12] algorithm and setting the SCALES parameter.

3.1.5 Self-calibration

The so-called self-calibration follows the same standard as the data calibration procedures described above. Here, however, we concentrate only on the target source. Recall from Sec. 3.1.3 that we derived approximate phase and amplitude solutions using calibrator sources, here, we want to improve upon this by using a model created from imaging the target itself to correct errors due to atmospheric variations between phase calibrators and target sources. Self-calibration uses the tasks TCLEAN, GAINCAL, and APPLYCAL. It can be summarised as follows:

[12] See reviews by, for example, Cornwell (2008).

1. create a model image using TCLEAN,
2. derive gain corrections using GAINCAL by choosing a good solution interval,
3. then apply gain solutions with APPLYCAL.
4. Re-image (TCLEAN) to obtain the final image.

However, it is important to know that self-calibration demands patience while changing and adjusting different parameters to obtain good results. For further details on when to use self-calibration see CASA's cookbooks[13].

3.1.6 Data reduction and calibration summary

A flow chart summarising the entire data reduction and calibration procedure is presented in Figure 3.1.

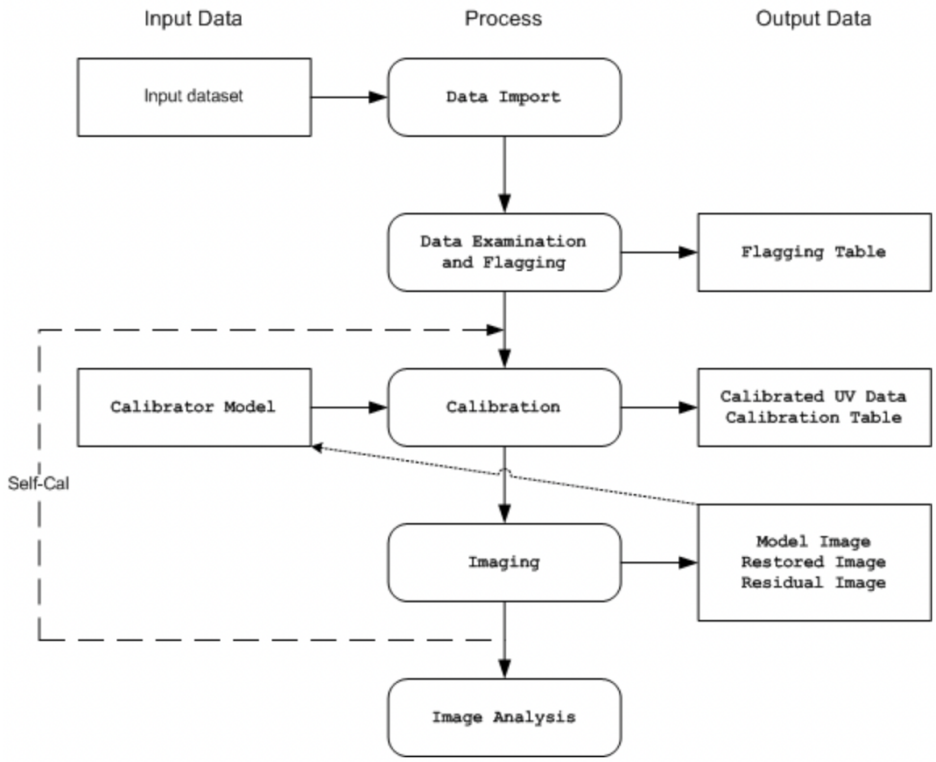

Figure 3.1: A flow chart summarising data reduction and calibration procedures presented in this Chapter. Credit: NRAO

[13] https://casa.nrao.edu/casa_cookbook.pdf

Chapter 4

Low-luminosity compact RLAGN

4.1 Introduction

One of the most important reasons for studying the jets of powerful RLAGN (e.g the Fanaroff and Riley, 1974, FRI/II sources) stems from the drive to understand their impact on galaxy formation and evolution through AGN feedback models (see Morganti et al., 2005a,b; Croton et al., 2006; Somerville and Davé, 2015; Hardcastle and Croston, 2020, see also Chapter 2 for a summary on AGN feedback). Recently, an interest in studying physically small (less than 100 kpc) RLAGN and their impact on their surroundings (e.g. Jarvis et al., 2019; Ubertosi et al., 2021) has emerged. These objects range from powerful yet compact RLAGN (e.g. CSS/GPS objects; Bicknell et al., 2018; O'Dea and Saikia, 2021) to low-radio power yet resolved galaxy scale jets (GSJs; Webster et al., 2021a,b) and low-radio power compact RLAGN, the so-called Fanaroff-Riley class 0 sources ('FR0s'; see Baldi and Capetti, 2010; Baldi et al., 2015, 2016; Baldi et al., 2018). Thanks to LoTSS, we can detect these objects in large numbers at low frequencies (150 MHz). In this Chapter, I present high-resolution (0.35 arcsec) 6 GHz VLA observations of a sample of 55 low-radio power compact RLAGN selected from the LOFAR AGN population based on LoTSS DR1.

4.1.1 The LoTSS DR1

The LoTSS DR1 (Shimwell et al., 2019) – a brief description of DR2 (Shimwell et al., 2022) is given in Chapter 5 – provided a catalogue of 318 520 radio sources both of SFGs and RLAGN after artefact rejection and source association/deblending. LoTSS DR1 consists of 424 deg^2 of data in the region

of the HETDEX[1] (e.g. Gebhardt et al., 2021) Spring field at right ascension and declination between $160° < \mathrm{RA} < 230°$ and $45° < \mathrm{Dec} < 57°$ respectively. It consists of 6 arcsec resolution observations with a median RMS value of around 70 μJy beam^{-1}. The 318 520 sources were optically identified using PanSTARRS[2](Kaiser et al., 2002) and WISE[3](Wright et al., 2010) data resulting in a 72% identification fraction (see Williams et al., 2019, and references therein). For radio objects where the observed spectral index is typically $\alpha = -0.7$, the LoTSS survey is approximately ten times deeper than FIRST[4] (Becker et al., 1995) and NVSS[5] (Condon et al., 1998) surveys. LOFAR's short and long baselines can be combined to make it more sensitive in observing both compact and extended sources in the radio sky.

Despite significant advances and developments in hardware and software for radio astronomy, a major challenge remains in understanding RLAGN emitting at much lower radio luminosities. This is mostly because SFGs are also known to emit at radio wavelengths which result in an overlap of radio luminosities with RLAGN (Condon, 1992). SFGs are known to dominate radio sources below flux densities of 10 mJy (e.g. Windhorst et al., 1985; Afonso et al., 2005; Wilman et al., 2008), whereas RLAGN dominates at higher flux density values (e.g. Condon, 1984; Magliocchetti et al., 2000). RLAGN separation from SFGs remains a key challenge and to successfully study them with radio instruments such as LOFAR, models to separate RLAGN from SFGs have since been developed. It is worth describing some of these separation models in brief below.

4.1.2 AGN-SF separation

The LoTSS DR1 RLAGN sub-sample studied in this thesis was constructed by Hardcastle et al. using the AGN-SF separation methods of Sabater et al. (2019). A brief description of those methods follows here.

The best AGN-SF separation method would make use of the radio excess of RLAGN over the emission expected from the measured SFR. This proposes selecting RLAGN if and only if their radio emission exceeds the emission expected to result from SF (e.g. Hardcastle et al., 2016). This method, however, requires good SFR information (e.g Gürkan et al., 2018; Smith et al., 2021) to be practical, which are unavailable at the moment for sources in the HETDEX field. This leaves us with other AGN-SF methods that rely on diagnostic diagrams. The first and most common AGN separation model was developed by Baldwin et al. (1981). In this method, line diagnostic diagrams are used to select extragalactic sources using their emission lines in the optical. However, this method depends on sources with clear emission line detections, and not all low-luminosity RLAGN would show as AGN on these line diagnostic diagrams. In the second method proposed by Machalski and Condon (1999), radio and far-infrared luminosities of sources are compared. The method typically relies on the FIRC[6] of SFGs. The third method describes the

[1] The Hobby-Eberly Telescope Dark Energy Experiment.
[2] The Panoramic Survey Telescope and Rapid Response System.
[3] The Wide Field Sky Explorer.
[4] The Faint Images of the Radio Sky at Twenty Centimetres.
[5] The NRAO VLA Sky Survey.
[6] The tight far-infrared radio correlation.

comparison of the ratio of the radio luminosity per unit of stellar mass against the 4000Å break strength (Best et al., 2005b). Kauffmann et al. (2008) further built upon this method by considering the ratio of the radio luminosity against the Hα luminosity. Using these models, Sabater et al. (2019) modified and extended the works of Best and Heckman (2012) resulting in the W2-W3 WISE colour model. This proposes that SFGs separate from hosts of RLAGN in their WISE colours (e.g. Wright et al., 2010). These AGN-SF separation methods have limitations and selection effects which can be reduced by applying as many methods as possible and then cross-matching them to obtain a purer sample of radiative AGN; I return to this point in Sec. 4.2.

This thesis utilises a larger sample of RLAGN derived from LoTSS DR1. Hardcastle et al. (2019) constructed this sample by extending the works of Best et al. (2005b) to much lower radio luminosity ($L_{150\ \mathrm{MHz}} > 10^{21}\ \mathrm{WHz}^{-1}$) levels detectable by LOFAR using spectroscopic and photometric techniques. To summarise their selection criteria, the starting point is the LoTSS DR1 consisting of the full (F) sample of 318 520 radio sources. Objects were selected such that they contain a Flux-complete (FC, 0.5 mJy flux cut) as well as Optical ID information (O), spectroscopic redshifts (Z), and 'Good' photometric redshift estimates (ZG) (see Wright et al., 2010; Chambers et al., 2016; Williams et al., 2019; Duncan et al., 2019). This resulted in 71 955 (FCOZG) radio sources. A cross-match of this sample with the MPA-JHU[7] sample resulted in 12 803 (FCOZGM) radio sources. 3706 RLAGN were selected from the FCOZGM sample with the remaining 9097 radio sources selected as SFGs and removed. Further, radio sources with WISE colours consistent with SFGs colours were removed together with those without available WISE data unless those that satisfied these conditions: their radio luminosities greater than $10^{25}\,\mathrm{W\,Hz}^{-1}$ at 150 MHz, K_s band magnitudes greater than -25 for non-quasars, and K_s band rest-frame magnitude less than -25 for quasars. Their radio luminosities should also be defined by $\log_{10}(L_{150}) > 25.3 - 0.06(25 + K_s)$. Applying these mechanisms, therefore, resulted in 23 344 RLAGN sources (see Fig. 4.1). Hardcastle et al. (2019) noted that this AGN-SF separation criterion does not provide an ideal RLAGN sample considering that there is an overlap in RLAGN and SF sources due to errors in the WISE colours[8], however, the most reliable RLAGN are those selected by spectroscopic methods.

Using analytical models derived by Hardcastle (2018b), Hardcastle et al. (2019) used the RLAGN sample to construct a power-linear size diagram in which they showed that while the distribution of the projected physical sizes at the more luminous end of the AGN population is consistent with a uniform lifetime function distribution (distribution of possible jet active times), the class of low-luminosity compact RLAGN [which are numerically dominant and many of them are physically very small ($<$100 kpc) in projected physical scales] may require a different model from the more powerful and better-understood large objects. In addition, a model in which low-luminosity compact objects are the young counterparts of the more powerful sources is rejected unless most of these objects at these luminosities do not survive to old age. A plausible speculation, however, is that they could be the low-jet-power continuation of the more

[7] https://wwwmpa.mpa-garching.mpg.de/SDSS/DR7/

[8] A majority of sources in the WISE W3 band, in particular, are non-detections and their sizes are upper limits. This does not affect the selection of RLAGN as their values can not be arbitrarily lower than the set limits; however, these sources are expected to be positioned further away to the left side of Fig. 4.1.

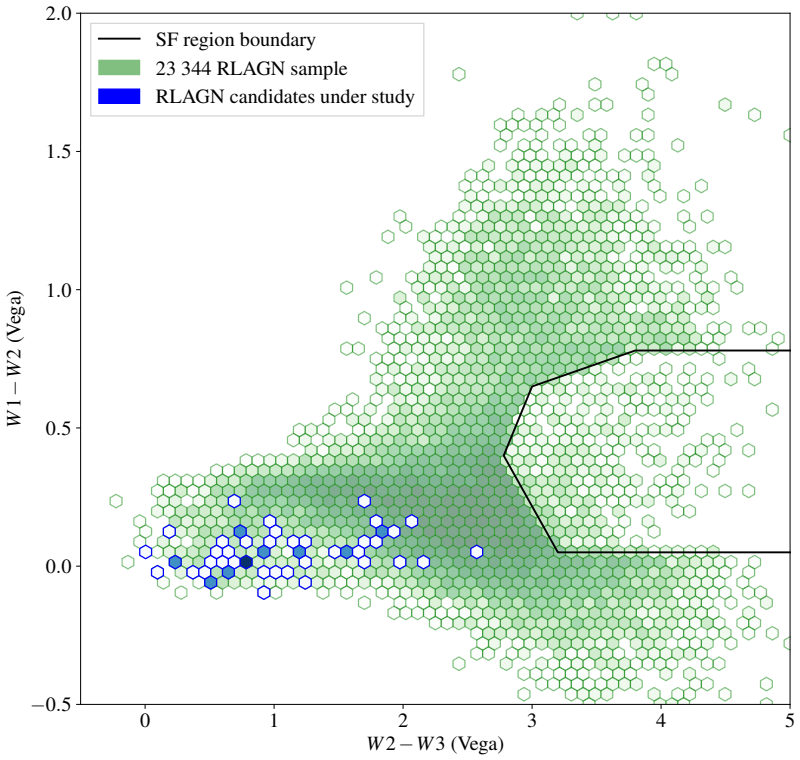

Figure 4.1: The final 23 344 RLAGN selected by Hardcastle et al. following a WISE AGN-SF separation technique based on WISE colours. Green points show the whole RLAGN sample overlaid with the position of RLAGN sub-sample under study (see Sec. 4.2 describing the construction of the LOFAR sub-sample). WISE AB magnitudes have been converted to Vega magnitudes. The line (black) boundary indicates the locus of points where SFGs dominate in WISE colours. Note that some of the sources on this plot are upper limits, particularly in the WISE W3 band. This does not affect the selection criteria for these sources as the set limits can not be arbitrarily lower than those limits; however, these sources are expected to be further away to the left side than shown.

luminous and larger RLAGN, and if this is the case, then we may be underestimating the input energy that they may be injecting into massive galaxies. Similar physically small, compact objects on galaxy scales ('FR0s') have previously been studied (Baldi and Capetti, 2010; Baldi et al., 2015, 2016; Baldi et al., 2018): as yet, little is known about how they contribute to AGN feedback. However, LOFAR's short baselines give us an added advantage in selecting these objects in a simple and homogeneous way without missing significant extended emission and we can robustly remove SF sources thanks to our excellent ancillary data.

I aim to investigate the nature of these ubiquitous low-luminosity compact RLAGN inhabiting massive galaxies. Are these low-luminosity RLAGN scaled-down versions of the better understood AGN populations that we see at high luminosities with double lobes inflating bubbles in the IGM, or are they morphologically different? On what scales do they affect the IGM of the host galaxy?

I aim to answer these questions using VLA observations of low-luminosity compact RLAGN selected from LoTSS DR1.

4.2 The LoTSS data

In this subsection, I summarise the construction of a sub-sample of 55 low-luminosity compact RLAGN by Hardcastle et al.. These objects were selected based on their compact nature in LoTSS DR1. The authors then obtained high-resolution VLA observations of these sources (see Sec. 4.3) which I analyse using a new set of high-quality LoTSS DR2 images (Shimwell et al., 2022).

To investigate the nature of these compact objects, Hardcastle et al. carefully and conservatively constructed a LOFAR sub-sample of 55 RLAGN candidates based on LoTSS DR1. They started by (1) selecting all DR1 sources cross-matched with the MPA-JHU value-added SDSS catalogue (Brinchmann et al., 2004) as described above, and took all the 3706 objects classed as RLAGN derived from the FCOZGM sample (Hardcastle et al., 2019) using the 4 AGN-SF separation methods of Sabater et al. (2019) that is (i) the Best et al. D_{4000} vs $L_{150}/M*$ method, (ii) the Baldwin et al. 'BPT' diagnostic diagram ([OIII]/Hβ vs [NII]/Hα) method, (iii) the Machalski and Condon $L_{H\alpha}$ vs L_{150} method, and (iv) the WISE colour model (W1-W2 vs W2-W3); this is summarised in Fig. 4.2. (2) To get the best spatial resolution, objects unresolved by LOFAR and with redshifts of $z < 0.1$ (see Fig. 4.3) were selected to ensure that we have no ambiguities in their AGN classification (i.e. no contamination from SF). Further (3), they selected sources with a LOFAR peak flux density of $S_{150\ \mathrm{MHz}} > 2$ mJy per beam, which has the dual effect of ensuring a high SNR-LOFAR detection and permitting VLA detections. These criteria (1$-$3) resulted in 55 low-redshift, low-luminosity compact RLAGN candidates (all of which are radiatively efficient AGN: HERGs). Their basic properties are presented in Table 4.1.

I then used high resolution sub-arcsecond VLA observations obtained by Hardcastle et al. to resolve these RLAGN candidates on sub-kpc scales ($\leq$100 kpc); the VLA images give us the opportunity to see a decomposition between cores, jets, and lobes (if any) on sub-kpc scales.

4.3 The VLA data

The VLA observations were recorded by Hardcastle et al. in the A configuration across two identical four-hour observation sessions during September 2019 at C-band (i.e. 4$-$8 GHz). For brevity's sake, I refer to these observations as epochs 1 and 2. Allowing for calibration and slewing overhead, the two identical four-hour sessions were scheduled such that the observations for each target were achieved in two three-minute observing blocks to improve the snapshot uv coverage. See Table 4.2 for the summary of these observations.

These observations were made using one of the primary VLA calibrators 3C286[9] and five phase calibrators: J1035+5628, J1146+5356, J1219+4829, J1349+5341, and J1419+5423 chosen for proximity to the targets. A summary of calibrator sources for the data used in this thesis is shown in Table 4.3.

[9]The flux calibrator.

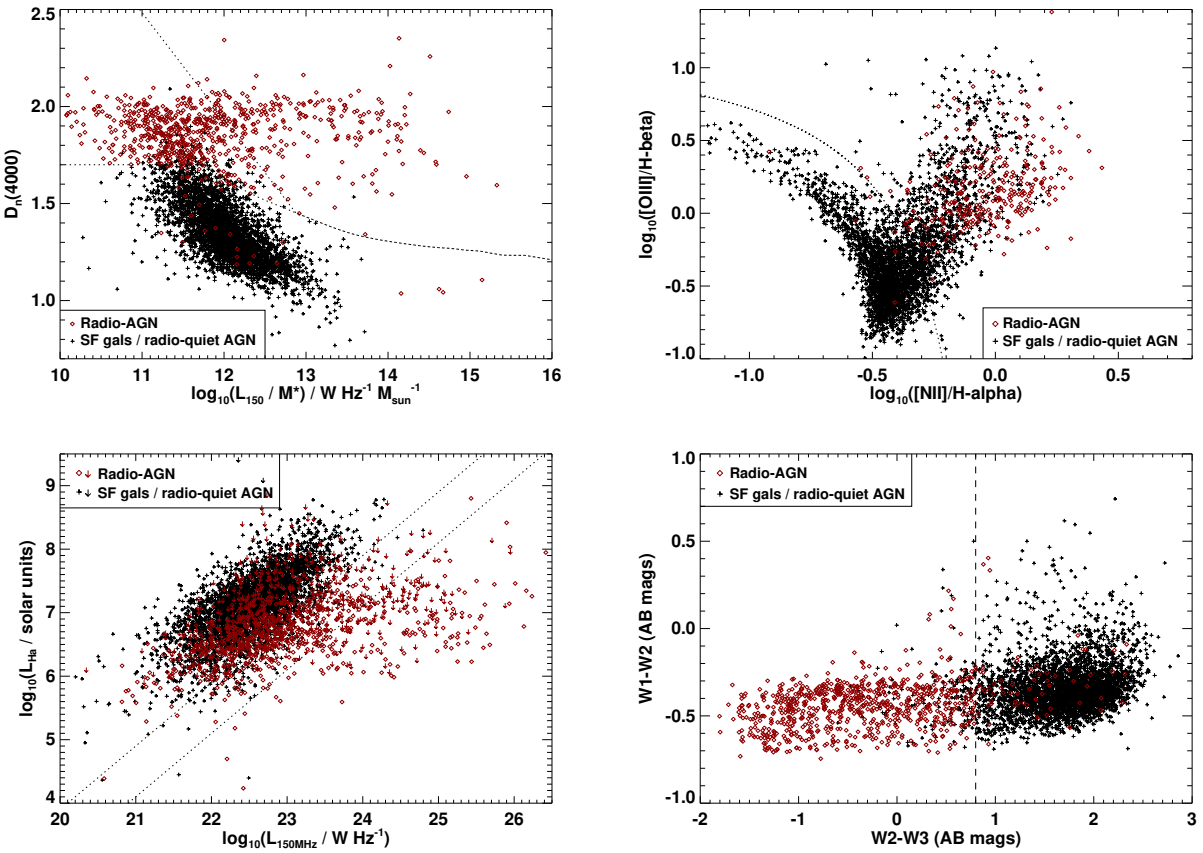

Figure 4.2: Figure is extracted from Sabater et al.. This follows the AGN-SF separation techniques met by the RLAGN studied in this thesis. *Top panel from left to right* respectively: AGN-SF method presented by Best et al. (2005b) thus the 4000Å vs $L_{150\ \mathrm{MHz}}/\mathrm{M}*$ and the Baldwin et al. (1981) emission line ratio method thus [OIII]/Hβ vs [NII]/Hα. *Bottom panel from left to right* respectively: comparison of $L_{\mathrm{H}\alpha}$ vs $L_{150\ \mathrm{MHz}}$ luminosities and the WISE colour-colour model (W1-W2 vs W2-W3).

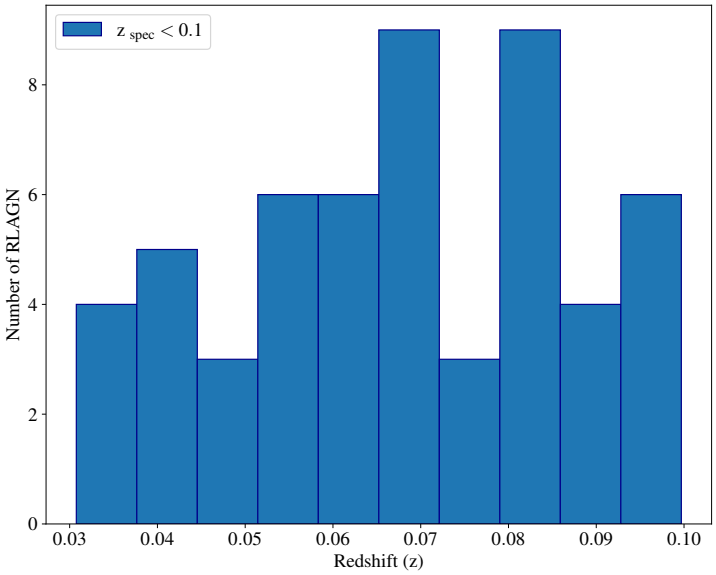

Figure 4.3: A histogram distribution of spectroscopic redshifts ($0.03 < z < 0.1$).

Table 4.1: Basic information about the 55 RLAGN candidates selected from the LOFAR AGN population at 150 MHz. The first column shows the full LOFAR source name for the objects with abbreviations shown in brackets for in-text discussions. RLAGN candidates are arranged in order of increasing right ascension (RA).

LOFAR source name		Right ascension	Declination	Redshift	Total flux 150 MHz	Peak flux 150 MHz	Radio luminosity $L_{150\ \mathrm{MHz}}$	Optical luminosity r-band
		RA	DEC	(z, spec)	(S_{int}, mJy)	(S_{p}, mJy)	(W Hz^{-1})	(W)
ILTJ104852.93+480314.8	(J1048+48)	$10^{\mathrm{h}}48^{\mathrm{m}}52.93^{\mathrm{s}}$	$+48°03'14.8''$	0.041	66.88 ± 0.328	64.01 ± 0.134	2.59×10^{23}	1.06×10^{37}
ILTJ105535.82+462903.3	(J1055+46)	$10^{\mathrm{h}}55^{\mathrm{m}}35.82^{\mathrm{s}}$	$+46°29'03.3''$	0.089	3.859 ± 0.123	3.681 ± 0.072	7.49×10^{22}	2.11×10^{37}
ILTJ110233.62+513124.3	(J1102+51)	$11^{\mathrm{h}}02^{\mathrm{m}}33.62^{\mathrm{s}}$	$+51°31'24.3''$	0.069	6.402 ± 0.099	5.054 ± 0.061	7.19×10^{22}	3.49×10^{37}
ILTJ111156.65+555449.9	(J1111+55)	$11^{\mathrm{h}}11^{\mathrm{m}}56.65^{\mathrm{s}}$	$+55°54'49.9''$	0.071	5.396 ± 0.152	3.207 ± 0.102	6.43×10^{22}	1.61×10^{37}
ILTJ111712.10+465135.6	(J1117+46)	$11^{\mathrm{h}}17^{\mathrm{m}}12.10^{\mathrm{s}}$	$+46°51'35.6''$	0.061	12.58 ± 0.121	11.61 ± 0.071	1.10×10^{23}	3.77×10^{37}
ILTJ111745.92+473327.5	(J1117+47)	$11^{\mathrm{h}}17^{\mathrm{m}}45.92^{\mathrm{s}}$	$+47°33'27.5''$	0.075	27.76 ± 0.155	20.85 ± 0.082	3.72×10^{23}	3.96×10^{37}
ILTJ112625.15+520503.6	(J1126+52)	$11^{\mathrm{h}}26^{\mathrm{m}}25.15^{\mathrm{s}}$	$+52°05'03.6''$	0.048	25.32 ± 0.307	19.61 ± 0.116	1.36×10^{23}	6.95×10^{36}
ILTJ113545.33+491619.6	(J1135+49)	$11^{\mathrm{h}}35^{\mathrm{m}}45.33^{\mathrm{s}}$	$+49°16'19.6''$	0.053	4.777 ± 0.127	3.379 ± 0.081	3.11×10^{22}	1.10×10^{37}
ILTJ113757.19+554207.5	(J1137+55)	$11^{\mathrm{h}}37^{\mathrm{m}}57.19^{\mathrm{s}}$	$+55°42'07.5''$	0.062	3.612 ± 0.121	3.522 ± 0.070	3.31×10^{22}	1.95×10^{37}
ILTJ114047.35+463225.5	(J1140+46)	$11^{\mathrm{h}}40^{\mathrm{m}}47.35^{\mathrm{s}}$	$+46°32'25.5''$	0.054	8.135 ± 0.131	5.733 ± 0.084	5.47×10^{22}	4.26×10^{36}
ILTJ114316.26+551639.9	(J1143+55)	$11^{\mathrm{h}}43^{\mathrm{m}}16.26^{\mathrm{s}}$	$+55°16'39.9''$	0.055	25.05 ± 0.249	18.18 ± 0.095	1.77×10^{23}	6.59×10^{36}
ILTJ114721.40+554348.4	(J1147+55)	$11^{\mathrm{h}}47^{\mathrm{m}}21.40^{\mathrm{s}}$	$+55°43'48.4''$	0.052	3.286 ± 0.132	2.557 ± 0.083	2.04×10^{22}	2.68×10^{37}
ILTJ115113.46+550659.0	(J1151+55)	$11^{\mathrm{h}}51^{\mathrm{m}}13.46^{\mathrm{s}}$	$+55°06'59.0''$	0.079	8.184 ± 0.251	5.198 ± 0.165	1.24×10^{23}	–
ILTJ115157.87+532845.5	(J1151+53)	$11^{\mathrm{h}}51^{\mathrm{m}}57.87^{\mathrm{s}}$	$+53°28'45.5''$	0.060	3.910 ± 0.113	3.046 ± 0.070	3.26×10^{22}	1.74×10^{37}
ILTJ115205.79+545817.1	(J1152+54)	$11^{\mathrm{h}}52^{\mathrm{m}}05.79^{\mathrm{s}}$	$+54°58'17.1''$	0.060	11.16 ± 0.162	8.906 ± 0.069	9.47×10^{22}	1.01×10^{37}
ILTJ115330.55+524121.8	(J1153+52)	$11^{\mathrm{h}}53^{\mathrm{m}}30.55^{\mathrm{s}}$	$+52°41'21.8''$	0.072	33.95 ± 0.332	28.05 ± 0.148	4.16×10^{23}	5.74×10^{37}
ILTJ115438.10+491851.4	(J1154+49)	$11^{\mathrm{h}}54^{\mathrm{m}}38.10^{\mathrm{s}}$	$+49°18'51.4''$	0.054	4.849 ± 0.103	4.525 ± 0.061	3.30×10^{22}	1.24×10^{37}
ILTJ115531.40+545200.4	(J1155+54)	$11^{\mathrm{h}}55^{\mathrm{m}}31.40^{\mathrm{s}}$	$+54°52'00.4''$	0.050	12.93 ± 1.348	12.71 ± 0.749	7.42×10^{22}	1.15×10^{37}
ILTJ115952.14+553205.5	(J1159+55)	$11^{\mathrm{h}}59^{\mathrm{m}}52.14^{\mathrm{s}}$	$+55°32'05.5''$	0.081	5.343 ± 0.122	3.419 ± 0.081	8.41×10^{22}	1.44×10^{38}
ILTJ120328.53+514256.3	(J1203+51)	$12^{\mathrm{h}}03^{\mathrm{m}}28.53^{\mathrm{s}}$	$+51°42'56.3''$	0.061	4.855 ± 0.120	3.441 ± 0.077	4.24×10^{22}	4.02×10^{37}
ILTJ120801.00+523635.3	(J1208+52)	$12^{\mathrm{h}}08^{\mathrm{m}}01.00^{\mathrm{s}}$	$+52°36'35.3''$	0.082	2.935 ± 0.130	2.459 ± 0.079	4.71×10^{22}	1.66×10^{37}
ILTJ121329.29+504429.4	(J1213+50)	$12^{\mathrm{h}}13^{\mathrm{m}}29.29^{\mathrm{s}}$	$+50°44'29.4''$	0.031	187.0 ± 0.777	162.4 ± 0.270	4.03×10^{23}	–
ILTJ123011.86+470022.7	(J1230+47)	$12^{\mathrm{h}}30^{\mathrm{m}}11.86^{\mathrm{s}}$	$+47°00'22.7''$	0.039	102.7 ± 0.453	86.99 ± 0.194	3.61×10^{23}	1.16×10^{37}
ILTJ123301.22+561013.7	(J1233+56)	$12^{\mathrm{h}}33^{\mathrm{m}}01.22^{\mathrm{s}}$	$+56°10'13.7''$	0.081	2.784 ± 0.160	2.643 ± 0.094	4.42×10^{22}	3.45×10^{37}
ILTJ124021.48+475143.6	(J1240+47)	$12^{\mathrm{h}}40^{\mathrm{m}}21.48^{\mathrm{s}}$	$+47°51'43.6''$	0.098	10.26 ± 0.153	8.335 ± 0.067	2.42×10^{23}	5.09×10^{37}
ILTJ124343.52+544902.0	(J1243+54)	$12^{\mathrm{h}}43^{\mathrm{m}}43.52^{\mathrm{s}}$	$+54°49'02.0''$	0.085	6.820 ± 0.179	5.242 ± 0.063	1.18×10^{23}	3.29×10^{37}
ILTJ125827.27+501650.6	(J1258+50)	$12^{\mathrm{h}}58^{\mathrm{m}}27.27^{\mathrm{s}}$	$+50°16'50.6''$	0.099	2.833 ± 0.107	2.293 ± 0.066	6.88×10^{22}	6.91×10^{37}
ILTJ130325.87+523522.5	(J1303+52)	$13^{\mathrm{h}}03^{\mathrm{m}}25.87^{\mathrm{s}}$	$+52°35'22.5''$	0.096	9.790 ± 0.152	8.570 ± 0.064	2.19×10^{23}	2.10×10^{37}
ILTJ130404.58+492728.5	(J1304+49)	$13^{\mathrm{h}}04^{\mathrm{m}}04.58^{\mathrm{s}}$	$+49°27'28.5''$	0.033	5.644 ± 0.110	3.497 ± 0.073	1.43×10^{22}	2.63×10^{36}
ILTJ130410.78+552839.0	(J1304+55)	$13^{\mathrm{h}}04^{\mathrm{m}}10.78^{\mathrm{s}}$	$+55°28'39.0''$	0.082	3.896 ± 0.116	3.449 ± 0.069	6.27×10^{22}	8.99×10^{37}
ILTJ130535.92+540142.5	(J1305+54)	$13^{\mathrm{h}}05^{\mathrm{m}}35.92^{\mathrm{s}}$	$+54°01'42.5''$	0.091	23.84 ± 0.236	20.60 ± 0.080	4.78×10^{23}	4.37×10^{37}
ILTJ131002.06+540005.2	(J1310+54)	$13^{\mathrm{h}}10^{\mathrm{m}}02.06^{\mathrm{s}}$	$+54°00'05.2''$	0.089	2.677 ± 0.112	2.279 ± 0.068	5.14×10^{22}	5.08×10^{37}
ILTJ131015.19+544004.8	(J1310+54)	$13^{\mathrm{h}}10^{\mathrm{m}}15.19^{\mathrm{s}}$	$+54°40'04.8''$	0.064	5.593 ± 0.114	5.027 ± 0.068	5.38×10^{22}	2.09×10^{37}
ILTJ132745.67+544756.8	(J1327+54)	$13^{\mathrm{h}}27^{\mathrm{m}}45.67^{\mathrm{s}}$	$+54°47'56.8''$	0.033	10.73 ± 0.176	9.195 ± 0.073	2.67×10^{22}	5.61×10^{36}
ILTJ133430.04+502718.3	(J1334+50)	$13^{\mathrm{h}}34^{\mathrm{m}}30.04^{\mathrm{s}}$	$+50°27'18.3''$	0.085	3.052 ± 0.108	2.735 ± 0.065	5.32×10^{22}	5.10×10^{37}
ILTJ134227.94+554939.3	(J1342+55)	$13^{\mathrm{h}}42^{\mathrm{m}}27.94^{\mathrm{s}}$	$+55°49'39.3''$	0.072	4.969 ± 0.121	3.354 ± 0.078	6.13×10^{22}	8.69×10^{36}
ILTJ134233.86+485316.2	(J1342+48)	$13^{\mathrm{h}}42^{\mathrm{m}}33.86^{\mathrm{s}}$	$+48°53'16.2''$	0.091	7.454 ± 0.113	6.245 ± 0.069	1.50×10^{23}	7.20×10^{37}
ILTJ134345.04+553801.3	(J1343+55)	$13^{\mathrm{h}}43^{\mathrm{m}}45.04^{\mathrm{s}}$	$+55°38'01.3''$	0.068	3.031 ± 0.124	2.374 ± 0.077	3.36×10^{22}	4.41×10^{37}
ILTJ135632.65+493710.9	(J1356+49)	$13^{\mathrm{h}}56^{\mathrm{m}}32.65^{\mathrm{s}}$	$+49°37'10.9''$	0.066	3.886 ± 0.110	3.361 ± 0.067	4.00×10^{22}	1.85×10^{37}
ILTJ140013.20+462556.0	(J1400+46)	$14^{\mathrm{h}}00^{\mathrm{m}}13.20^{\mathrm{s}}$	$+46°25'56.0''$	0.053	3.792 ± 0.097	3.334 ± 0.058	2.51×10^{22}	7.16×10^{36}
ILTJ140906.86+532749.1	(J1409+53)	$14^{\mathrm{h}}09^{\mathrm{m}}06.86^{\mathrm{s}}$	$+53°27'49.1''$	0.078	22.28 ± 0.279	16.84 ± 0.130	3.27×10^{23}	3.93×10^{37}
ILTJ141118.46+551053.2	(J1411+55)	$14^{\mathrm{h}}11^{\mathrm{m}}18.46^{\mathrm{s}}$	$+55°10'53.2''$	0.042	26.93 ± 0.213	21.86 ± 0.092	1.10×10^{23}	1.27×10^{37}
ILTJ141149.57+545733.1	(J1411+54)	$14^{\mathrm{h}}11^{\mathrm{m}}49.57^{\mathrm{s}}$	$+54°57'33.1''$	0.083	4.127 ± 0.162	4.111 ± 0.094	6.96×10^{22}	5.26×10^{37}
ILTJ141234.88+494611.5	(J1412+49)	$14^{\mathrm{h}}12^{\mathrm{m}}34.88^{\mathrm{s}}$	$+49°46'11.5''$	0.071	4.331 ± 0.169	3.135 ± 0.108	5.19×10^{22}	2.47×10^{37}
ILTJ141422.37+553520.5	(J1414+55)	$14^{\mathrm{h}}14^{\mathrm{m}}22.37^{\mathrm{s}}$	$+55°35'20.5''$	0.077	2.719 ± 0.132	2.182 ± 0.082	3.86×10^{22}	2.34×10^{37}
ILTJ142025.23+544016.1	(J1420+54)	$14^{\mathrm{h}}20^{\mathrm{m}}25.23^{\mathrm{s}}$	$+54°40'16.1''$	0.042	2.879 ± 0.120	2.006 ± 0.077	1.16×10^{22}	4.78×10^{36}
ILTJ142125.51+482933.3	(J1421+48)	$14^{\mathrm{h}}21^{\mathrm{m}}25.51^{\mathrm{s}}$	$+48°29'33.3''$	0.072	8.493 ± 0.163	6.472 ± 0.102	1.04×10^{23}	3.84×10^{37}
ILTJ142255.56+474713.9	(J1422+47)	$14^{\mathrm{h}}22^{\mathrm{m}}55.56^{\mathrm{s}}$	$+47°47'13.9''$	0.072	3.416 ± 0.134	2.836 ± 0.082	4.21×10^{22}	3.89×10^{37}
ILTJ142707.30+525001.5	(J1427+52)	$14^{\mathrm{h}}27^{\mathrm{m}}07.30^{\mathrm{s}}$	$+52°50'01.5''$	0.083	8.372 ± 0.179	7.271 ± 0.108	1.41×10^{23}	1.63×10^{37}
ILTJ142948.48+535754.2	(J1429+53)	$14^{\mathrm{h}}29^{\mathrm{m}}48.48^{\mathrm{s}}$	$+53°57'54.2''$	0.043	3.554 ± 0.192	2.881 ± 0.118	1.53×10^{22}	1.24×10^{37}
ILTJ143334.77+524310.2	(J1433+52)	$14^{\mathrm{h}}33^{\mathrm{m}}34.77^{\mathrm{s}}$	$+52°43'10.2''$	0.045	3.840 ± 0.142	2.730 ± 0.090	1.81×10^{22}	9.02×10^{36}
ILTJ143521.75+505123.0	(J1435+50)	$14^{\mathrm{h}}35^{\mathrm{m}}21.75^{\mathrm{s}}$	$+50°51'23.0''$	0.100	339.0 ± 2.285	264.7 ± 0.763	8.30×10^{24}	5.90×10^{37}
ILTJ145350.18+540440.9	(J1453+54)	$14^{\mathrm{h}}53^{\mathrm{m}}50.18^{\mathrm{s}}$	$+54°04'40.9''$	0.099	5.231 ± 0.192	4.026 ± 0.081	1.27×10^{23}	7.29×10^{37}
ILTJ145415.10+492549.9	(J1454+49)	$14^{\mathrm{h}}54^{\mathrm{m}}15.10^{\mathrm{s}}$	$+49°25'49.9''$	0.037	6.264 ± 0.197	5.482 ± 0.119	2.00×10^{22}	5.39×10^{36}
ILTJ150422.16+474111.2	(J1504+47)	$15^{\mathrm{h}}04^{\mathrm{m}}22.16^{\mathrm{s}}$	$+47°41'11.2''$	0.093	20.11 ± 1.092	12.24 ± 0.723	4.29×10^{23}	1.25×10^{38}

Table 4.2: Details of the VLA data across the two observing epochs. Here Ant and Chan refer to the number of antennas and the number of channels used during the observations respectively.

Label	Project code	Date of observation	Start time	End time	Duration (s)	Ant	Chan	Bandwidth (GHz)	Array
Epoch 1	19A-264	15-Sep-2019	15:22:56.0	19:22:12.0	14356	27	64	4−8	A
Epoch 2	19A-264	24-Sep-2019	14:07:20.0	18:06:38.0	14358	27	64	4−8	A

Table 4.3: VLA calibrator sources.

Calibrator Name	Description
1331+305 = 3C286	flux calibrator
J1035+5628	phase calibrators
J1146+5356	
J1219+4829	
J1349+5341	
J1419+5423	
J1407+2827	polarization calibrator

4.3.1 Data reduction and calibration

I provide a summary of Chapter 3 in this section regarding the reduction and calibration of VLA observations with CASA (McMullin et al., 2007).

Before data calibration, I first inspected the VLA data using the visualising tool PLOTMS to determine the nature of the data. This was to ensure that all issues reported in the observer's log were taken into consideration. I then performed basic data editing by manually flagging the setup scan (the first scan) using the task FLAGDATA in MANUAL mode. In the final basic data edit, initial samples (QUACKINTERVAL, 10s) from the start of each scan were also manually flagged in QUACK mode to allow the array some settling time. After basic data inspection and editing based on a prior information, amplitude spikes caused by RFI dominating some spectral window IDs were removed by the HANNINGSMOOTH algorithm, which removes Gibbs ringing. RFI excision was thereafter followed up by running an automated task FLAGDATA in TFCROP mode.

Throughout the calibration process, I chose a convenient reference antenna (from the middle of the 'Y' shaped array) with good solutions. I then proceeded to calibrate the data by first correcting for antenna positions using the task GENCAL to correctly correlate each signal for a good estimation of the final image. A known flux density was then set for the primary calibrator 3C 286 by locating the VLA standard model at C-band 3C286_C.im using the task SETJY. This was applied using the PERLEY-BUTLER 2017 flux density standard model (Perley and Butler, 2017). Phase and delay-only calibration solutions were then derived using the task GAINCAL by choosing a short solution interval. For a reasonable SNR, only a portion of the middle channels was selected for the phase-only calibration while also flagging unstable antennas (i.e. antennas with phase jumps between two or more states). Once variations in phase as a function of time were corrected, antenna-based delays were also corrected. Bandpass solutions were derived using the task BANDPASS which measures and corrects for the equipment response of the receiver. The last rounds of data calibration were to determine appropriate solutions for the targets by first deriving complex gains for the amplitude calibrator and later deriving solutions for phase calibrators using the task GAINCAL. In the final step, I derived solutions of true flux densities of secondary calibrators with the

Table 4.4: Imaging summary. I adjusted the image size to account for surrounding sources to mitigate artefacts in the final images during self-calibration.

CASA parameter	Value	Unit
imsize	3200×3200	pixels
cell	0.08×0.08	arcsec
gridder	standard	
deconvolver	clark	
weighting	briggs	
robust	0.5	
niter	1000	
threshold	0.03	mJy

task FLUXSCALE to produce a properly-scaled amplitude gain calibration table for secondary calibrators. Since we determined the flux density of the primary (amplitude) calibrator, I used this solution as our reference to compute the true flux densities of the secondary (phase and polarization) calibrators.

Finally, after deriving all calibration solutions, I applied these solutions using the task APPLYCAL to first the calibrator sources themselves (by nearest interpolation), then to the target sources (by linear interpolation). At this stage, any traces of bad data were flagged using the task FLAGDATA in RFLAG mode. This mode only works on calibrated data as it utilises the CORRECTED_DATA column. I split the science targets from the measurement set's (MS) CORRECTED_DATA column using the task SPLIT in readiness for imaging. I also utilised this task to average the data in time and channel (by a factor of 4s and 4 channels respectively) to save deconvolution time. To correct for the effects of relative scatter arising from flagging, I used the task STATWT which also calculates and sets weightings of visibilities if they are to be combined into a single MS. The targets from epochs 1 and 2 were combined with the task CONCAT. I produced initial images with the TCLEAN algorithm using the CLARK deconvolver (Clark, 1980). I also used a BRIGGS weighting with a ROBUST parameter value of 0.5 (Briggs, 1995). Three or four self-calibration rounds in phase only were performed for targets with a peak flux density value greater than 2 mJy. In some special cases, however, a final round in phase and amplitude was performed for targets with peak flux densities greater than 6 mJy using a solution interval between $30-60$s and a 3σ threshold; though in some cases, self-calibration barely improved the quality of the final image. The imaging parameters discussed above are summarised in Table 4.4 while the rest of the imaging parameters were left on default settings.

4.4 Analysis and Results

4.4.1 Radio emission categories

To analyse the nature of the images produced, source parameters in the final images were computed using the task IMFIT. This tool fits two-dimensional Gaussian elliptical components on a region in the image. This was achieved by interactively drawing boxes or tracing polygons around the edge of the object's emission. The final output returned the integrated flux, peak flux, convolved and deconvolved

source parameters that is the angular major and minor axes (in arcsec) at FWHM, and the position angles (PA; degrees). This information is listed in Tables 4.6 and 4.7 together with the errors associated with them (given by estimates in the IMFIT model fitting and taking into consideration the 5% limit in the flux calibration; Perley and Butler, 2017). I also estimated the images' root mean square ($\sigma_{\rm rms}$) values by selecting a region free of emission yet close enough to the source. This gave a range of $\sigma_{\rm rms}$ values spanning $\sim$12$-$45 μJy with higher values corresponding to brighter sources (i.e. sources with integrated fluxes greater than 20 mJy). The spectral indices listed in Tables 4.6 and 4.7 are computed between LOFAR and the VLA observing frequencies (150 MHz and 6 GHz respectively) and using the power law definition given in Chapter 1. Using the VLA final images (visual inspection for extended emission) and the information derived from IMFIT, I constructed three categories of these objects: undetected, compact, and extended. Further analyses and discussions of their morphologies and scales are presented in Sec 4.4.2, 4.4.3, and 4.4.4. A summary of this category is also shown below (Table 4.5).

Table 4.5: Final image category.

Total RLAGN objects	Undetected objects	Unresolved objects	Resolved objects
55	3	43	9

4.4.2 Undetected radio emission

A visual inspection of the VLA images shows no detection (see Fig. 4.4) of radio emission in three ($3/55$; $\sim$5%) objects namely; J1159+55, J1203+51, and J1304+49. These objects by visual inspection, however, clearly show compact radio emission in LoTSS DR2 images. A discussion of their radio spectra is given in Sec. 4.5.1 estimated by setting an upper limit (3σ; respectively, σ=13.68μJy, 14.10μJy, and 14.02μJy) on the total flux for each restoring image; for this case, a non-detection in all three cases imply a steep radio spectrum (see Fig. 4.7).

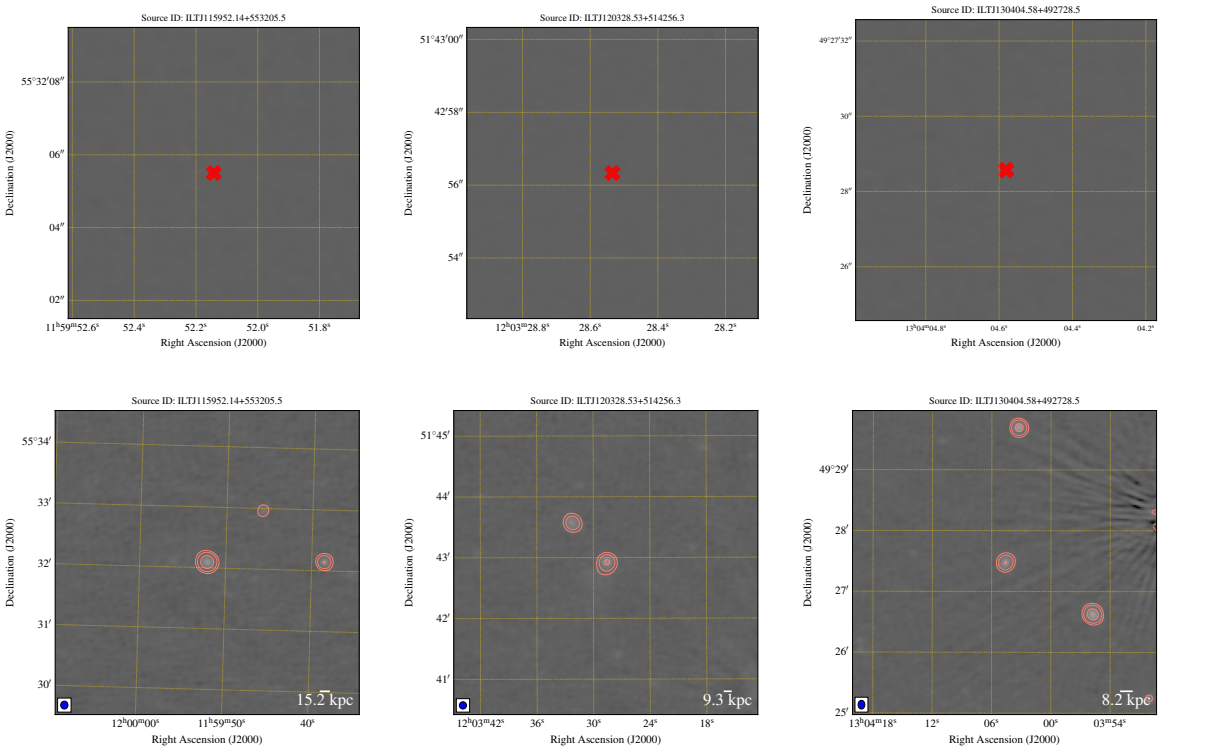

Figure 4.4: Top three panels are VLA images for non-detected objects at 6 GHz; red crosses indicate the central position where radio emission is detected in LoTSS DR2 images (bottom panels). The physical sizes (in kpc) shown in LoTSS DR2 images are upper limits, estimated from twice the deconvolved size plus three times the associated error. LoTSS DR2 images and contour maps are at levels [-3, 3, 5, 10, 20,...,640] $\times$ $\sigma_{\rm rms}$ where $\sigma_{\rm rms} = 71,\ 120,$ and 125 μJy (from left to right) respectively.

4.4.3 Compact radio emission and radio maps

To correctly classify unresolved sources, I compared the image component sizes (deconvolved from the beam) against their restoring beam parameters provided by IMFIT. I also took into account the comparisons of the object's total and peak flux densities (see Table 4.6). Sources with a deconvolved size less than the restoring beam and with peak and integrated flux densities within a factor of 1.2 or less were classified as compact. Using these criteria, 43 out of 55 objects (representing $\sim$78% of the sources in our catalogue) are compact in the VLA images (see Fig. 4.5). This implies that these objects are compact compared to the limiting angular resolution of the VLA of 0.35 arcsec, corresponding to $\sim 0.1-0.8$ kpc in projected physical sizes. Given that these sources were selected on the basis of their compact nature in LoTSS DR1, 3 of the VLA compact objects (J1151+53, J1433+52, and J1504+47) show extended radio emission in LoTSS DR2 images (see Chapter 5, Fig. 5.1). These appear to be in fact the radio cores of more extended sources with projected sizes spanning $\sim 10-49$ kpc, which were not identified as such in LoTSS DR1 because of its poorer surface brightness sensitivity. A brief description of their structures is given in Sec. 5.1. Another source that is compact here, J1213+50 (NGC 4187), shows extended radio emission in the VLA images at 1.5, 4.5, and 7.5 GHz observing frequencies (e.g. Baldi et al., 2019). The object shows a two-jetted radio morphology that extends up to $\sim$2 kpc in projected physical size. A detailed discussion of the spectral index distribution for the whole sample is given in Sec. 4.5.

Table 4.6: Forty-three VLA compact objects. The spectral indices (α) and luminosities ($L_{6\ \mathrm{GHz}}$) are computed using the information presented in Table 4.1. The restoring and deconvolved source parameters determined at FWHM are also presented. The sizes (kpc) of the objects are estimated from twice the size of the deconvolved beam's major axis.

LOFAR source name	Total flux 6 GHz (S_{Int}, mJy)	Peak flux 6 GHz (S_{p}, mJy)	Restoring beam $[\theta_{\mathrm{M}}^{\mathrm{R}} \times \theta_{\mathrm{m}}^{\mathrm{R}}]$ (arcsec)	PA$^{\mathrm{R}}$ (°)	Deconvolved size $[\theta_{\mathrm{M}}^{\mathrm{D}} \times \theta_{\mathrm{m}}^{\mathrm{D}}]$ (arcsec)	Spectral index (α_{150}^{6000})	Size (arcsec)	Linear size (D, kpc)	Luminosity $L_{6\ \mathrm{GHz}}$ (W Hz^{-1})	RMS σ_{rms} (μJy)
ILTJ105535.82+462903.3	2.18 ± 0.04	2.11 ± 0.02	0.35 × 0.31	79.11	0.05 × 0.02	-0.15	0.10	0.17	4.03×10^{22}	14.13
ILTJ110233.62+513124.3	2.65 ± 0.06	2.46 ± 0.03	0.35 × 0.30	72.09	0.13 × 0.04	-0.24	0.26	0.34	2.88×10^{22}	13.67
ILTJ111745.92+473327.5	6.62 ± 0.04	6.35 ± 0.02	0.35 × 0.32	62.05	0.09 × 0.05	-0.38	0.18	0.25	8.67×10^{22}	19.01
ILTJ113545.33+491619.6	2.96 ± 0.05	2.75 ± 0.03	0.43 × 0.36	81.82	0.12 × 0.10	-0.13	0.24	0.24	1.87×10^{22}	13.63
ILTJ113757.19+554207.5	2.67 ± 0.05	2.56 ± 0.03	0.34 × 0.30	60.47	0.09 × 0.17	-0.08	0.18	0.22	2.35×10^{22}	13.49
ILTJ114047.35+463225.5	30.8 ± 0.13	30.1 ± 0.07	0.32 × 0.29	38.92	0.05 × 0.04	0.36	0.10	0.10	1.96×10^{23}	20.00
ILTJ114316.26+551639.9	22.6 ± 0.10	21.8 ± 0.06	0.33 × 0.29	58.97	0.07 × 0.06	-0.03	0.14	0.14	1.54×10^{23}	13.86
ILTJ114721.40+554348.4	3.50 ± 0.04	3.42 ± 0.02	0.35 × 0.31	66.94	0.07 × 0.02	0.02	0.14	0.13	2.09×10^{22}	14.78
ILTJ115113.46+550659.0	0.38 ± 0.02	0.37 ± 0.01	0.35 × 0.31	71.47	0.08 × 0.03	-0.82	0.16	0.22	5.82×10^{21}	13.88
ILTJ115157.87+532845.5	3.23 ± 0.03	3.07 ± 0.02	0.38 × 0.30	75.81	0.11 × 0.04	-0.05	0.22	0.25	2.59×10^{22}	16.96
ILTJ115205.79+545817.1	5.30 ± 0.03	5.16 ± 0.02	0.36 × 0.32	73.54	0.07 × 0.04	-0.20	0.14	0.16	4.37×10^{22}	12.54
ILTJ115330.55+524121.8	16.0 ± 0.05	15.6 ± 0.03	0.44× 0.36	84.37	0.07 × 0.06	-0.20	0.14	0.20	1.89×10^{23}	20.60
ILTJ115438.10+491851.4	7.00 ± 0.07	6.88 ± 0.04	0.34 × 0.32	61.58	0.05 × 0.03	0.10	0.10	0.11	4.56×10^{22}	13.62
ILTJ115531.40+545200.4	29.5 ± 0.19	29.0 ± 0.10	0.37 × 0.31	68.89	0.07 × 0.02	0.22	0.14	0.13	1.62×10^{23}	39.32
ILTJ120801.00+523635.3	0.41 ± 0.04	0.26 ± 0.02	0.40 × 0.30	83.84	–	-0.53	–	–	6.45×10^{21}	14.58
ILTJ121329.29+504429.4	74.6 ± 0.47	69.6 ± 0.26	0.33 × 0.30	63.97	0.10 × 0.08	-0.25	0.20	0.12	1.59×10^{23}	45.01
ILTJ123011.86+470022.7	68.4 ± 0.20	64.9 ± 0.11	0.35 × 0.30	73.10	0.09 × 0.06	-0.11	0.18	0.13	2.35×10^{23}	33.30
ILTJ123301.22+561013.7	1.68 ± 0.10	1.56 ± 0.05	0.39 × 0.29	79.31	0.12 × 0.05	-0.14	0.24	0.37	2.56×10^{22}	14.52
ILTJ124021.48+475143.6	2.34 ± 0.08	1.97 ± 0.04	0.37 × 0.32	78.07	0.15 × 0.15	-0.40	0.30	0.55	5.36×10^{22}	13.52
ILTJ125827.27+501650.6	0.32 ± 0.03	0.26 ± 0.02	0.39 × 0.31	84.32	0.15 × 0.09	-0.58	0.30	0.53	7.71×10^{21}	13.82
ILTJ130325.87+523522.5	7.44 ± 0.04	7.25 ± 0.02	0.40 × 0.34	80.26	0.09 × 0.03	-0.07	0.18	0.29	1.57×10^{23}	16.96
ILTJ130535.92+540142.5	17.1 ± 0.06	16.7 ± 0.03	0.39 × 0.32	78.24	0.07 × 0.05	-0.09	0.14	0.21	3.24×10^{23}	19.38
ILTJ131002.06+540005.2	1.85 ± 0.07	1.75 ± 0.04	0.39 × 0.30	77.75	0.09 × 0.02	-0.10	0.18	0.30	3.38×10^{22}	15.13
ILTJ132745.67+544756.8	2.32 ± 0.12	1.88 ± 0.06	0.36 × 0.32	69.55	0.18 × 0.15	-0.41	0.36	0.24	5.72×10^{21}	14.43
ILTJ133430.04+502718.3	0.80 ± 0.02	0.75 ± 0.01	0.39 × 0.31	-89.98	0.12 × 0.07	-0.36	0.24	0.36	1.36×10^{22}	13.50
ILTJ134227.94+554939.3	0.46 ± 0.02	0.34 ± 0.10	0.36 × 0.31	74.91	0.24 × 0.13	-0.64	0.48	0.65	5.65×10^{21}	13.61
ILTJ134233.86+485316.2	1.75 ± 0.07	1.51 ± 0.04	0.39 × 0.31	-87.17	0.22 × 0.06	-0.39	0.44	0.73	3.44×10^{22}	15.44
ILTJ134345.04+553801.3	0.41 ± 0.02	0.28 ± 0.01	0.36 × 0.31	73.30	0.29 × 0.13	-0.54	0.58	0.76	4.46×10^{21}	12.28
ILTJ135632.65+493710.9	6.61 ± 0.03	6.45 ± 0.02	0.41 × 0.33	-85.97	0.08 × 0.04	0.14	0.16	0.19	6.45×10^{22}	15.41
ILTJ140013.20+462556.0	0.69 ± 0.04	0.63 ± 0.02	0.41 × 0.31	-80.98	0.13 × 0.09	-0.46	0.26	0.26	4.50×10^{21}	14.19
ILTJ140906.86+532749.1	1.98 ± 0.07	1.72 ± 0.04	0.38 × 0.30	78.84	0.18 × 0.09	-0.65	0.36	0.53	2.89×10^{22}	13.08
ILTJ141149.57+545733.1	9.78 ± 0.05	9.52 ± 0.03	0.36 × 0.32	63.21	0.07 × 0.05	0.23	0.14	0.21	1.53×10^{23}	14.02
ILTJ141234.88+494611.5	3.08 ± 0.11	2.92 ± 0.06	0.37 × 0.31	84.95	0.09 × 0.08	-0.09	0.18	0.24	3.54×10^{22}	13.36
ILTJ141422.37+553520.5	0.24 ± 0.02	0.23 ± 0.01	0.35 × 0.30	61.01	0.09 × 0.03	-0.65	0.18	0.26	3.42×10^{21}	13.71
ILTJ142025.23+544016.1	1.87 ± 0.05	1.74 ± 0.03	0.37 × 0.30	69.16	0.09 × 0.03	-0.12	0.18	0.14	7.32×10^{21}	12.97
ILTJ142125.51+482933.3	23.0 ± 0.06	22.3 ± 0.03	0.38 × 0.30	-89.78	0.08 × 0.05	0.27	0.16	0.21	2.64×10^{23}	16.65
ILTJ142707.30+525001.5	3.41 ± 0.03	3.25 ± 0.02	0.37 × 0.31	80.76	0.10 × 0.05	-0.24	0.20	0.31	5.52×10^{22}	13.57
ILTJ142948.48+535754.2	1.65 ± 0.12	1.58 ± 0.07	0.36 × 0.29	74.21	0.09 × 0.01	-0.21	0.18	0.15	6.95×10^{21}	15.29
ILTJ143334.77+524310.2	1.95 ± 0.04	1.82 ± 0.02	0.38 × 0.31	83.02	0.14 × 0.05	-0.18	0.28	0.24	8.98×10^{21}	13.91
ILTJ143521.75+505123.0	66.5 ± 0.60	54.2 ± 0.30	0.39 × 0.31	86.18	0.23 × 0.10	-0.44	0.46	0.80	1.59×10^{24}	32.44
ILTJ145350.18+540440.9	5.92 ± 0.04	5.91 ± 0.02	0.37 × 0.28	86.89	0.02 × 0.02	0.04	0.03	0.10	1.34×10^{23}	13.41
ILTJ145415.10+492549.9	7.46 ± 0.14	7.35 ± 0.08	0.42 × 0.34	-64.04	0.06 × 0.04	0.05	0.12	0.10	2.31×10^{22}	26.14
ILTJ150422.16+474111.2	2.20 ± 0.11	2.13 ± 0.06	0.42 × 0.30	-84.08	0.08 × 0.05	-0.59	0.15	0.26	4.65×10^{22}	14.26

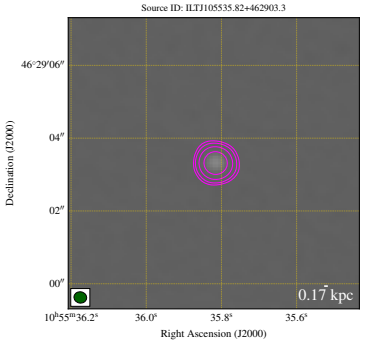
Source ID: ILTJ105535.82+462903.3
Declination (J2000)
Right Ascension (J2000)
0.17 kpc

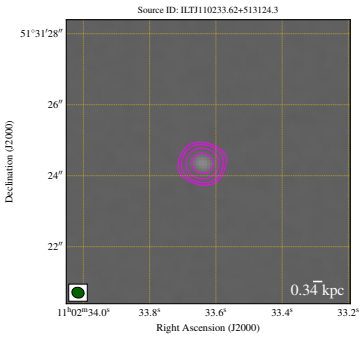
Source ID: ILTJ110233.62+513124.3
Declination (J2000)
Right Ascension (J2000)
0.34 kpc

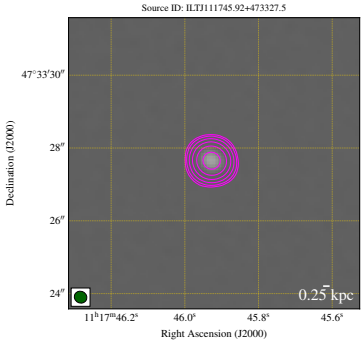
Source ID: ILTJ111745.92+473327.5
Declination (J2000)
Right Ascension (J2000)
0.25 kpc

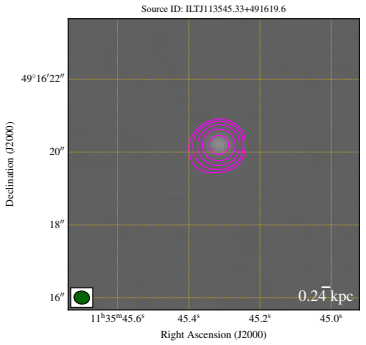
Source ID: ILTJ113545.33+491619.6
Declination (J2000)
Right Ascension (J2000)
0.24 kpc

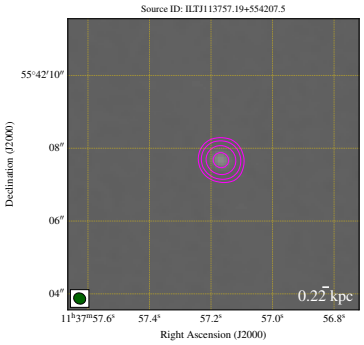
Source ID: ILTJ113757.19+554207.5
Declination (J2000)
Right Ascension (J2000)
0.22 kpc

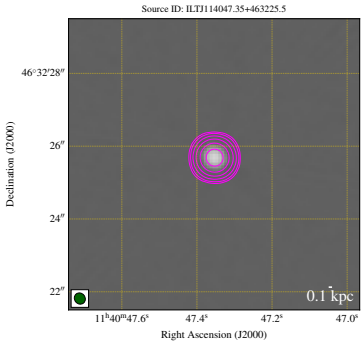
Source ID: ILTJ114047.35+463225.5
Declination (J2000)
Right Ascension (J2000)
0.1 kpc

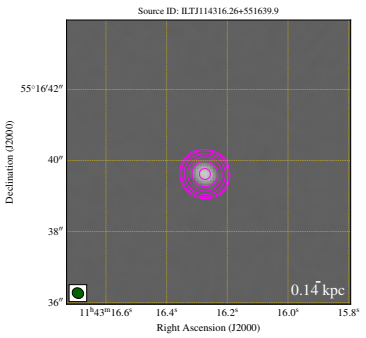
Source ID: ILTJ114316.26+551639.9
Declination (J2000)
Right Ascension (J2000)
0.14 kpc

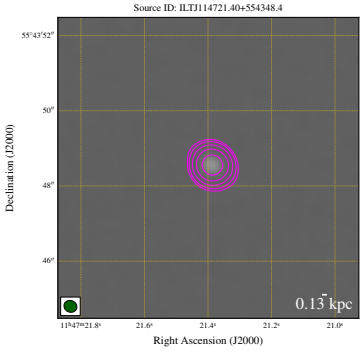
Source ID: ILTJ114721.40+554348.4
Declination (J2000)
Right Ascension (J2000)
0.13 kpc

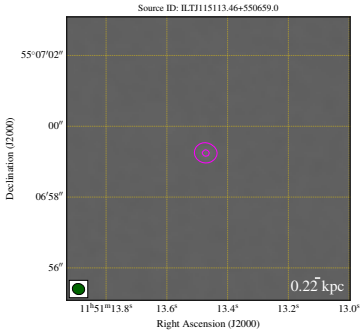
Source ID: ILTJ115113.46+550659.0
Declination (J2000)
Right Ascension (J2000)
0.22 kpc

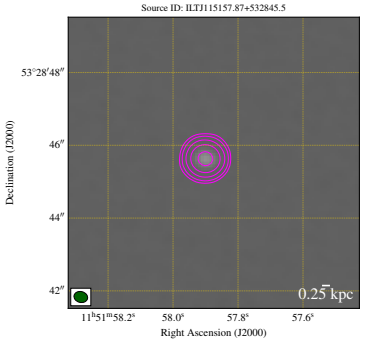
Source ID: ILTJ115157.87+532845.5
Declination (J2000)
Right Ascension (J2000)
0.25 kpc

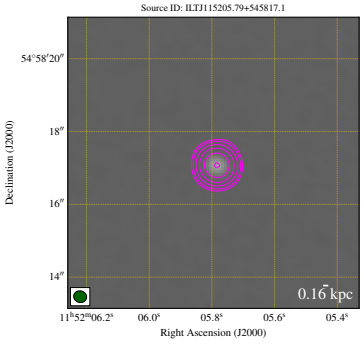
Source ID: ILTJ115205.79+545817.1
Declination (J2000)
Right Ascension (J2000)
0.16 kpc

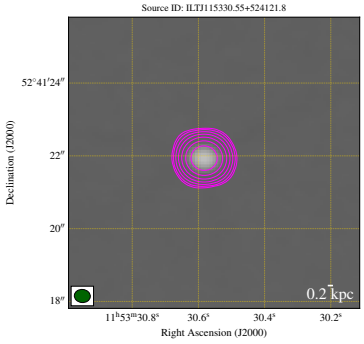
Source ID: ILTJ115330.55+524121.8
Declination (J2000)
Right Ascension (J2000)
0.2 kpc

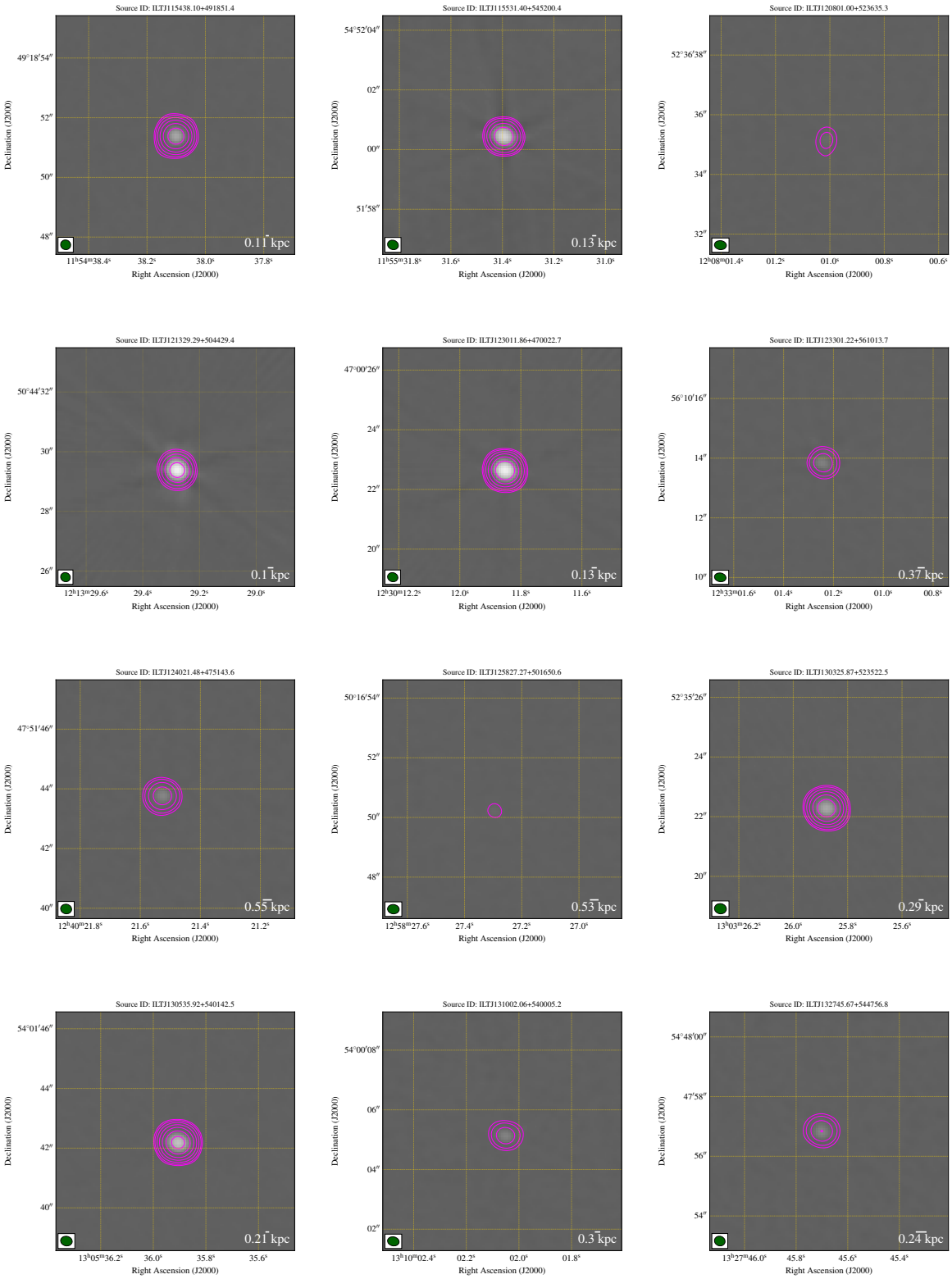
Source ID: ILTJ115438.10+491851.4
Source ID: ILTJ115531.40+545200.4
Source ID: ILTJ120801.00+523635.3
Source ID: ILTJ121329.29+504429.4
Source ID: ILTJ123011.86+470022.7
Source ID: ILTJ123301.22+561013.7
Source ID: ILTJ124021.48+475143.6
Source ID: ILTJ125827.27+501650.6
Source ID: ILTJ130325.87+523522.5
Source ID: ILTJ130535.92+540142.5
Source ID: ILTJ131002.06+540005.2
Source ID: ILTJ132745.67+544756.8
Declination (J2000)
Right Ascension (J2000)
0.11 kpc
0.13 kpc
0.13 kpc
0.1 kpc
0.13 kpc
0.37 kpc
0.55 kpc
0.53 kpc
0.29 kpc
0.21 kpc
0.3 kpc
0.24 kpc

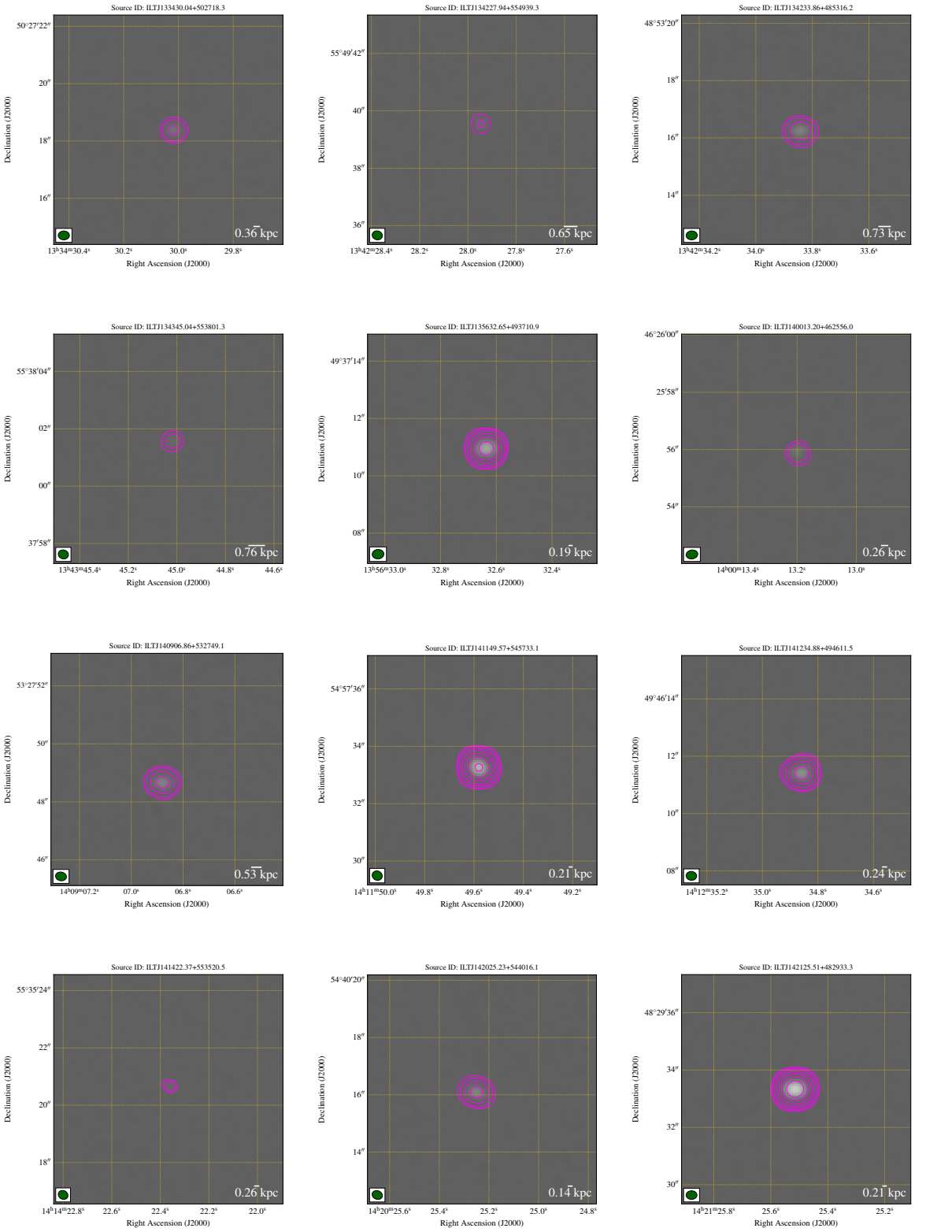
Source ID: ILTJ133430.04+502718.3
0.36 kpc
Source ID: ILTJ134227.94+554939.3
0.65 kpc
Source ID: ILTJ134233.86+485316.2
0.73 kpc
Source ID: ILTJ134345.04+553801.3
0.76 kpc
Source ID: ILTJ135632.65+493710.9
0.19 kpc
Source ID: ILTJ140013.20+462556.0
0.26 kpc
Source ID: ILTJ140906.86+532749.1
0.53 kpc
Source ID: ILTJ141149.57+545733.1
0.21 kpc
Source ID: ILTJ141234.88+494611.5
0.24 kpc
Source ID: ILTJ141422.37+553520.5
0.26 kpc
Source ID: ILTJ142025.23+544016.1
0.14 kpc
Source ID: ILTJ142125.51+482933.3
0.21 kpc
Declination (J2000)
Right Ascension (J2000)

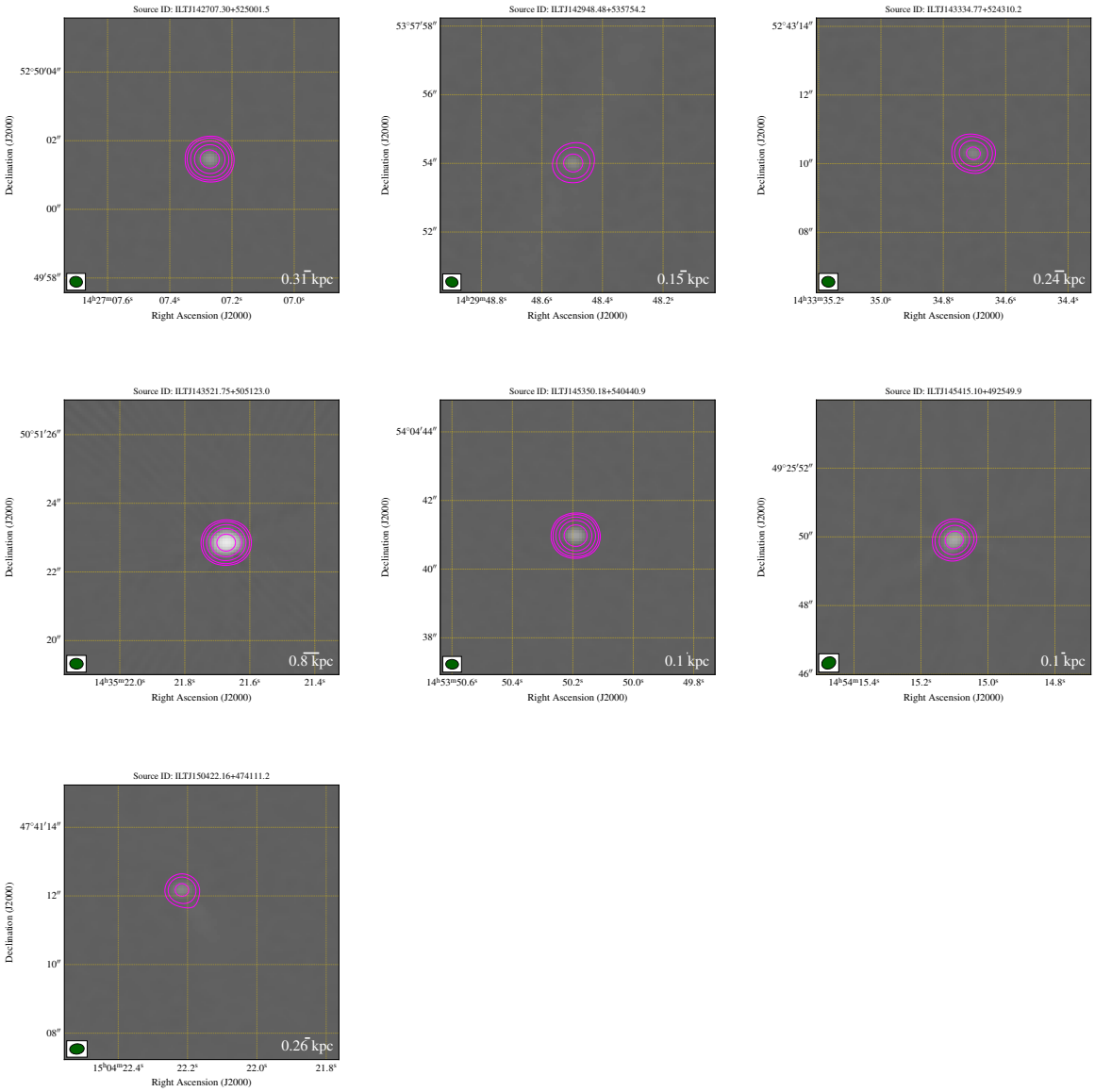

Figure 4.5: VLA images for compact RLAGN overlaid with VLA 6 GHz contour maps (magenta) at levels [-3, 3, 5, 10, 20,...,640]$\times$ $\sigma_{\rm rms}$ where $\sigma_{\rm rms}$ is presented in Table 4.6 for each object. The RA and DEC covered by each object are shown on the axes. The VLA beam is shown in the bottom left corner (green ellipses). Shown also are physical sizes (in kpc) estimated from twice the deconvolved size. The scale bar is in arcsec.

4.4.4 Extended radio emission and radio maps

The remaining nine ($9/55$; $\sim$16%) objects show extended radio emission and are resolved or at least marginally resolved in the VLA images. Their information is presented in Table 4.7 and the VLA images overlaid with contour maps for each of these sources are shown in Fig. 4.6. A brief description of their radio morphologies and their scales follows here; I discuss their extended radio emission with respect to high-quality LoTSS DR2 images of these objects.

Table 4.7: Nine VLA extended objects. The sizes (arcsec) of the extended radio emission are estimated at the 3σ contour boundary. The linear sizes (kpc) are computed using the redshift information presented in Table 4.1. RMS values were estimated from a region free from emission and closer to the source in the 6 GHz VLA images.

LOFAR Source name	Total flux 6 GHz ($S_{\rm int}$, mJy)	Peak flux 6 GHz ($S_{\rm p}$, mJy)	Restoring beam $[\theta^{\rm R}_{\rm M} \times \theta^{\rm R}_{\rm m}]$ (arcsec)	PA$^{\rm R}$ (°)	Spectral index (α^{6000}_{150})	Size (arcsec)	Linear size (kpc)	Luminosity $L_{6\ \rm GHz}$ (W Hz^{-1})	RMS $\sigma_{\rm rms}$ (μJy)
ILTJ104852.93+480314.8	6.37 ± 0.26	3.28 ± 0.09	0.34×0.31	72.96	-0.63	2.50	2.02	2.46×10^{22}	15.3
ILTJ111156.65+555449.9	0.54 ± 0.04	0.15 ± 0.01	0.36×0.30	66.55	-0.62	1.86	2.51	6.44×10^{21}	15.2
ILTJ111712.10+465135.6	2.65 ± 0.35	1.08 ± 0.10	0.34×0.30	79.67	-0.42	1.04	1.22	2.27×10^{22}	30.4
ILTJ112625.15+520503.6	3.46 ± 0.25	2.63 ± 0.12	0.37×0.32	70.62	-0.53	1.85	1.75	1.85×10^{22}	25.8
ILTJ124343.52+544902.0	1.93 ± 0.18	1.70 ± 0.09	0.38×0.31	77.11	-0.34	1.41	2.25	3.25×10^{22}	23.2
ILTJ130410.78+552839.0	0.60 ± 0.06	0.33 ± 0.02	0.36×0.32	52.70	-0.50	1.20	1.85	9.50×10^{21}	19.9
ILTJ131015.19+544004.8	2.12 ± 0.28	0.70 ± 0.07	0.35×0.33	54.74	-0.26	1.99	2.44	1.99×10^{22}	25.3
ILTJ141118.46+551053.2	4.91 ± 0.42	3.93 ± 0.21	0.35×0.31	49.27	-0.46	2.63	2.18	1.98×10^{22}	18.1
ILTJ142255.56+474713.9	0.44 ± 0.05	0.21 ± 0.02	0.39×0.30	-88.02	-0.55	1.81	2.48	5.36×10^{21}	18.1

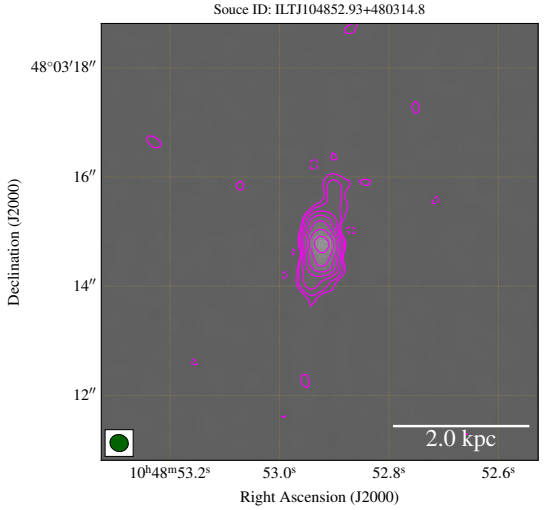

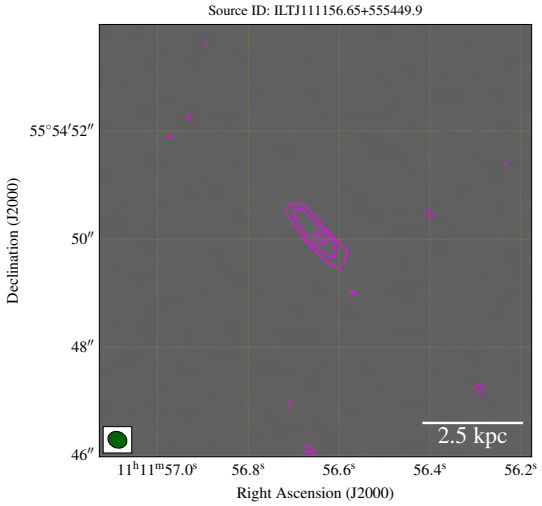

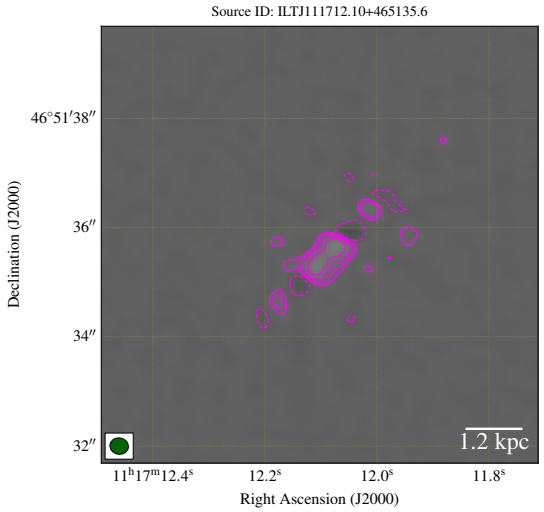

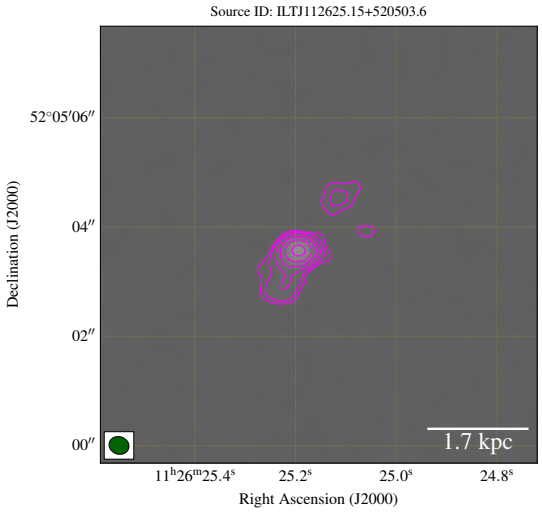

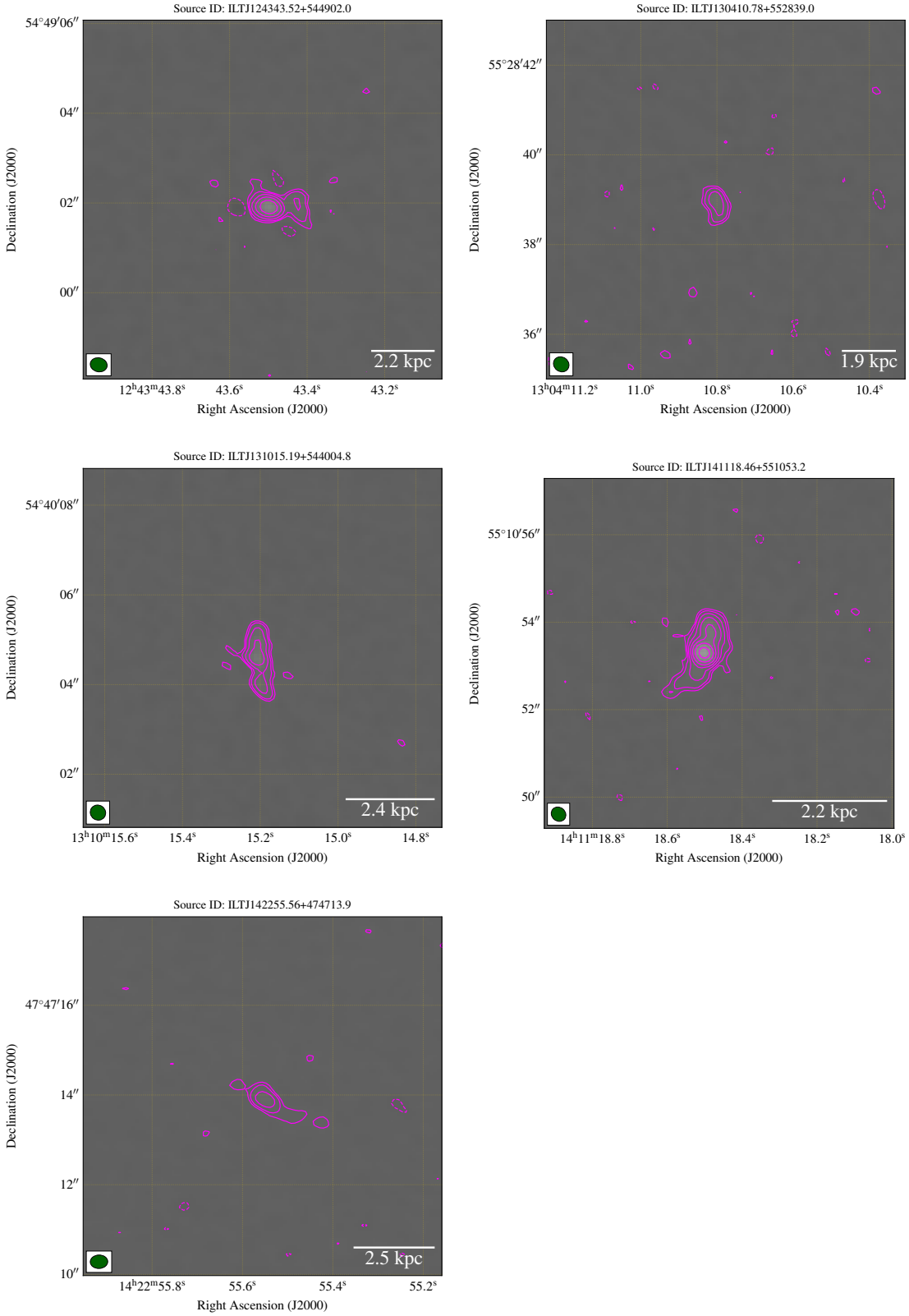

Figure 4.6: VLA images overlaid with VLA 6 GHz contour maps (magenta) at levels [-3, 3, 5, 10, 20, 40,...,640]$\times$ $\sigma_{\rm rms}$ where $\sigma_{\rm rms}$ is presented in Table 4.7 for each object. The RA and DEC covered by each object are shown on the axes. Solid lines represent positive contours (3σ), whereas dashed lines correspond to negative contours (-3σ). Shown in the bottom left corner (green ellipses) for each object is the VLA beam while the physical sizes (in kpc) are shown in the bottom right corner; the scale bar is in arcsec. North is up and east is left.

4.4.4.1 ILTJ104852.93+480314.8

The VLA contours for this source show a bright unresolved or slightly resolved radio core with two-sided jets symmetrically extending away from the central structure. The total maximum length of the extended emission is projected to be approximately 2.0 kpc. This object is compact in LoTSS DR2 images.

4.4.4.2 ILTJ111156.65+555449.9

The VLA radio contours for this object show double-sided jets with a maximum length of $\sim$2.5 kpc. The emission seems to propagate from its centre to the north-east direction and we see no sign of a bright compact core. However, the object clearly shows extended radio emission in LoTSS DR2 images extending in the same direction as in the VLA image. In DR2, the object shows an unresolved/slightly resolved bright central radio structure whose maximum projected physical extent is measured at $\sim$22 kpc (see Fig. 5.1). The object appears to be the radio core of a more extended and powerful FRI/II source with faint double symmetric jets/plumes faintly seen propagating away from the bright central radio core. However, the 3σ radio contours overlaid on the LoTSS DR2 image (Fig. 5.1) do not fully capture this radio emission.

4.4.4.3 ILTJ111712.10+465135.6

This object shows a double-lobed radio structure with two bright edges, a radio morphology similar to that of FRIIs but on much smaller scales. More observations are required to confirm if the two 'blobs' seen on either side away from the central structure could be due to a jet or artefact. The maximum projected length for this source is measured at $\sim$1.2 kpc. The source lacks any extended radio emission in LoTSS DR2 images and is compact.

4.4.4.4 ILTJ112625.15+520503.6

The contours for this object show a bright unresolved/slightly resolved radio core with a one-sided jet radio morphology. Its structure extends south-east from the centre. The blob seen in the north-west direction away from the central structure could be due to a jet or artefact. The maximum projected length of the central structure is $\sim$1.7 kpc. This object is also compact in LoTSS DR2 images.

4.4.4.5 ILTJ124343.52+544902.0

Contour maps for this object show a bright unresolved or slightly resolved one-sided jet extending to the west. The maximum projected length is $\sim$2.2 kpc in physical size. The object is compact in LoTSS DR2.

4.4.4.6 ILTJ130410.78+552839.0

The VLA contour maps for this object show a slightly extended complex radio structure projected at ∼1.9 kpc in physical size. The object does not show the bright central core that is seen in most of these extended images. The object is compact in LoTSS DR2 images.

4.4.4.7 ILTJ131015.19+544004.8

Radio contour maps for this object show a slightly resolved radio core and double symmetrical radio structures/lobes on either side of the radio core. The radio morphological classification of this object is similar to those of FRIs but on smaller scales. The maximum length of the radio emission is projected at ∼2.4 kpc. LoTSS DR2 contour maps for this object show faint and diffuse extended emission (Fig. 5.1) propagating symmetrically north and south from the bright unresolved central structure. Given that a similar morphology is seen in the VLA images but on smaller scales does suggest that the emission is in fact associated with jets rather than artefacts. The maximum length of the central structure in LoTSS DR2 is projected at ∼19 kpc

4.4.4.8 ILTJ141118.46+551053.2

Contour maps for this object show a bright radio core and two-sided radio structures extending in the north and south-east directions. The maximum projected length is ∼2.2 kpc. The object is compact in DR2 images.

4.4.4.9 ILTJ142255.56+474713.9

The VLA radio contours for this object show a slightly resolved structure extending in the north-east direction with a slight tail extending in the south-west direction. The two-sided morphology is projected at ∼2.5 kpc in physical scale. The object is compact in LoTSS DR2 images.

4.5 Discussion

I give a discussion of the 55 low-radio power sources in this section and it proceeds as follows: the distribution of spectral indices is discussed in Sec. 4.5.1, whereas I investigate the effects of synchrotron self-absorption (SSA) in Sec. 4.5.2. The position of the objects on the power/linear size ($P-D$) diagram is discussed in Sec. 4.5.3. I end this section with a discussion of our sources with similarly compact RLAGN such as 'FR0s' (Section 4.5.4).

4.5.1 Radio spectral index

Extragalactic sources dominate the radio sky (e.g. Condon, 1999) and to understand the nature of low-luminosity compact RLAGN, we have to study their physical properties in the radio range. The spectral index of radio sources provides valuable information that can be used to estimate the age of electrons responsible for the radio emission, and in constraining the duty cycle of AGN activity (Kellermann, 1964; Pacholczyk, 1970). This information can be used to further understand emission and absorption processes, and energy losses for radio sources. Typical values of the observed spectral index for extended RLAGN lie between $-1 < \alpha < -0.5$, following the definition in Sec. 1.2. At low frequencies (e.g. 150 MHz), SFGs dominate over RLAGN (particularly at luminosities below $L_{150\ \mathrm{MHz}} < 10^{25}$ W Hz^{-1} and $z < 0.3$, e.g. Padovani, 2016; Hardcastle et al., 2016; Gürkan et al., 2018; Hardcastle et al., 2019), and a clear understanding of the spectra of these radio sources are important in determining the radio emission resulting from low-luminosity SF or low-luminosity RLAGN (e.g. Prandoni et al., 2006; Ibar et al., 2009). This emission mechanism was used by, for example, Huynh et al. (2007) in classifying AGNs from SFGs by proposing that AGNs produce flat and/or inverted spectra at low frequencies due to self-absorption in a medium that is optically thick, a condition that is not met in SFGs; however, Zinn et al. (2012) note that this mechanism is not ideal for AGN-SF separation techniques unless other reliable diagnostic means are not present. The radio spectrum is also important in classifying RLAGN to investigate if they are CSOs (e.g. Wilkinson et al., 1994), GPSs (very steep spectral indices, i.e. $\alpha \lesssim -0.8$ at high frequencies and a very inverted $\alpha \gtrsim +0.8$ spectrum at low frequencies) or CSSs ($\alpha \lesssim -0.5$ at high frequencies) (e.g. O'Dea et al., 1990; Fanti et al., 1990; O'Dea et al., 1991; O'Dea, 1998). The radio spectrum can also help us understand the $z - \alpha$ relation; this is used to track radio objects at high redshifts (e.g. Klamer et al., 2006; Morabito and Harwood, 2018) which suggests that radio objects at higher redshifts exhibit very steep spectral indices ($\alpha < -1.0$).

It has been observed that compact RLAGN and their hotspots show flatter spectral indices than larger and extended objects (e.g. de Gasperin et al., 2018). And at low frequencies, flat radio spectra, core-dominated objects become numerically dominant, an effect that is usually attributed to SSA and FFA (e.g. Bicknell et al., 2018; O'Dea and Saikia, 2021), whereas the steep radio spectra observed for extended objects is usually associated with old plasma (e.g. Bicknell et al., 2018).

One method of creating a catalogue of spectral indices is by cross-matching two or more source catalogues from different radio surveys at different frequencies (e.g Vollmer et al., 2005; Randall et al., 2012). In this work however, I have derived spectral indices using the definition in Sec. 1.2 taking logarithmic ratios of the fluxes and frequencies between LOFAR and the VLA.

Fig. 4.7 shows the spectral index distribution of our objects ranging from steep to flat and/or inverted radio spectra ($-1.31 < \alpha < 0.36$); this implies that our RLAGN sample consists of various compact RLAGN. Approximately 29% (16 out of 55) of these objects show steep spectral indices (i.e. $-1.31 < \alpha < -0.50$)[10] which is consistent with standard models for optically thin synchrotron radio emission –

[10]These include the radio spectra for the 3 undetected objects: J1159+55, J1203+51, and J1304+49 showing at the steeper

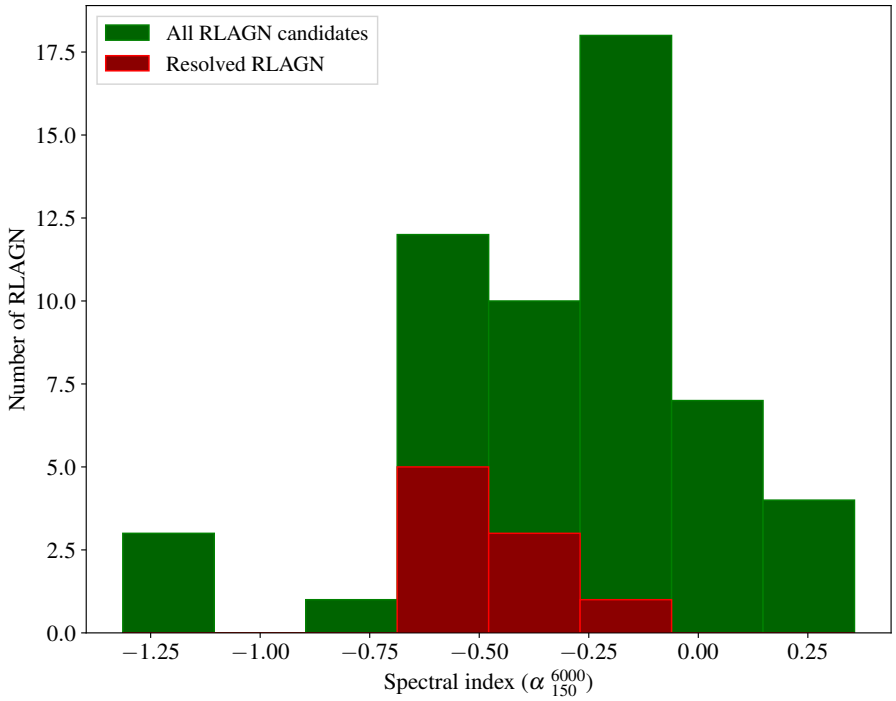

Figure 4.7: A histogram distribution of spectral indices computed between LOFAR and the VLA at 150 MHz and 6 GHz respectively. Showing in red is the distribution of objects with extended emission while the green distribution is for the whole sample. Values for which $\alpha_{150}^{6000} \approx -1.30,\ -1.27,$ and $-\ 1.31$ are upper limits for sources not detected by the VLA (Sec. 4.4.2).

9 of these objects are compact at the limiting angular resolution of 0.35 arcsec while 5 show extended radio structures. The remaining objects (4 extended and 35 compact) show flat ($\alpha > -0.5$) and/or inverted ($\alpha > 0$) spectral indices. The flattening observed in these sources is also seen in μJy sources (e.g. Windhorst et al., 1993; Randall et al., 2012) and could suggest the effects of SSA which is a key feature for the morphology of radio jets on sub-kpc scales.

In Fig. 4.8, I show the spectral index dependence on the total projected size of the objects. We see that all of the compact sources in our sample have estimated sizes that are very small ($<$1 kpc) as expected. 7 of these objects show steep spectral indices ($\alpha < -0.5$) while 36 objects display flat/inverted spectral indices ($\alpha > -0.5$). We also observe that all extended objects in the VLA images have sizes > 1 kpc (as expected) with 5 objects showing steep radio spectra, whereas 4 objects show flat radio spectra. We also note two distinct categories of compact flat radio spectrum populations and resolved steep radio spectrum populations. These are analogous to CSS objects and consistent with the idea that compact RLAGN are physically small in size, young and rapidly growing objects (e.g. Snellen et al., 2000; O'Dea and Saikia, 2021) that could potentially grow into the more extended and powerful Fanaroff and Riley FRI/II objects.

At this point, it is crucial to understand the nature of flat-spectrum sources, a property consistent with self-absorption at low frequencies. In the next section, I investigate the effects of SSA for compact classed objects with flat radio spectra (i.e. $\alpha > -0.5$).

end of Fig. 4.7 thus $\alpha = -1.30,\ -1.27,$ and $-\ 1.31$ respectively.

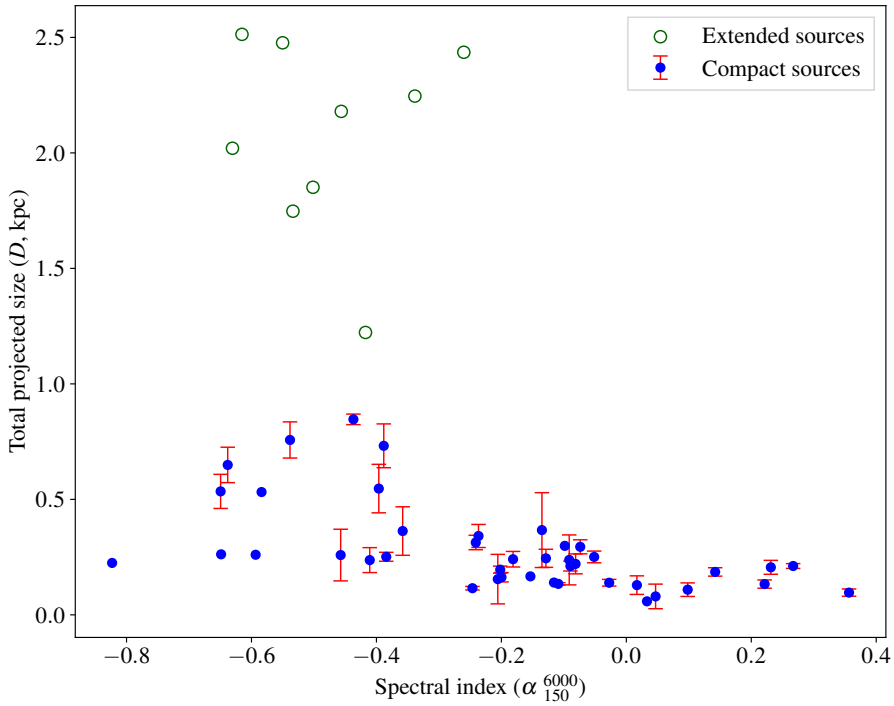

Figure 4.8: The distribution of total projected sizes against spectral indices of sources. In green (open circles) are extended objects while in blue are compact objects. Sizes of extended objects are maximum lengths while the sizes of compact sources are given by their upper limits; the error bars in compact sources are also shown for objects where the errors were obtained using IMFIT. We see that flat/inverted spectral indices are associated with compact sources.

4.5.2 Investigating synchrotron self-absorption (SSA)

An interesting feature of our sources is that they show steep and flat radio spectra at 150 MHz. Many of these sources ($43/55;\ 78\%$) are compact compared to the limiting angular resolution of 0.35 arcsec of the VLA, a characteristic that suggests self-absorption at low frequencies. Therefore, it is natural to investigate whether these sources are self-absorbed in the context of SSA, and here, I attempt to derive the properties of the region responsible for this emission.

All the radiation in a synchrotron emitting source is ideally expected to reach the observer, however, there are cases when this radiation interacts with relativistic particles on its way out of the plasma of the emitting source causing a scattering that results in its absorption. This process is called synchrotron self-absorption (SSA; Kellermann, 1966). SSA models can be used to estimate the radio properties of compact RLAGN such as GPS and CSS sources. For instance, the observed spectral turnover at GHz frequencies in GPS/CSS sources may suggest SSA (e.g. O'Dea and Baum, 1997; Snellen et al., 2000). SSA can further be used to estimate magnetic fields and predict physical sizes (e.g. Kim et al., 2022; Patil et al., 2022) of the compact synchrotron emitting source.

To estimate the properties of the emitting region, I assume SSA at 150 MHz, I assume that these sources have an ellipsoidal geometry, and I consider a case where these objects are in equipartition assuming no non-radiating particles. To do this, I start from the definition of the absorption coefficient of synchrotron

radio emission presented in Sec. 2.2.1 thus

$$\chi_\nu = \frac{\sqrt{3}e^3 c}{8\pi^2 \epsilon_0 m_e} k B^{(p+2)/2} \left(\frac{3e}{2\pi m_e^3 c^4}\right)^{p/2} b(p) \nu^{-(p+4)/2} \tag{4.1}$$

where ν is the observing frequency, k is the normalization of the electron energy spectrum defined by $N(E) = kE^{-p}$, p is the electron energy index given by $\alpha = -(p-1)/2$, c is the speed of light, e is the charge of an electron, m_e is the electron mass, ϵ_0 is the permittivity of free space, μ_0 is the permeability of free space, and

$$b(p) = \frac{\sqrt{\pi}}{8} \frac{\Gamma\left(\frac{3p+22}{12}\right) \Gamma\left(\frac{3p+2}{12}\right) \Gamma\left(\frac{p+6}{4}\right)}{\Gamma\left(\frac{p+8}{4}\right)} \tag{4.2}$$

is a constant that depends on the value of the exponent p; for $\alpha = -0.5$, we have $p = 2$ therefore, $b(p) = 0.269$ (see Longair, 2011, for details on constants). Note that the Γs, in this case, are gamma−functions. Evaluating the constants, Eq. 4.1 can be recast and presented in SI units as

$$\chi_\nu = 3.354 \times 10^{-9} k B^{(p+2)/2} (3.54 \times 10^{18})^p b(p) \nu^{-(p+4)/2} \ \ \mathrm{m}^{-1} \tag{4.3}$$

and I can estimate B (the source equipartition magnetic field) using the derivations of Hardcastle et al. (2004) thus

$$B = \left(2\mu_0(1+\kappa)\frac{J(\nu)}{C}\nu^{(p-1)/2} I\right)^{2/(p+5)}. \tag{4.4}$$

From Eq. 4.4, $J(v)$ is the synchrotron emissivity which can be computed from the source luminosity and volume (i.e. $J(\nu) = L_{\mathrm{radio}}/V$). Eq. 4.4 shows that the magnetic field B depends on the sources' observables such as the flux density, redshift, observing frequency, and the sources' measured Gaussian angular sizes ($\theta_{\mathrm{M}}^{\mathrm{D}} \times \theta_{\mathrm{m}}^{\mathrm{D}}$); in this case, I estimate $B-$fields at 6 GHz. The κ term, the energy density ratio between non-radiating and radiating particles, is given by $\zeta = 1 + \kappa$. In the case of SSA, $\zeta = 1.0$ for no non-radiating particles and

$$I = \begin{cases} \ln(\mathrm{E_{max}}/\mathrm{E_{min}}), & p = 2 \\ \frac{1}{(2-\mathrm{p})[\mathrm{E_{max}}^{(2-\mathrm{p})} - \mathrm{E_{min}}^{(2-\mathrm{p})}]}, & p \neq 2 \end{cases}, \tag{4.5}$$

$$C = c(p)\frac{e^3}{\epsilon_0 c m_e}\left(\frac{m_e^3 c^4}{e}\right)^{-(p-1)/2}, \tag{4.6}$$

and

$$E = \gamma m_e c^2. \tag{4.7}$$

The quantity $c(p)$ is dimensionless and is of order 0.050 for $p = 2$. Eq. 4.3 tells us that SSA will be

important if:

$$\tau = \chi_{\nu}.d \approx 1 \tag{4.8}$$

where d is the depth of the compact object in meters determined from the object's angular minor axis scale ($\theta_{\rm m}^{\rm D}$; Table 4.6) and I work at v =150 MHz. Using this analysis, the information presented in Tables 4.1 and 4.6, and utilising the PYSYNCH code[11] to estimate $B-$fields (Hardcastle et al., 1998b) for each object, I find for the measured sizes of compact objects that Eq. 4.8 is not satisfied which implies either of two possibilities: (1) the objects are not absorbed at 150 MHz or (2) the measured sizes (upper limits) presented in Table 4.6 are overestimates. The question then arises as to what sizes these objects have to have to be self-absorbed at 150 MHz. I answer this question by reducing the volume of the measured sizes for each object (Table 4.6) by a factor between $2-100$ until the condition set in Eq. 2.23 is met. The results are presented in Table 4.8 where we see that the SSA predicted sizes for these sources are well below the measured Gaussian sizes presented in Table 4.6.

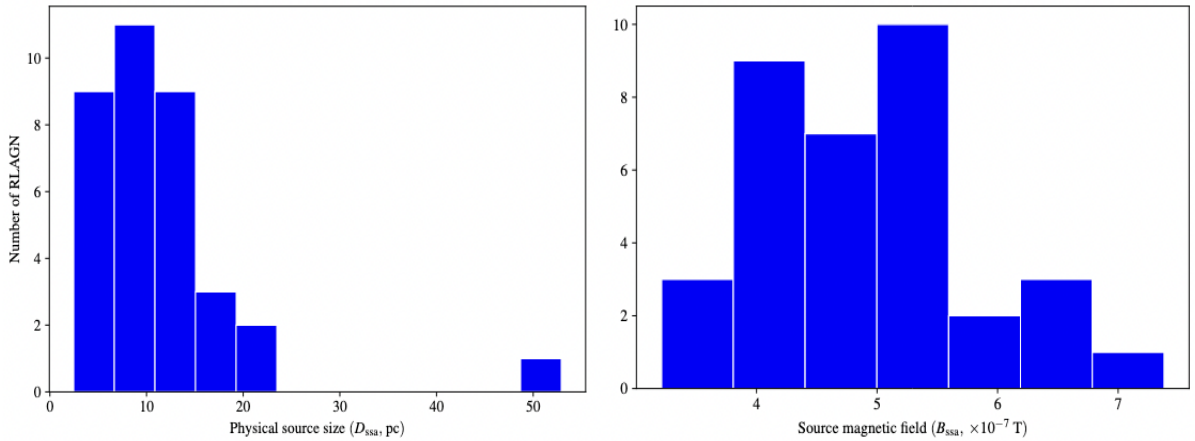

Figure 4.9: Distribution of source predicted physical sizes (left panel; in parsec) and source equipartition magnetic fields (right panel; in Tesla) assuming SSA at 150 MHz.

The distribution of the predicted physical sizes and magnetic fields for the flat/inverted 35 compact objects are shown in Fig. 4.9. I find that the sizes of these low-luminosity compact RLAGN have to be in the range of milliarcsec scales ($\sim 2-30$ mas) corresponding to $\sim 2-53$ pc in linear scales if they are to be self-absorbed at 150 MHz. Comparisons of these predicted sizes with observed sizes are not yet possible in our case, except for J1213+50 and J1230+47 which are resolved at sub-parsec resolution in the Very Long Baseline Interferometry (VLBI; e.g. Kellermann and Moran, 2001), the Very Long Baseline Array (VLBA; e.g. Napier, 1994), and the European VLBI Network (EVN; e.g. Schilizzi, 1995) observations at 8.4, 5, and 8 GHz respectively (Cheng and An, 2018; Cheng et al., 2021) and are therefore consistent with our predictions. These two objects show two-sided jetted morphologies extending up to a few pc in projected physical scales. The angular sizes predicted for all the 35 RLAGN sources in Table 4.8 are well below the resolution of LOFAR (6 arcsec) and the VLA (0.35 arcsec), which means that they can only be resolved at much lower angular scales with long baselines such as the enhanced Multi-Element Remotely Linked Interferometer Network (eMERLIN; e.g. Davies et al., 1980), VLBA, and/or EVN at milliarcsec

[11] https://github.com/mhardcastle/pysynch/

Table 4.8: Property estimates of compact RLAGN assuming SSA. The first column indicates the LOFAR source name, column 2 shows the measured linear size (Table 4.6; in pc) for comparison with the predicted SSA maximum linear size, column 3 shows diameter estimates of the size of the object assuming an ellipsoid shape, column 4 shows estimates of the sources magnetic fields (in Tesla) derived at 6 GHz and using Eq. 4.4. Column 5 indicates the electron number density, and column 6 shows the maximum physical size estimates (in pc) computed using values in column 3 and redshift information presented in Table 4.1. Column 7 presents estimates of the absorption coefficient satisfying SSA at 150 MHz, and the final column shows the object's depth in meters.

LOFAR source name	Estimated linear size	$D_{\rm ssa} \times d_{\rm ssa}$	$B-$field	k	$D_{\rm ssa}$	χ_v	$d_{\rm ssa}$
	(D, pc)	(arcsec)	($\times 10^{-7}$, T)	($\times 10^{-9}$, m^{-3})	(pc)	($\times 10^{-16}$, m^{-1})	($\times 10^{16}$, m)
ILTJ105535.82+462903.3	166.72	0.0059 × 0.0023	5.12	9.07	9.81	0.08	11.80
ILTJ110233.62+513124.3	341.52	0.0079 × 0.0022	5.39	10.03	10.35	0.10	8.84
ILTJ111745.92+473327.5	251.48	0.0084 × 0.0046	4.39	6.67	11.98	0.04	20.27
ILTJ113545.33+491619.6	244.84	0.0048 × 0.0037	5.00	8.64	4.90	0.07	11.81
ILTJ113757.19+554207.5	220.71	0.0063 × 0.0026	5.28	9.62	7.61	0.09	9.70
ILTJ114047.35+463225.5	96.39	0.0132 × 0.0127	3.61	4.50	13.77	0.02	40.84
ILTJ114316.26+551639.9	139.13	0.0109 × 0.0096	4.08	5.75	11.59	0.03	31.55
ILTJ114721.40+554348.4	128.73	0.0064 × 0.0032	5.28	9.64	6.44	0.09	9.93
ILTJ115157.87+532845.5	250.80	0.0081 × 0.0025	5.37	9.96	9.29	0.10	8.94
ILTJ115205.79+545817.1	162.99	0.0078 × 0.0040	4.79	7.92	9.05	0.06	14.31
ILTJ115330.55+524121.8	195.79	0.0102 × 0.0078	3.99	5.50	13.99	0.03	33.05
ILTJ115438.10+491851.4	109.06	0.0087 × 0.0043	4.92	8.35	9.09	0.07	14.02
ILTJ115531.40+545200.4	133.33	0.0229 × 0.0064	4.58	7.25	22.22	0.05	19.17
ILTJ121329.29+504429.4	115.42	0.0208 × 0.0163	4.02	5.58	12.82	0.03	30.93
ILTJ123011.86+470022.7	134.12	0.0216 × 0.0151	3.82	5.05	16.76	0.02	36.14
ILTJ123301.22+561013.7	366.99	0.0052 × 0.0020	5.49	10.40	7.98	0.10	9.23
ILTJ124021.48+475143.6	546.73	0.0038 × 0.0037	4.40	6.69	6.92	0.04	20.93
ILTJ130325.87+523522.5	294.58	0.0119 × 0.0038	4.43	6.78	21.04	0.04	20.63
ILTJ130535.92+540142.5	211.23	0.0114 × 0.0085	3.61	4.50	19.20	0.02	44.28
ILTJ131002.06+540005.2	298.75	0.0090 × 0.0015	5.64	10.98	14.94	0.12	7.43
ILTJ132745.67+544756.8	237.04	0.0038 × 0.0031	6.12	12.93	2.50	0.16	6.37
ILTJ133430.04+502718.3	362.89	0.0029 × 0.0017	5.57	10.71	4.59	0.11	8.58
ILTJ134233.86+485316.2	731.83	0.0062 × 0.0018	5.49	10.41	10.45	0.11	9.26
ILTJ135632.65+493710.9	185.86	0.0086 × 0.0045	4.54	7.11	10.93	0.05	17.58
ILTJ140013.20+462556.0	258.87	0.0024 × 0.0017	6.33	13.84	2.46	0.19	5.36
ILTJ141149.57+545733.1	205.89	0.0087 × 0.0061	4.06	5.71	13.73	0.03	29.57
ILTJ141234.88+494611.5	237.94	0.0048 × 0.0039	4.60	7.32	6.43	0.05	16.46
ILTJ142025.23+544016.1	139.95	0.0065 × 0.0018	6.30	13.73	5.38	0.18	4.69
ILTJ142125.51+482933.3	211.54	0.0141 × 0.0085	3.85	5.12	19.23	0.03	35.96
ILTJ142707.30+525001.5	313.33	0.0069 × 0.0030	4.80	7.96	10.80	0.06	14.67
ILTJ142948.48+535754.2	154.77	0.0091 × 0.0011	7.38	18.83	7.74	0.34	2.89
ILTJ143334.77+524310.2	240.96	0.0059 × 0.0020	6.24	13.47	5.24	0.18	5.35
ILTJ143521.75+505123.0	846.45	0.0288 × 0.0126	3.21	3.57	52.90	0.01	71.31
ILTJ145350.18+540440.9	58.59	0.0064 × 0.0054	4.01	5.55	11.72	0.03	30.51
ILTJ145415.10+492549.9	79.87	0.0072 × 0.0055	5.03	8.73	5.32	0.07	12.48

resolution. Shown in Table 4.8 and Fig. 4.9 are also estimated magnetic fields, a vital property that can help us constrain evolutionary stages of young RLAGN (e.g. Orienti and Dallacasa, 2008). I estimate $B-$field values lying between $\sim$0.3$-$0.75 μT for SSA and are comparable to those estimated in CSS (e.g. Dallacasa et al., 2002) sources. If accurate, these provide useful information about the physical conditions in these sources.

4.5.3 Radio power-linear size ($P-D$) diagram

The radio spectra for our RLAGN have shown that these sources could also be drawn from the RLAGN population of CSS objects. If this is true, then we expect our sources to populate the position that CSS objects occupy on the $P-D$ diagram. Here, I briefly describe the construction of the $P-D$ diagram and I discuss the position of our VLA sample in the $P-D$ space with respect to the position of other compact RLAGN such CSSs, CSOs, GPSs, LINERs, Seyferts, as well as the main LoTSS DR1 RLAGN

sample that incorporates FRI/FRIIs.

The $P-D$ diagram is important in modelling the evolution of extended RLAGN (Baldwin, 1982). Its construction depends on observational measurements of the radio object's flux density, maximum angular size, and redshift (Hardcastle et al., 2016). These measurements directly result in estimates of the radio luminosity (P) and the maximum physical size (D). The $P-D$ diagram, therefore, offers another way of investigating the evolution of various RLAGN classes such as GPSs, CSSs, CSOs, RQQs, LINERs, Seyferts, and FRI/FRIIs. However, the evolution of RLAGN depends on intrinsic source factors such as the central engine properties (e.g. nuclear activity and jet power) and environmental factors (e.g. interaction of jets and the ISM).

CSS, GPS, and CSO sources have radio powers $P_{1.4\ \mathrm{GHz}} > 10^{25}$ W Hz^{-1} while their sizes are typically smaller than 2 arcsec thus $D \lesssim 20$ kpc for CSS objects, $D \lesssim 1$ kpc for GPS objects, and $D \lesssim 500$ pc for CSO objects. However, low-luminosity $P_{1.4\ \mathrm{GHz}} < 10^{24}$ W Hz^{-1} CSOs have also been observed (e.g. An and Baan, 2012) with maximum projected sizes of < 1 kpc. Tracking these objects on the $P-D$ diagram suggests that CSSs descend from the population of GPSs and are in turn expected to grow into FRIIs (i.e. GPS/CSS objects reveal radio morphologies similar to FRIIs but on much smaller scales e.g., O'Dea and Saikia, 2021). RQQs on the other hand are compact RLAGN with moderately low radio powers estimated between $10^{23} \lesssim P_{1.4} \lesssim 10^{25}$ W Hz^{-1}. Their projected sizes span $\sim$1$-$25 kpc. LINERs and Seyferts, however, have very low radio powers $P < 10^{22}$ W Hz^{-1} with sizes spanning $\sim$10$-$100 pc (see Gallimore et al., 2006; Ho, 2008). In the radio regime, LINERs and Seyferts cover the lower end of the $P-D$ diagram. Recall from Chapter 2 that FRI/II objects exhibit two distinct ranges of radio power with their radio emission travelling to distances out on kpc and sometimes Mpc scales (e.g. Neeser et al., 1995); FRIs have radio luminosities $P_{178} < 10^{25}$ W Hz^{-1} while FRIIs show radio-powers $P_{178} > 10^{25}$ W Hz^{-1} (Fanaroff and Riley, 1974). FRI/II objects, therefore, cover two radio power regimes dividing at around $L_{178\ \mathrm{MHz}} \sim 10^{25}$ W Hz^{-1}. However, recent studies (e.g. Mingo et al., 2019) from LoTSS show that radio luminosities for FR populations overlap at low frequencies (i.e. at $z \leq 0.8$, some FRIIs show $P_{150} \leq 10^{25}$ W Hz^{-1}). Both FRI/II objects extend over kpc scales with FRIIs sometimes extending to Mpc scales (e.g. Willis et al., 1974).

Fig. 4.10 shows a $P-D$ diagram for the 23 344 LoTSS DR1 RLAGN sample selected by Hardcastle et al. (2019) using the AGN-SF techniques described in Sec 4.1.2. The sample consists of both resolved sources (in green)[12] and unresolved sources (in blue)[13] at 6 arcsec LOFAR resolution. The 23 344 RLAGN sample is overlaid with the position of the extended and compact VLA 6 GHz RLAGN under study. The VLA extended objects (in magenta) show radio powers ranging between $10^{22} < P_{150} < 10^{24}$ W Hz^{-1} and extend between $1 < D < 2$ kpc in linear size. The compact VLA objects (in salmon) exhibit the same radio powers as the extended objects except for an outlier object with radio power $\log_{10}(L_{150\ \mathrm{MHz}}) = 24.9$ W Hz^{-1}. The physical sizes of compact sources are however $D < 1$ kpc. For the VLA compact objects, I have taken estimates of their sizes as upper limits from the deconvolved

[12] This sample has been studied in detail by Mingo et al. (2019) and consists of both FRI and FRII sources.
[13] Size estimates are given by upper limits of the deconvolved size plus thrice the associated error.

major axis (see Table 4.6). Following the discussion above, we see that our RLAGN do not occupy a special place on the $P - D$ diagram with regard to the different classes of AGN discussed. However, we see them populate the bottom left side of the $P - D$ space, a position that corresponds to the position of low-radio power CSOs in their very early evolutionary stage (see, for example, the $P - D$ diagram in Hardcastle and Croston, 2020, and references therein).

The evolutionary tracks (dashed black lines) shown in Fig. 4.10 were derived by Hardcastle (2018b) using analytical methods (see the reference for details) and represent jet powers Q thus $Q = 10^{35-40}$ W from bottom to top. These tracks together with other analytical models (e.g. Kaiser and Alexander, 1997; Blundell et al., 1999; Hardcastle and Krause, 2013; Godfrey et al., 2017; Turner et al., 2018) describe the evolutionary path of RLAGN that start with young CSOs and evolve into FRIIs provided environmental conditions sustaining RLAGN evolution are met (e.g. An and Baan, 2012). Our objects, therefore, are expected to follow these evolutionary routes if they are to evolve into more extended low-luminosity FRI/II sources. The diagonal line (blue) follows qualitative analyses by Hardcastle et al. (2016) and shows surface brightness limitations where low-redshift, low-luminosity, and large-scale sources can not be detected with LOFAR.

4.5.4 Comparison with similarly compact RLAGN sources

In this section, I aim to draw a comparison or a relationship between the nature of our compact sources with other unresolved compact RLAGN that have previously been studied in radio surveys at high resolutions in the local RLAGN Universe (e.g. Sadler et al., 2014; Baldi and Capetti, 2010); these unresolved objects in the local Universe are sometimes referred to as 'FR0s' (Baldi et al., 2015, 2016). This terminology (used to describe an unresolved source) comes that they lack substantial emission, making them a factor of $\sim$30 more core-dominated than typical FRIs despite sharing similar radio properties. However, and as noted by Hardcastle and Croston (2020), the 'FR0' nomenclature can only be exclusively adopted when observations capable of resolving these sources are available as is in the case with the Fanaroff and Riley morphological classification.

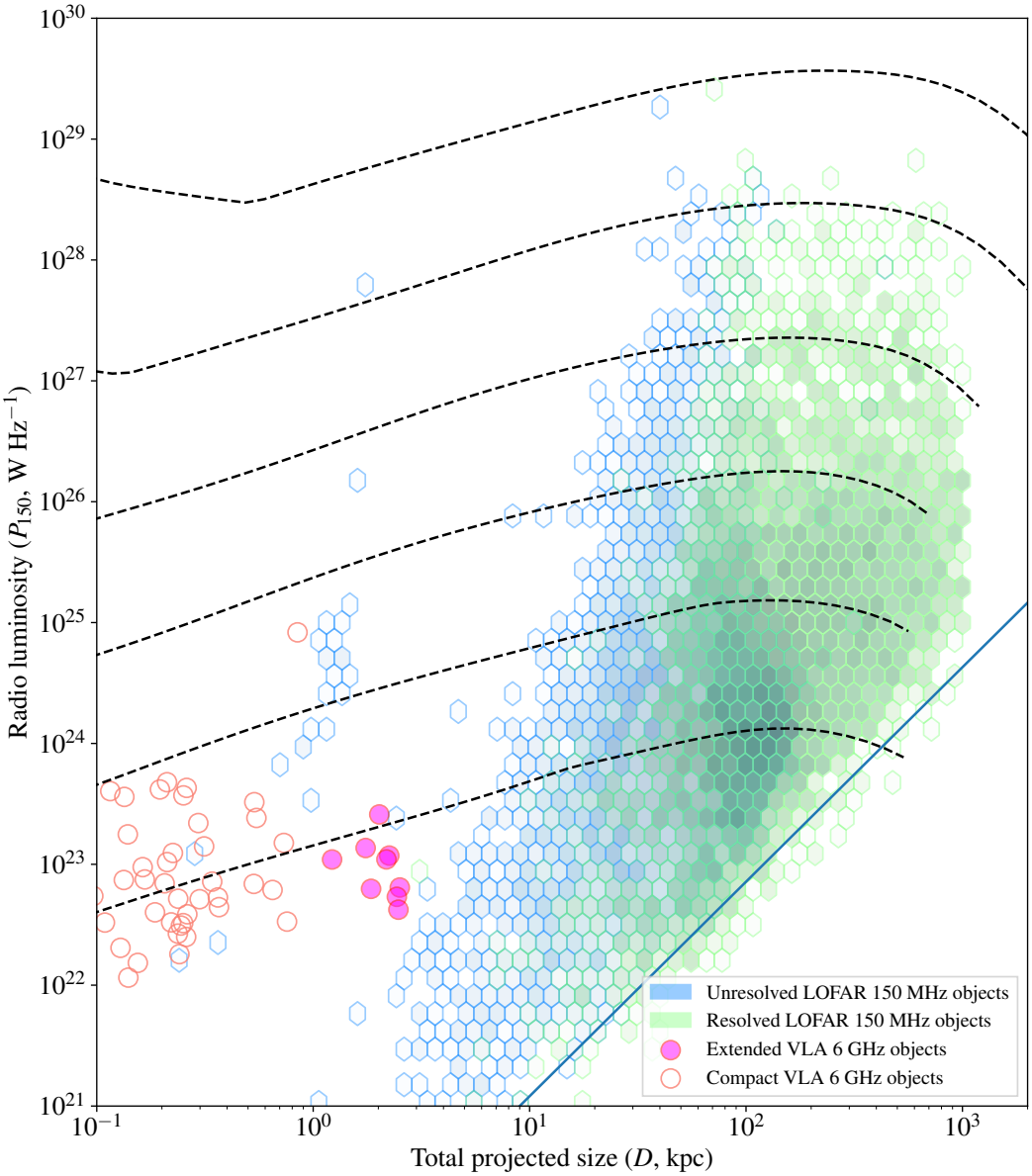

Figure 4.10: A power-linear size diagram of the 23 344 RLAGN sample constructed by the methods of Hardcastle et al. (2019) as discussed in Sec. 4.1.2 overlaid with a LOFAR sub-sample resolved by the VLA at sub-arcsec resolution. There are a total of 16 494 sources that are unresolved (blue) and 6 850 sources that are resolved (green) by LOFAR. Magenta points show those objects (9) that appear extended in the VLA images while salmon points (43) show compact objects at VLA's 6 GHz. The linear sizes for unresolved LOFAR sources are determined from the upper limits of the deconvolved size plus thrice the associated error. For the VLA compact objects, the sizes are estimated from twice the size of the deconvolved major axis. Colours are adjusted to ensure that all points are visible. Following qualitative analyses derived by Hardcastle et al. (2016), the diagonal line in blue shows the area where radio sources are undetectable by LOFAR, due to surface brightness limitations. Jet powers (Q) are represented by dashed lines (evolutionary tracks) thus $Q = 10^{35-40}$ W from bottom to top. These were derived for $z = 0$ sources in a galaxy group defined by $M_{500} = 2.5 \times 10^{13} M_{\odot}$, and $kT = 1$ keV (Hardcastle, 2018b).

The local Universe is dominated by unresolved RLAGN, among which are what have become popularly known as FR0s. They are mainly associated with compact RLAGN that are spectroscopically classified as LERGs (Baldi et al., 2015, 2016; Baldi et al., 2018; Baldi et al., 2018, 2019) revealing a range of radio properties on smaller scales (<100 kpc). However, a couple of HERGs with FR0-like features have also been observed at high-frequency resolution (e.g. Pierce et al., 2020). Collectively, FR0s and FRIs display similar radio and host galaxy properties. The only observed difference thus far is the lack of sub-

stantial emission seen in FRIs. In their pilot study, Baldi et al. (2015) presented 8 FR0s selected from the AGN population ($z < 0.1$) constructed by Best et al. (2005a). These objects had radio powers between 10^{22-26} W Hz^{-1} at 1.4 GHz and inhabit red massive ($\sim 10^{11}$ M$_\odot$) early-type galaxies (ETGs; BH$\geq 10^8$ M$_\odot$). High resolution multi-frequency (1.4, 4.5, and 7.5 GHz) VLA observations of these 8 FR0 objects revealed a range of radio properties. 4 RLAGN showed extended radio emission, 1 of which was classified as a HERG showing a hybrid of FRI/FRII radio morphology (maximum projected size of up to 40 kpc). 3 FR0s were classified as LERGs showing extended radio emission spanning $1-3$ kpc. The remaining 4 objects were compact at the limiting angular resolution of 0.2 arcsec, corresponding to $0.2-0.4$ kpc in projected physical scales (Baldi et al., 2016). Their radio spectral indices range between $-1.16 \leq \alpha \leq -0.04$.

Given that both the RLAGN sample presented in this work and the Baldi et al. FR0 sample were selected from the local Universe, show comparable radio powers ($10^{22} \leq L_{150\ \mathrm{MHz}} \leq 10^{24}$ W Hz^{-1}), comparable projected physical scales (i.e. $0.1-0.8$ for compact RLAGN and $1-3$ kpc for extended RLAGN), and similar morphologies to our sample, it is likely that our objects can be placed in the same class as FR0s: a comparison between the two populations is significant in constraining the nature of our sample; I use their radio spectra for this analysis. It should be noted however that a major distinction between the two sample populations is that all our objects are selected as HERGs with BH masses lying between 10^{6-11} M$_\odot$ (Sabater et al., 2019). Baldi et al. (2019) studied a sample of 18 FR0s selected from the FR0 catalogue, FR0CAT (Baldi et al., 2018); this catalogue consists of 104 FR0s. Most of the objects in FR0CAT are classified as LERGs and include $z \leq 0.05$ sources with radio powers between 10^{22-24} W Hz^{-1} at 1.4 GHz. Their sizes have an upper limit of 5 kpc in projected physical sizes. This catalogue includes 66 FR0s that are in LoTSS DR2 area (Capetti et al., 2020) among which are 4 sources in our sample: J1048+48, J1126+52, J1213+50, and J1230+47.

Baldi et al. (2019) obtained A-array multi-frequency (1.5, 4.5, and 7.5 GHz) high resolution VLA observations of 18 FR0s, which include 2 (J1213+50 and J1230+47) objects from our compact RLAGN sample. They derived core-radio spectra for all the 18 sources between 1.5 and 4.5 GHz spanning $-1.03 < \alpha < 0.60$. 6 (33%) FR0s showed steep spectral indices ($\alpha < -0.49$) while 11 (61%) FR0s showed flat spectral indices ($\alpha > -0.49$). Only 1 FR0 showed a strongly inverted radio spectrum i.e. $\alpha = 0.6$. In comparison to the distribution of spectral indices for our sources, 16 (29%) objects show steep spectral indices ($\alpha < -0.5$), 30 (54%) show flat spectral indices ($-0.5 < \alpha < 0$), and 9 (16%) show an inverted radio spectrum ($\alpha > 0$). However, J1213+50 and J1230+47 remain flat (see Table 4.6) in the Baldi et al. FR0 sample between 1.5 and 4.5 GHz that is $\alpha = -0.33$ and $\alpha = -0.29$ respectively[14]. The median spectral index values between the two populations are $\bar{\alpha} = -0.25$ for the 55 RLAGN sample under study and $\bar{\alpha} = -0.28$ for the 18 FR0s respectively. However, Baldi et al. (2019) reported a radio spectral steepening increment (38%) between 4.5 and 7.5 GHz for the 18 FR0s (median value $\bar{\alpha} = -0.38$). I find, after a K$-$S[15] test, that the null hypothesis that our sources are drawn from the same spectral index distribution as the Baldi et al. FR0s (1.5$-$4.5 GHz) can not be rejected at a confidence

[14] They also remain flat between 4.5 and 7.5 GHz with spectral indices $\alpha = -0.29$ and $\alpha = -0.47$ respectively.
[15] Two$-$sample Kolmogorov–Smirnov test.

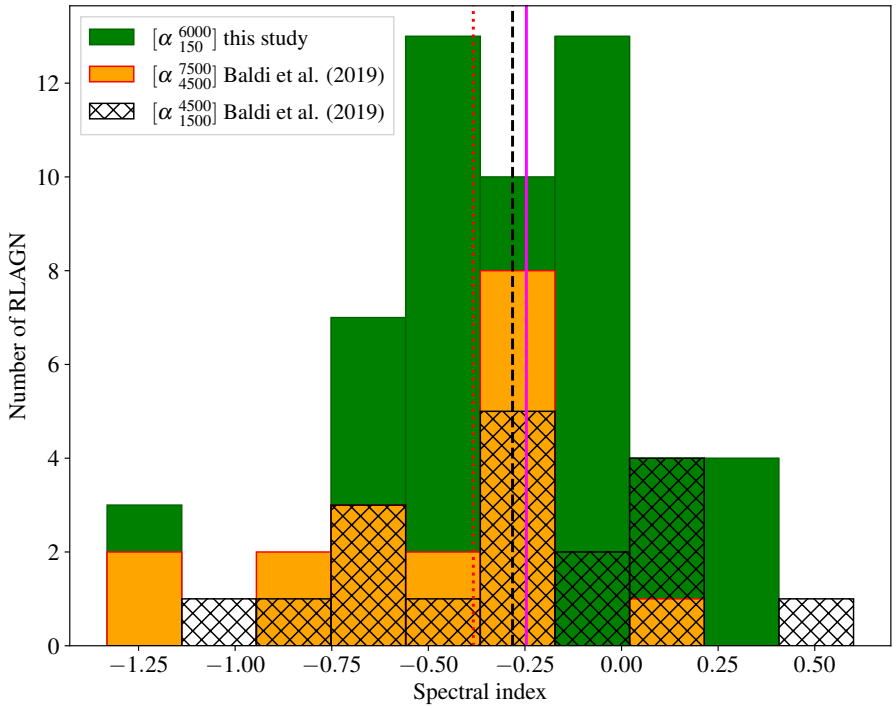

Figure 4.11: Comparison in the spectral index distribution between the Baldi et al. FR0 sample and the RLAGN presented in this work. Green bins show the radio spectra distribution for the whole sample presented in this thesis overlaid with hatched bins representing the radio spectra of Baldi et al. FR0s measured at 1.5 and 4.5 GHz VLA frequencies. Orange bins represent the radio spectra for the Baldi et al. FR0 sample measured between 4.5 and 7.5 GHz VLA frequencies. The solid magenta line, the black dashed line, and the red dotted line show spectral index median values that is $\bar{\alpha}^{6000}_{150} = -0.25$, $\bar{\alpha}^{4500}_{1500} = -0.28$, and $\bar{\alpha}^{7500}_{4500} = -0.38$ respectively for our RLAGN and FR0s.

level of 77.01% ($p$value $= 0.7701$)[16]. A comparison in the distribution of spectral indices as discussed above are shown in Fig. 4.11.

In terms of their radio morphologies, the Baldi et al. FR0 sample share similar radio morphologies with our extended RLAGN. Firstly, 4/18 FR0s show extended radio emission in the VLA images projected at $2-14$ kpc in maximum physical size. One object, J1213+50 shows marginally extended radio emission (projected maximum length of $\sim$2 kpc) particularly at 4.5 and 7.5 GHz in the Baldi et al. FR0 sample while it is compact in our VLA images at 6 GHz. In comparison, the extended objects in our sample lie within the extended FR0's range and have projected maximum sizes between $1-3$ kpc. Secondly, the FR0 extended sources show a wide range of morphologies: two-sided jets, one-sided jets, doubles, and complex, consistent with our extended objects. The source J1230+47 remains compact at all the VLA frequencies in the FR0 sample as well as in our catalogue. All the 4 RLAGN objects in the FR0CAT sample are compact in the DR2 area (Capetti et al., 2020) but show parsec scale extended radio emission in the eMERLIN, VLBI, and EVN detailed studies of FR0s (Cheng and An, 2018; Cheng et al., 2021; Baldi et al., 2021).

Could there be a large population of HERG-FR0 sources? Recently, Pierce et al. (2020) presented a

[16]The null hypothesis that these sources are drawn from the same spectral index distribution can be rejected at a high confidence level of 96% ($p$value $= 0.041$) between the radio spectra of our RLAGN and the Baldi et al. FR0 spectra measured between 4.5 and 7.5 GHz. One caveat that could affect the results in this analysis is the low-redshift selection of the Baldi et al. sources; only 12/55 RLAGN in our catalogue include sources with redshift $z \leq 0.05$ (see Fig. 4.3).

sample of 16 RLAGN ($z < 0.1$) with comparable radio powers ($22.5 < \log(L_{1.4}) < 25.0$ W Hz^{-1}) to our observations. These objects were optically classified as HERGs (Pierce et al., 2019). The 16 Pierce et al. (2020) HERG objects were observed with the VLA at both L- and C-bands. High resolution VLA images of the 16 HERG sample showed a variety of radio morphologies in 7 extended objects however, they differ in projected physical scales with our extended RLAGN; the 7 extended Pierce et al. HERG objects were extended on larger scales ($2-19$ kpc: median value $= 6.1$ kpc) compared to our 9 extended objects ($1-3$ kpc: median value $= 2.18$ kpc). However, it should be noted that the extended radio emission in the Pierce et al. sample were estimated at the 5σ contour boundary compared to our extended RLAGN sample estimated at 3σ contour boundary. The remaining objects (9/16) in the Pierce et al. HERG sample were compact at the same limiting angular resolution of $\sim$0.3 arcsec with our sources. This corresponds to projected physical scales of $\sim 0.28-0.54$ kpc, comparable to our compact sources' projected sizes ($\sim 0.1-0.8$ kpc).

Further differences between the two populations can also be seen in their radio spectra. The Pierce et al. HERG sample display steep spectral indices between $1.5-4.5$ GHz (median value: $\bar{\alpha} = -0.75$) and between $4.5-7.5$ GHz (median value: $\bar{\alpha} = -0.99$) while a majority of compact objects in our sample show flat radio spectra (median value: $\bar{\alpha} = -0.25$). Repeating the K$-$S test as above, I find between our RLAGN and the Pierce et al. sample (in both instances thus between $0.15-6$ GHz and $1.5-4.5$ GHz: $p$value$= 0.00029$ and between $0.15-6$ GHz and $4.5-7.5$ GHz: $p$value$= 8.34 \times 10^{-6}$) that the null hypothesis that these sources are drawn from the same spectral index distribution can be rejected at a high confidence level of 99.971% and 99.999% respectively. Fig. 4.12 presents a summary of the above discussion.

I speculate that the differences in the spectral index distribution between the Pierce et al. sample, together with the Baldi et al. sample discussed above, is down to differences in their observing frequencies; flux measurements at high frequencies tend to display steeper spectral indices, whereas self-absorption flattens the spectra of sources at lower frequencies (e.g. at 150 MHz).

To summarise this section, I have highlighted close similarities in radio morphology and radio luminosity between our RLAGN and the Baldi et al. FR0s. The distribution of spectral indices of our objects and the Baldi et al. FR0 sources also show close similarities, particularly for those FR0s measured between 1.5 and 4.5 GHz observing frequencies (Baldi et al., 2019). The main distinction between the two populations comes from the fact that the Baldi et al. sample is spectroscopically classified as LERGs while our sources are radiatively efficient RLAGN (HERGs). The high core dominance observed in our sample is consistent with that observed in the Baldi et al. FR0s at different observing bands. However, based on the fact that FRIs are typically associated with LERGs, we can rule out the possibility that our HERG sample could be the younger and smaller-scale versions of FRI sources. Further multi-frequency (e.g. at 1.5, 4.5, and 7.5 GHz) high-resolution observations of our RLAGN sample with the VLA and with long-baseline interferometers would help in confirming if these galaxies can be placed in the same pool as the FR0s.

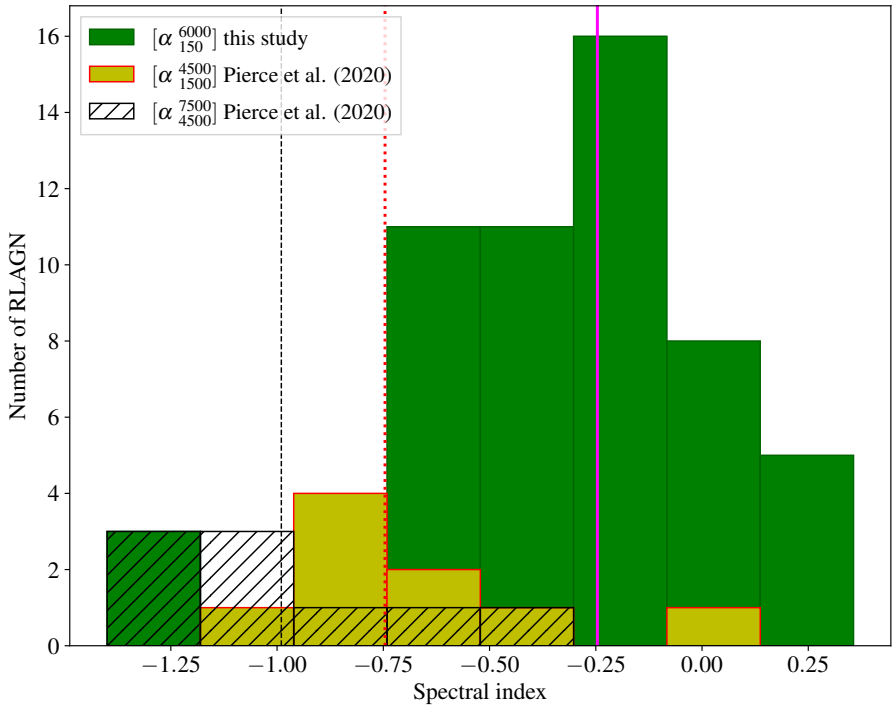

Figure 4.12: A spectral index distribution comparison between our HERG compact sample and the Pierce et al. HERG compact sample. The magenta solid line shows the median spectral index for our observations ($\bar{\alpha}^{6000}_{150} = -0.25$) while the black dashed line and the red dotted line represent the median spectral index of the Pierce et al. sample, respectively $\bar{\alpha}^{7500}_{4500} = -0.99$ and $\bar{\alpha}^{4500}_{1500} = -0.75$.

4.6 Summary

I have attempted to constrain the nature of 55 low-luminosity RLAGN selected from LoTSS DR1. I have discussed the radio spectrum of these sources where I have shown that a majority of these objects (39 out of 55) show flat spectral indices, a feature that is associated with the cores of more powerful and extended RLAGN such as FRI/IIs. The remaining objects (16 out of 55) show steep spectral indices, a feature associated with the jets of large-scale RLAGN. I have also attempted to investigate synchrotron self-absorption at 150 MHz for the 35 sources with flat/inverted radio spectra. I predict the sizes for these objects to lie between $2-53$ pc in projected physical scales while I estimate small B-fields to lie between $0.3-0.75$ μT. I also find that our objects occupy the lower left-end of the $P-D$ diagram, a position occupied by low-luminosity CSOs. Finally, I have compared our object's radio properties with those of similarly compact RLAGN such as the Baldi et al. FR0s; I find close similarities in radio luminosity, radio spectra, radio morphology, and projected physical sizes. However, I find differences in the spectral index distribution with the Pierce et al. low-redshift, low-luminosity compact HERG sample (these sources have FR0-like features) despite their objects having comparable radio-powers and projected physical sizes to our objects.

Chapter 5

VLA sources with extended radio emission in LoTSS DR2

This Chapter presents VLA objects showing extended radio emission in LoTSS DR2.

5.1 LoTSS DR2

This is the second data release (DR2) of the LOFAR survey LoTSS (Shimwell et al., 2022) covering 27% of the northern sky at 120−168 MHz. The DR2 coverage is split into two regions; the first region is centred at $12^{h}45^{m}$ (right ascension) and $+44°30'$ (declination) while the second region is centred at a right ascension of $1^{h}00^{m}$ and declination of $+28°00'$ spanning 4178 and 1457 deg^2 respectively. Shimwell et al. describes techniques that have resulted in the construction of a sample consisting of 4 396 228 extragalactic sources both of AGN and SFGs. The median sensitivity of DR2 is around 83 μJy beam^{-1} at 6 arcsec resolution (144 MHz).

5.1.1 LoTSS DR2 images and radio maps

Following the same analysis presented in Sec. 4.2 in the construction of a LOFAR sub-sample (55 objects) based on DR1, and recalling that these objects were selected on the basis of their compact nature in DR1, I present 5 RLAGN (and one extra source) objects from LoTSS DR2 which show extended radio emission in the LOFAR images. The remaining 50 objects are compact in DR2. The following is their discussion (refer to structures of interest marked by arrows in Fig. 5.1):

- **J1111+55** – this object is extended in both the VLA and in LoTSS DR2 images. LOFAR radio maps for this object show extended radio emission similar to the description given in Sec. 4.4.4.3 (also see Fig. 4.6). The projected physical size of the central structure in DR2 is estimated at ∼22 kpc.

- **J1151+53** – this object shows extended radio emission in DR2 images with what appears to be a decomposition between a bright unresolved radio core and a radio lobe in the north away from the central structure. The central structure in DR2 extends up to a projected maximum length of ∼15 kpc. However, this object is compact in the VLA images.

- **J1310+54** – the LOFAR contour maps for this object show faint and diffuse extended radio emission propagating symmetrically north and south from the radio core. The object shows extended radio emission in the VLA images (see Sec. 4.4.4.7 for a further discussion). The bright unresolved/slightly resolved central structure in DR2 is projected at ∼19 kpc in physical size.

- **J1310+51** – the object is clearly extended in LoTSS DR2 radio images. Interestingly, we can see two radio lobes on either side of the central structure measured at ∼58 kpc in linear size. However, the object was not included in the construction of the LOFAR sub-sample as its redshift ($z \sim 0.17$) is estimated to lie outside our redshift range ($0.03 < z < 0.1$). It was only included for the sole purpose of showcasing the brightness sensitivity of LoTSS DR2 as the object is compact in DR1.

- **J1433+52** – the source shows extended radio emission in DR2. LOFAR radio maps show a bright and unresolved radio core with what appears like a one-sided jet that tails slightly away from the radio core to the south-west direction. The projected physical size of the core is ∼10 kpc. The object is compact in the VLA images.

- **J1504+47** – the object is extended in LoTSS DR2 with what appears like a twin-sided jet. However, it is compact in the VLA images. The central structure extends up to ∼48 kpc in physical size.

The fact that some of the VLA compact objects show extended radio emission in LoTSS DR2 suggests that we may be underestimating the sizes for some of the populations of these sources. If this is the case, then we are likely missing a population of extended low-luminosity RLAGN which would occupy the lower-right side of the $P - D$ diagram (Fig. 4.10), limited by the surface brightness sensitivity of LOFAR. If discovered, these objects could add to our understanding of AGN feedback models.

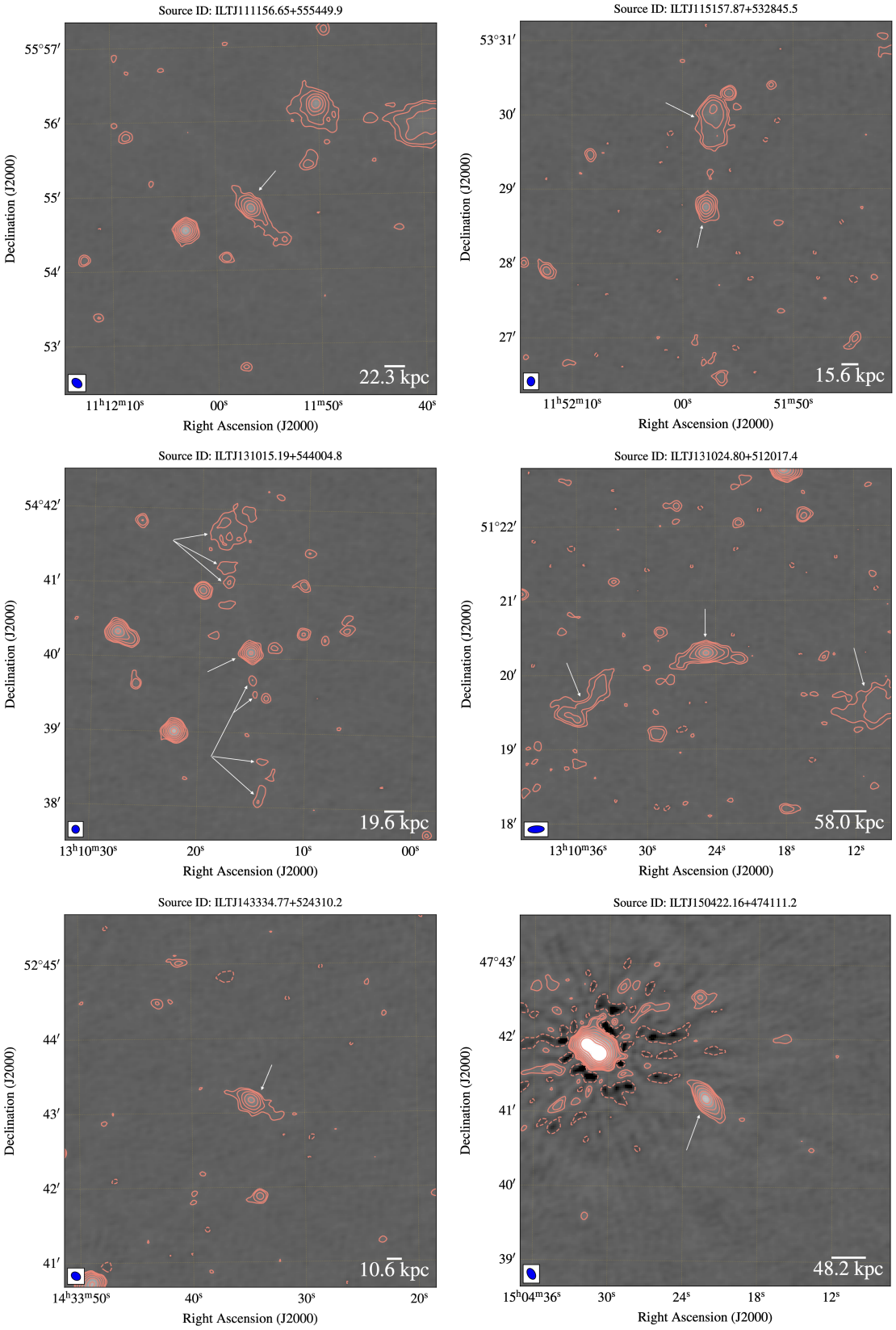

Figure 5.1: LoTSS DR2 images overlaid with 150 MHz radio contour maps in salmon. Contour levels are at [-3, 3, 5, 10, 20, 40,...,640]$\times\ \sigma_{\rm rms}$. Top two panels from left to right: $\sigma_{\rm rms} = 42.89$ and $41.90\ \mu$Jy respectively. Middle panels from left to right: $\sigma_{\rm rms} = 45.54$ and $76.54\ \mu$Jy respectively. Bottom panels from left to right: $\sigma_{\rm rms} = 46.57$ and $108.92\ \mu$Jy respectively. The RA and DEC covered by each object are shown on the axes. Solid lines represent positive contours (3σ) while dashed lines represent negative contours (-3σ). The LOFAR beam (blue ellipses) is displayed in the bottom left corner for each image. North is up and east is left. Note that the source ILTJ131024.80+512017.4 is not part of this paper's analysis as discussed in the text. The arrows on the images indicate structures that are of interest (associated with a jet). The measured sizes quoted in these images are for central structures only.

Chapter 6

Conclusion and Future Work

In the present Chapter, I summarise the main results of this work and I highlight possible future work.

6.1 Conclusion

I have presented high-resolution VLA 6 GHz observations of 55 low-luminosity ($L_{150} < 10^{25}$ W Hz^{-1}) RLAGN observed in the A-configuration. These objects were selected by Hardcastle et al. from a larger (23 344) LoTSS DR1 RLAGN sample. The objects were selected such that only those objects that showed as radiative efficient AGN on all the four AGN-SF separation techniques of Sabater et al. were picked. Then, their peak flux densities were limited to $S_{150\ \mathrm{MHz}} \geq 2$ mJy. Further, they restricted the selection of these sources within redshift range $0.03 < z < 0.1$. These procedures resulted in the 55 RLAGN presented in this thesis. These sources were selected on the basis of their compact nature in LoTSS DR1, though some objects (five) show extended radio emission in high-quality LoTSS DR2 images. Here I present a summary of our results and make necessary conclusions. The summary of this thesis is as follows:

1. I have found that only 9 out of 55 RLAGN show extended emission in the VLA images while 43 objects were found to be compact compared to the limiting angular resolution of 0.35 arcsec. This corresponds to $\sim$0.1$-$0.8 kpc in projected physical sizes. The extended objects have maximum sizes spanning 1$-$3 kpc and show a range of radio morphologies: doubles (3), two-sided jets (3), one-sided jets (2), and complex (1). No radio emissions were detected by the VLA for 3 objects.

2. The spectral index distribution ($-1.31 < \alpha < 0.36$) of these objects span the range seen in various compact RLAGN such as CSO, GPS, and CSS sources. 16 out of 55 objects have steep

radio spectra ($-1.31 < \alpha < -0.53$) which are consistent with standard models of optically thin synchrotron radio emission. 39 out of 55 objects showed flat/inverted radio spectra, a property that is prominent in self-absorbed synchrotron sources. I attribute the steepening in the radio spectra of these objects to be analogous to young rapidly growing CSS sources.

3. I have predicted physical sizes for 35 compact RLAGN with flat/inverted radio spectra, assuming SSA at 150 MHz, to be between $2-30$ mas in angular scales. This corresponds to $\sim 2-53$ pc in predicted physical sizes. The angular sizes are very well under LOFAR and the VLA resolution of 6 and 0.35 arcsec respectively. I have also estimated small $B-$fields ($0.3-0.7\,\mu$T) for these sources which correspond to young radio sources and are comparable to those estimated in CSS objects.

4. I have also shown that our RLAGN sample populate the bottom left side of the $P-D$ diagram ($P_{150} < 10^{25}$ W Hz^{-1}; D < 3 kpc), a position that is occupied by low-luminosity CSO sources. These sources in the $P-D$ space, therefore, do not occupy a special or unique position in comparison to other compact RLAGN such as CSOs, GPs, and CSSs. They are, however, expected to follow the evolutionary tracks represented by jet powers of Q $= 10^{35-37}$ W provided that other source and environmental conditions are met.

5. In total, 25 FR0s (Baldi et al., 2016, 2019) were observed with the VLA at different frequencies. These objects showed a range of radio properties that are similar to those of FRI sources lacking only in extended radio emission. Given that our RLAGN sample was selected from the local Universe as the FR0 sample, I have highlighted similarities in radio power, projected physical size, radio morphology, and radio spectra between FR0s and the sample presented in this work. However, the main difference between the two sources comes from the fact that our objects were selected on the basis that they are HERGs as opposed to the Baldi et al. FR0s which are predominantly selected as LERGs.

6. I also compared our HERG sample with the Pierce et al. HERG sample drawn from the local Universe ($z < 0.1$). Although both populations have similarly low radio-powers ($22.5 < \log(L_{1.4}) < 25.0$ W Hz^{-1}) and show similar maximum projected sizes ($0.28-0.54$ kpc), I find no similarities in their radio spectra; the K$-$S test ruled out the null hypothesis that our sources could be drawn from the same spectral index distribution with the Pierce et al. HERGs at a high confidence level.

In conclusion, the low-luminosity compact RLAGN selected from the LOFAR population can be associated with various classes of compact AGNs (e.g. CSO, GPS, CSS sources). The main result of this thesis is that a majority of these sources ($\sim$78%) remain unresolved and/or slightly resolved at high resolution with the VLA. All of these sources are highly core-dominated however, a small number of extended objects ($\sim$16%) show complex radio structures that can not be precisely classified. This supports the idea that these sources are injecting energies back into their local environments on sub-kpc scales and could play a crucial role in understanding SF and galaxy evolution (e.g. Ubertosi et al., 2021).

6.2 The future

In this thesis, I aimed to study the nature of 55 low-luminosity compact RLAGN selected from the LOFAR RLAGN population using their VLA high-resolution observations. Only 9 objects showed extended radio emission in the VLA images at 0.35 arcsec resolution while the remaining objects are compact.

Interestingly, there seems to be an emergence of flat/inverted radio spectra dominating from these sources at low frequencies. While I explored the effects of synchrotron self-absorption on these compact sources in this thesis, I have deferred (due to time constraints) the investigation of the effects of free-free absorption (FFA) on these compact sources to the near future and the results of which will be included in a paper (J. Chilufya et al. 2023) that is in preparation for publication in the Monthly Notices of the Royal Astronomical Society (MNRAS) journal.

Other future work includes proposing observation time (proposal in Prep.) for these compact sources to milliarcsec high-resolution long-baseline interferometers such as the eMERLIN[1], the VLBA[2], and/or the EVN[3] which should reveal a range of radio morphologies in a majority of these RLAGN on pc scales given that a few of these compact objects (J1213+50 and J1230+47) have been resolved with these interferometers (Cheng and An, 2018; Cheng et al., 2021; Baldi et al., 2021). As we have seen in Chapter 5, we may be underestimating the sizes for some of these objects and high resolution observations of these sources would help us understand the scales at which these sources affect the IGM of their host galaxies.

Detailed studies of RLAGN at both low and high luminosities, the local Universe, and out-to-high redshifts will be made possible by LOFAR sky surveys such as LoTSS whose capabilities to detect and resolve RLAGN in the radio sky is unrivalled. Other radio surveys with the Australian Square Kilometre Array Pathfinder (ASKAP; e.g. Hotan et al., 2021), the Karoo Array Telescope (MeerKAT; e.g. Jonas and MeerKAT Team, 2016), and in the future with the Square Kilometre Array (SKA; e.g. Dewdney et al., 2009) will provide radio data that will help us understand the amount of energy that is being injected in the IGM of the host galaxy by the jets of these low-luminosity radio-loud AGNs whose contribution to halting or slowing star formation and galaxy evolution is as yet poorly understood as the focus has been more in the study of the jets of powerful and extended FRI and FRII objects. Understanding the nature of such objects in the much larger LoTSS DR2 catalogue will be the focus of my future work.

[1] https://www.e-merlin.ac.uk/
[2] https://public.nrao.edu/telescopes/vlba/
[3] https://www.evlbi.org/

Bibliography

Afonso, J., Georgakakis, A., Almeida, C., et al., 2005. The Phoenix Deep Survey: Spectroscopic Catalog. *ApJ*, 624(1):135.

An, T. and Baan, W.A., 2012. The Dynamic Evolution of Young Extragalactic Radio Sources. *ApJ*, 760(1):77.

Antonucci, R., 1993. Unified models for active galactic nuclei and quasars. *Annual Review of Astronomy and Astrophysics*, 31:473.

Antonucci, R.R.J. and Miller, J.S., 1985. Spectropolarimetry and the nature of NGC 1068. *ApJ*, 297:621.

Antonucci, R.R.J. and Ulvestad, J.S., 1985. Extended radio emission and the nature of blazars. *ApJ*, 294:158.

Baldi, R.D. and Capetti, A., 2010. Spectro-photometric properties of the bulk of the radio-loud AGN population. *A&A*, 519:A48.

Baldi, R.D., Capetti, A., and Giovannini, G., 2015. Pilot study of the radio-emitting AGN population: the emerging new class of FR 0 radio-galaxies. *A&A*, 576:A38.

Baldi, R.D., Capetti, A., and Giovannini, G., 2016. The new class of FR 0 radio galaxies. *Astronomische Nachrichten*, 337(1-2):114.

Baldi, R.D., Capetti, A., and Giovannini, G., 2019. High-resolution VLA observations of FR0 radio galaxies: the properties and nature of compact radio sources. *MNRAS*, 482(2):2294.

Baldi, R.D., Capetti, A., and Massaro, F., 2018. FR0CAT: a FIRST catalog of FR 0 radio galaxies. *A&A*, 609:A1.

Baldi, R.D., Giovannini, G., and Capetti, A., 2021. The eMERLIN and EVN View of FR 0 Radio Galaxies. *Galaxies*, 9(4):106.

Baldi, R.D., Williams, D.R.A., McHardy, I.M., et al., 2018. LeMMINGs – I. The eMERLIN legacy survey of nearby galaxies. 1.5-GHz parsec-scale radio structures and cores. *Monthly Notices of the Royal Astronomical Society*, 476(3):3478.

Baldwin, J.A., Phillips, M.M., and Terlevich, R., 1981. Classification parameters for the emission-line spectra of extragalactic objects. *PASP*, 93:5.

Baldwin, J.E., 1982. Evolutionary tracks of extended radio sources. In D.S. Heeschen and C.M. Wade, editors, *Extragalactic Radio Sources*, volume 97, pages 21–24.

Barkana, R. and Loeb, A., 2007. The physics and early history of the intergalactic medium. *Reports on Progress in Physics*, 70(4):627.

Barthel, P.D., 1989. Is Every Quasar Beamed? *ApJ*, 336:606.

Becker, R.H., White, R.L., and Helfand, D.J., 1995. The FIRST Survey: Faint Images of the Radio Sky at Twenty Centimeters. *ApJ*, 450:559.

Beckmann, V. and Shrader, C., 2012. *Active Galactic Nuclei*. Physics textbook. Wiley.

Begelman, M.C., 1994. Thermal and Nonthermal Processes in Active Galactic Nuclei. In G.V. Bicknell, M.A. Dopita, and P.J. Quinn, editors, *The Physics of Active Galaxies*, volume 54 of *Astronomical Society of the Pacific Conference Series*, page 51.

Begelman, M.C., Blandford, R.D., and Rees, M.J., 1984. Theory of extragalactic radio sources. *Reviews of Modern Physics*, 56(2):255.

Best, P.N. and Heckman, T.M., 2012. On the fundamental dichotomy in the local radio-AGN population: accretion, evolution and host galaxy properties. *MNRAS*, 421(2):1569.

Best, P.N. and Heckman, T.M., 2012. On the fundamental dichotomy in the local radio-AGN population: accretion, evolution and host galaxy properties. *Monthly Notices of the Royal Astronomical Society*, 421(2):1569.

Best, P.N., Kaiser, C.R., Heckman, T.M., et al., 2006. AGN-controlled cooling in elliptical galaxies. *MNRAS*, 368(1):L67.

Best, P.N., Kauffmann, G., Heckman, T.M., et al., 2005a. A sample of radio-loud active galactic nuclei in the Sloan Digital Sky Survey. *MNRAS*, 362(1):9.

Best, P.N., Kauffmann, G., Heckman, T.M., et al., 2005b. The host galaxies of radio-loud active galactic nuclei: mass dependences, gas cooling and active galactic nuclei feedback. *MNRAS*, 362(1):25.

Best, P.N., Ker, L.M., Simpson, C., et al., 2014. The cosmic evolution of radio-AGN feedback to z = 1. *Monthly Notices of the Royal Astronomical Society*, 445(1):955.

Beuchert, T., 2017. *Multiwavelength observations of Active Galactic Nuclei from the radio to the hard X-rays*. Ph.D. thesis, University of Erlangen-Nuremberg, Astronomical Institute.

Bharadwaj, V., Reiprich, T.H., Schellenberger, G., et al., 2014. Intracluster medium cooling, AGN feedback, and brightest cluster galaxy properties of galaxy groups. Five properties where groups differ from clusters. *A&A*, 572:A46.

Bicknell, G.V., 1995. Relativistic Jets and the Fanaroff-Riley Classification of Radio Galaxies. *ApJ*, 101:29.

Bicknell, G.V., Dopita, M.A., and O'Dea, C.P.O., 1997. Unification of the Radio and Optical Properties of Gigahertz Peak Spectrum and Compact Steep-Spectrum Radio Sources. *ApJ*, 485(1):112.

Bicknell, G.V., Mukherjee, D., Wagner, A.Y., et al., 2018. Relativistic jet feedback – II. Relationship to gigahertz peak spectrum and compact steep spectrum radio galaxies. *Monthly Notices of the Royal Astronomical Society*, 475(3):3493.

Blandford, R., Meier, D., and Readhead, A., 2019. Relativistic jets from active galactic nuclei. *Annual Review of Astronomy and Astrophysics*, 57(1):467.

Blandford, R.D. and Narayan, R., 1992. Cosmological applications of gravitational lensing. *Annual Review of Astronomy and Astrophysics*, 30:311.

Blandford, R.D. and Payne, D.G., 1982. Hydromagnetic flows from accretion disks and the production of radio jets. *MNRAS*, 199:883.

Blandford, R.D. and Rees, M.J., 1974. A "twin-exhaust" model for double radio sources. *MNRAS*, 169:395.

Blundell, K.M., Rawlings, S., and Willott, C.J., 1999. The nature and evolution of classical double radio sources from complete samples. *The Astronomical Journal*, 117(2):677.

Boller, T., 2000. Rosat results on narrow-line seyfert 1 galaxies. *New Astronomy Reviews*, 44(7-9):387.

Boller, T., Brandt, W.N., and Fink, H., 1996. Soft X-ray properties of narrow-line Seyfert 1 galaxies. *A&A*, 305:53.

Bondi, M., Marchã, M., Dallacasa, D., et al., 2001. Intermediate BL Lac objects. *Monthly Notices of the Royal Astronomical Society*, 325(3):1109.

Bosch-Ramon, V., 2018. The role of AGN jets in the reionization epoch. *A&A*, 617:L3.

Brandt, W.N. and Alexander, D.M., 2010. Supermassive black-hole growth over cosmic time: Active galaxy demography, physics, and ecology from Chandra surveys. *Proceedings of the National Academy of Science*, 107:7184.

Brandt, W.N., Mathur, S., and Elvis, M., 1997. A comparison of the hard ASCA spectral slopes of broad- and narrow-line Seyfert 1 galaxies. *Monthly Notices of the Royal Astronomical Society*, 285(3):L25.

Bridle, A.H. and Perley, R.A., 1984. Extragalactic Radio Jets. *Annual Review of Astronomy and Astrophysics*, 22:319.

Briggs, D.S., 1995. High Fidelity Interferometric Imaging: Robust Weighting and NNLS Deconvolution. In *American Astronomical Society Meeting Abstracts*, volume 187 of *American Astronomical Society Meeting Abstracts*, page 112.02.

Brinchmann, J., Charlot, S., White, S.D.M., et al., 2004. The physical properties of star-forming galaxies in the low-redshift Universe. *MNRAS*, 351(4):1151.

Burbidge, G.R., 1956. On Synchrotron Radiation from Messier 87. *ApJ*, 124:416.

Capetti, A., Brienza, M., Baldi, R.D., et al., 2020. The LOFAR view of FR 0 radio galaxies. *A&A*, 642:A107.

Celotti, A. and Fabian, A.C., 1993. The kinetic power and luminosity of parsec-scale radio jets – an argument for heavy jets. *Monthly Notices of the Royal Astronomical Society*, 264(1):228.

Chambers, K.C., Magnier, E.A., Metcalfe, N., et al., 2016. The Pan-STARRS1 Surveys. *arXiv e-prints*, arXiv:1612.05560.

Chen, Y.Y., Zhang, X., Zhang, H.J., et al., 2015. Core-dominance parameter, black hole mass and jet-disc connection for Fermi blazars. *Monthly Notices of the Royal Astronomical Society*, 451(4):4193.

Cheng, X., An, T., Sohn, B.W., et al., 2021. Parsec-scale properties of eight Fanaroff-Riley type 0 radio galaxies. *MNRAS*, 506(2):1609.

Cheng, X.P. and An, T., 2018. Parsec-scale Radio Structure of 14 Fanaroff-Riley Type 0 Radio Galaxies. *ApJ*, 863(2):155.

Chiaberge, M., Macchetto, F.D., Sparks, W.B., et al., 2002. The Nuclei of Radio Galaxies in the Ultraviolet: The Signature of Different Emission Processes. *ApJ*, 571(1):247.

Clark, B.G., 1980. An efficient implementation of the algorithm 'CLEAN'. *A&A*, 89(3):377.

Condon, J.J., 1984. Cosmological evolution of radio sources. *ApJ*, 287:461.

Condon, J.J., 1992. Radio emission from normal galaxies. *Annual Review of Astronomy and Astrophysics*, 30:575.

Condon, J.J., 1999. Very Large Radio Surveys of the Sky. *Proceedings of the National Academy of Science*, 96(9):4756.

Condon, J.J., Cotton, W.D., Greisen, E.W., et al., 1998. The NRAO VLA sky survey. *The Astronomical Journal*, 115(5):1693.

Cornwell, T.J., 2008. Multiscale clean deconvolution of radio synthesis images. *IEEE Journal of selected topics in signal processing*, 2(5):793.

Croton, D.J., Springel, V., White, S.D.M., et al., 2006. The many lives of active galactic nuclei: cooling flows, black holes and the luminosities and colours of galaxies. *MNRAS*, 365(1):11.

Curtis, H.D., 1918. Descriptions of 762 Nebulae and Clusters Photographed with the Crossley Reflector. *Publications of Lick Observatory*, 13:9.

Dallacasa, D., Tinti, S., Fanti, C., et al., 2002. The B3-VLA CSS sample. II. VLBA images at 18 cm. *A&A*, 389:115.

Davies, J.G., Anderson, B., and Morison, I., 1980. The Jodrell Bank radio-linked interferometer network. *Nature*, 288(5786):64.

de Gasperin, F., Intema, H.T., and Frail, D.A., 2018. A radio spectral index map and catalogue at 147-1400 MHz covering 80 per cent of the sky. *MNRAS*, 474(4):5008.

Delhaize, J., Heywood, I., Prescott, M., et al., 2021. MIGHTEE: are giant radio galaxies more common than we thought? *MNRAS*, 501(3):3833.

Dewdney, P.E., Hall, P.J., Schilizzi, R.T., et al., 2009. The square kilometre array. *Proceedings of the IEEE*, 97(8):1482.

Di Matteo, T., Allen, S.W., Fabian, A.C., et al., 2003. Accretion onto the Supermassive Black Hole in M87. *ApJ*, 582(1):133.

Di Matteo, T., Springel, V., and Hernquist, L., 2005. Energy input from quasars regulates the growth and activity of black holes and their host galaxies. *Nature*, 433(7026):604.

Doi, A., Nagira, H., Kawakatu, N., et al., 2012. KILOPARSEC-SCALE RADIO STRUCTURES IN NARROW-LINE SEYFERT 1 GALAXIES. *The Astrophysical Journal*, 760(1):41.

Duncan, K.J., Sabater, J., Röttgering, H.J.A., et al., 2019. The LOFAR Two-metre Sky Survey. IV. First Data Release: Photometric redshifts and rest-frame magnitudes. *A&A*, 622:A3.

Fabian, A.C., 2012. Observational Evidence of Active Galactic Nuclei Feedback. *Annual Review of Astronomy and Astrophysics*, 50:455.

Fan, X., Strauss, M.A., Becker, R.H., et al., 2006. Constraining the Evolution of the Ionizing Background and the Epoch of Reionization with z$\sim$6 Quasars. II. A Sample of 19 Quasars. *AJ*, 132(1):117.

Fanaroff, B.L. and Riley, J.M., 1974. The morphology of extragalactic radio sources of high and low luminosity. *MNRAS*, 167:31P.

Fanidakis, N., Baugh, C.M., Benson, A.J., et al., 2011. Grand unification of AGN activity in the ΛCDM cosmology. *MNRAS*, 410(1):53.

Fanti, R., Fanti, C., Schilizzi, R.T., et al., 1990. On the nature of compact steep spectrum radio sources. *A&A*, 231:333.

Gallimore, J.F., Axon, D.J., O'Dea, C.P., et al., 2006. A Survey of Kiloparsec-Scale Radio Outflows in Radio-Quiet Active Galactic Nuclei. *AJ*, 132(2):546.

Gallimore, J.F., Axon, D.J., O'Dea, C.P., et al., 2006. A survey of kiloparsec-scale radio outflows in radio-quiet active galactic nuclei. *The Astronomical Journal*, 132(2):546.

Garofalo, D., Evans, D.A., and Sambruna, R.M., 2010. The evolution of radio-loud active galactic nuclei as a function of black hole spin. *MNRAS*, 406(2):975.

Gaur, H., Gupta, A.C., Strigachev, A., et al., 2012. Optical flux and spectral variability of blazars. *Monthly Notices of the Royal Astronomical Society*, 425(4):3002.

Gawroński, M.P., Marecki, A., Kunert-Bajraszewska, M., et al., 2006. Hybrid morphology radio sources from the FIRST survey. *A&A*, 447(1):63.

Gebhardt, K., Mentuch Cooper, E., Ciardullo, R., et al., 2021. The Hobby-Eberly Telescope Dark Energy Experiment (HETDEX) Survey Design, Reductions, and Detections. *ApJ*, 923(2):217.

Ghisellini, G. and Celotti, A., 2001. The dividing line between FR I and FR II radio-galaxies. *A&A*, 379:L1.

Ghisellini, G., Padovani, P., Celotti, A., et al., 1993. Relativistic Bulk Motion in Active Galactic Nuclei. *ApJ*, 407:65.

Giovannini, G., Taylor, G.B., Cotton, W.D., et al., 2002. Intrinsic Properties of High and Low Power Radio Sources and Unified Scheme Models. In R. Maiolino, A. Marconi, and N. Nagar, editors, *Issues in Unification of Active Galactic Nuclei*, volume 258 of *Astronomical Society of the Pacific Conference Series*, page 285.

Giroletti, M., Giovannini, G., Taylor, G.B., et al., 2004. A Sample of Low-Redshift BL Lacertae Objects. I. The Radio Data. *ApJ*, 613(2):752.

Godfrey, L.E.H., Morganti, R., and Brienza, M., 2017. On the population of remnant Fanaroff-Riley type II radio galaxies and implications for radio source dynamics. *MNRAS*, 471(1):891.

González-Martín, O., Masegosa, J., Márquez, I., et al., 2006. X-ray nature of the LINER nuclear sources. *A&A*, 460(1):45.

Gopal-Krishna, Goyal, A., Joshi, S., et al., 2011. Rapid optical variability of TeV blazars. *Monthly Notices of the Royal Astronomical Society*, 416(1):101.

Gopal-Krishna and Wiita, P.J., 2000. Extragalactic radio sources with hybrid morphology: implications for the Fanaroff-Riley dichotomy. *A&A*, 363:507.

Gorchtein, M., Profumo, S., and Ubaldi, L., 2010. Probing dark matter with active galactic nuclei jets. *Phys. Rev. D*, 82:083514.

Grier, C.J., Pancoast, A., Barth, A.J., et al., 2017. The structure of the broad-line region in active galactic nuclei. ii. dynamical modeling of data from the agn10 reverberation mapping campaign. *The Astrophysical Journal*, 849(2):146.

Gürkan, G., Hardcastle, M.J., Smith, D.J.B., et al., 2018. LOFAR/H-ATLAS: the low-frequency radio luminosity-star formation rate relation. *MNRAS*, 475(3):3010.

Hardcastle, M., 2018a. Interpreting radiative efficiency in radio-loud AGNs. *Nature Astronomy*, 2:273.

Hardcastle, M.J., 2004. B_{gg} revisited: The environments of low-excitation radio galaxies and unified models. *A&A*, 414:927.

Hardcastle, M.J., 2018b. A simulation-based analytic model of radio galaxies. *MNRAS*, 475(2):2768.

Hardcastle, M.J., Alexander, P., Pooley, G.G., et al., 1998a. FRII radio galaxies with z<0.3 - I. Properties of jets, cores and hotspots. *MNRAS*, 296(2):445.

Hardcastle, M.J., Birkinshaw, M., and Worrall, D.M., 1998b. Magnetic field strengths in the hotspots of 3C 33 and 111. *MNRAS*, 294:615.

Hardcastle, M.J. and Croston, J.H., 2020. Radio galaxies and feedback from AGN jets. *New Astronomy Review*, 88:101539.

Hardcastle, M.J., Evans, D., and Croston, J.H., 2009. The active nuclei of z < 1.0 3crr radio sources. *Monthly Notices of the Royal Astronomical Society*, 396:1929.

Hardcastle, M.J., Evans, D.A., and Croston, J.H., 2006. The X-ray nuclei of intermediate-redshift radio sources. *MNRAS*, 370(4):1893.

Hardcastle, M.J., Evans, D.A., and Croston, J.H., 2007. Hot and cold gas accretion and feedback in radio-loud active galaxies. *MNRAS*, 376(4):1849.

Hardcastle, M.J., Gürkan, G., van Weeren, R.J., et al., 2016. LOFAR/H-ATLAS: a deep low-frequency survey of the Herschel-ATLAS North Galactic Pole field. *MNRAS*, 462(2):1910.

Hardcastle, M.J., Harris, D.E., Worrall, D.M., et al., 2004. The Origins of X-Ray Emission from the Hot Spots of FR II Radio Sources. *ApJ*, 612(2):729.

Hardcastle, M.J. and Krause, M.G.H., 2013. Numerical modelling of the lobes of radio galaxies in cluster environments. *MNRAS*, 430(1):174.

Hardcastle, M.J., Williams, W.L., Best, P.N., et al., 2019. Radio-loud AGN in the first LoTSS data release. The lifetimes and environmental impact of jet-driven sources. *A&A*, 622:A12.

Hardcastle, M.J. and Worrall, D.M., 2000. The environments of FRII radio sources. *MNRAS*, 319(2):562.

Harrison, C.M., 2017. Impact of supermassive black hole growth on star formation. *Nature Astronomy*, 1:0165.

Hassan, S., Davé, R., Mitra, S., et al., 2017. Constraining the contribution of active galactic nuclei to reionization. *Monthly Notices of the Royal Astronomical Society*, 473(1):227.

Heckman, T.M., 1980. An Optical and Radio Survey of the Nuclei of Bright Galaxies - Activity in the Normal Galactic Nuclei. *A&A*, 87:152.

Heckman, T.M. and Best, P.N., 2014. The Coevolution of Galaxies and Supermassive Black Holes: Insights from Surveys of the Contemporary Universe. *Annual Review of Astronomy and Astrophysics*, 52:589.

Hill, G.J. and Lilly, S.J., 1991. A Change in the Cluster Environments of Radio Galaxies with Cosmic Epoch. *ApJ*, 367:1.

Hine, R.G. and Longair, M.S., 1979. Optical spectra of 3CR radio galaxies. *MNRAS*, 188:111.

Ho, L.C., 2008. Nuclear activity in nearby galaxies. *Annual Review of Astronomy and Astrophysics*, 46:475.

Ho, L.C., Filippenko, A.V., and Sargent, W.L.W., 1997. A Search for "Dwarf" Seyfert Nuclei. III. Spectroscopic Parameters and Properties of the Host Galaxies. *ApJ*, 112(2):315.

Högbom, J.A., 1974. Aperture Synthesis with a Non-Regular Distribution of Interferometer Baselines. *A&A Supp.*, 15:417.

Hotan, A.W., Bunton, J.D., Chippendale, A.P., et al., 2021. Australian square kilometre array pathfinder: I. system description. *Publications of the Astron. Soc. of Australia*, 38:e009.

Huynh, M.T., Jackson, C.A., and Norris, R.P., 2007. Radio observations of the hubble deep field-south region. III. the 2.5, 5.2, and 8.7 GHz catalogs and radio source properties. *The Astronomical Journal*, 133(4):1331.

Ibar, E., Ivison, R.J., Biggs, A.D., et al., 2009. Deep multi-frequency radio imaging in the Lockman Hole using the GMRT and VLA - I. The nature of the sub-mJy radio population. *MNRAS*, 397(1):281.

Jansky, K.G., 1933. Radio Waves from Outside the Solar System. *Nature*, 132(3323):66.

Jarvis, M., Taylor, R., Agudo, I., et al., 2016. The MeerKAT International GHz Tiered Extragalactic Exploration (MIGHTEE) Survey. In *MeerKAT Science: On the Pathway to the SKA*, page 6.

Jarvis, M.E., Harrison, C.M., Thomson, A.P., et al., 2019. Prevalence of radio jets associated with galactic outflows and feedback from quasars. *MNRAS*, 485(2):2710.

Jonas, J. and MeerKAT Team, 2016. The MeerKAT Radio Telescope. In *MeerKAT Science: On the Pathway to the SKA*, page 1.

Kaiser, C.R. and Alexander, P., 1997. A self-similar model for extragalactic radio sources. *MNRAS*, 286(1):215.

Kaiser, N., Aussel, H., Burke, B.E., et al., 2002. Pan-STARRS: A Large Synoptic Survey Telescope Array. In J.A. Tyson and S. Wolff, editors, *Survey and Other Telescope Technologies and Discoveries*, volume 4836 of *Society of Photo-Optical Instrumentation Engineers (SPIE) Conference Series*, pages 154–164.

Kakiichi, K., Ellis, R.S., Laporte, N., et al., 2018. The role of galaxies and AGN in reionizing the IGM - I. Keck spectroscopy of 5 < z < 7 galaxies in the QSO field J1148+5251. *MNRAS*, 479(1):43.

Kauffmann, G., Heckman, T.M., and Best, P.N., 2008. Radio jets in galaxies with actively accreting black holes: new insights from the SDSS. *MNRAS*, 384(3):953.

Kellermann, K.I., 1964. The Spectra of Non-Thermal Radio Sources. *ApJ*, 140:969.

Kellermann, K.I., 1966. The radio source 1934-63. *Australian Journal of Physics*, 19:195.

Kellermann, K.I., Condon, J.J., Kimball, A.E., et al., 2016. Radio-loud and Radio-quiet QSOs. *ApJ*, 831(2):168.

Kellermann, K.I. and Moran, J.M., 2001. The development of high-resolution imaging in radio astronomy. *Annual Review of Astronomy and Astrophysics*, 39(1):457.

Kellermann, K.I., Sramek, R., Schmidt, M., et al., 1989. VLA Observations of Objects in the Palomar Bright Quasar Survey. *AJ*, 98:1195.

Kellermann, K.I., Sramek, R.A., Schmidt, M., et al., 1994. The Radio Structure of Radio Loud and Quiet Quasars in the Palomar Bright Quasar Survey. *AJ*, 108:1163.

Khachikian, E.Y. and Weedman, D.W., 1974. An atlas of Seyfert galaxies. *ApJ*, 192:581.

Kharb, P., Lister, M.L., and Cooper, N.J., 2010. Extended Radio Emission in MOJAVE Blazars: Challenges to Unification. *ApJ*, 710(1):764.

Kim, S.H., Lee, S.S., Lee, J.W., et al., 2022. Magnetic field strengths of the synchrotron self-absorption region in the jet of CTA 102 during radio flares. *MNRAS*, 510(1):815.

Klamer, I.J., Ekers, R.D., Bryant, J.J., et al., 2006. A search for distant radio galaxies from SUMSS and NVSS - III. Radio spectral energy distributions and the z-α correlation. *MNRAS*, 371(2):852.

Komossa, S., Voges, W., Xu, D., et al., 2006. Radio-loud Narrow-Line Type 1 Quasars. *AJ*, 132(2):531.

Krolik, J.H., 1999. *Active galactic nuclei: from the central black hole to the galactic environment*, volume 60. Princeton University Press.

Krolik, J.H. and Begelman, M.C., 1986. An X-ray heated wind in NGC 1068. *ApJ*, 308:L55.

Krolik, J.H. and Di Matteo, T., 2000. Active Galactic Nuclei: From the Central Black Hole to the Galactic Environment. *American Journal of Physics*, 68(5):489.

Kunert-Bajraszewska, M., Gawroński, M.P., Labiano, A., et al., 2010. A survey of low-luminosity compact sources and its implication for the evolution of radio-loud active galactic nuclei - I. Radio data. *MNRAS*, 408(4):2261.

Kunert-Bajraszewska, M. and Labiano, A., 2010. A survey of low-luminosity compact sources and its implication for the evolution of radio-loud active galactic nuclei - II. Optical analysis. *MNRAS*, 408(4):2279.

Laing, R.A., 1994. Decelerating Relativistic Jets in FRI Radio Sources. In G.V. Bicknell, M.A. Dopita, and P.J. Quinn, editors, *The Physics of Active Galaxies*, volume 54 of *Astronomical Society of the Pacific Conference Series*, page 227.

Laing, R.A., Jenkins, C.R., Wall, J.V., et al., 1994. Spectrophotometry of a Complete Sample of 3CR Radio Sources: Implications for Unified Models. In G.V. Bicknell, M.A. Dopita, and P.J. Quinn, editors, *The Physics of Active Galaxies*, volume 54 of *Astronomical Society of the Pacific Conference Series*, page 201.

Lawrence, A., 1987. Classification of active galaxies and the prospect of a unified phenomenology. *PASP*, 99:309.

Leahy, J.P. and Williams, A.G., 1984. The bridges of classical double radio sources. *MNRAS*, 210:929.

Liang, E.W. and Liu, H.T., 2003. The masses of central supermassive black holes and the variability time-scales in gamma-ray loud blazars. *Monthly Notices of the Royal Astronomical Society*, 340(2):632.

Lin, Y.T., Ostriker, J.P., and Miller, C.J., 2010. A New Test of the Statistical Nature of the Brightest Cluster Galaxies. *ApJ*, 715(2):1486.

Longair, M., 2011. *High Energy Astrophysics*. Cambridge University Press.

Machalski, J. and Condon, J.J., 1999. Radio Emission from Galaxies in the Las Campanas Redshift Survey. *ApJ*, 123(1):41.

Machalski, J., Kozieł-Wierzbowska, D., Jamrozy, M., et al., 2008. J1420-0545: The Radio Galaxy Larger than 3C 236. *ApJ*, 679(1):149.

MacLeod, J.M. and Andrew, B.H., 1968. The Radio Source VRO 42.22.01. *Astrophysics Letters*, 1:243.

Magliocchetti, M., Maddox, S.J., Wall, J.V., et al., 2000. The redshift distribution of FIRST radio sources at 1mJy. *MNRAS*, 318(4):1047.

Malkan, M.A., Jensen, L.D., Rodriguez, D.R., et al., 2017. Emission line properties of seyfert galaxies in the 12 μm sample. *The Astrophysical Journal*, 846(2):102.

Malkan, M.A. and Sargent, W.L.W., 1982. The ultraviolet excess of Seyfert 1 galaxies and quasars. *ApJ*, 254:22.

Maraschi, L. and Rovetti, F., 1994. A Unified Relativistic Beaming Model for BL Lacertae Objects and Flat Spectrum Radio Quasars. *ApJ*, 436:79.

Marchesini, D., Celotti, A., and Ferrarese, L., 2004. A transition in the accretion properties of radio-loud active nuclei. *Monthly Notices of the Royal Astronomical Society*, 351(2):733.

Markowitz, A.G., Krumpe, M., and Nikutta, R., 2014. First X-ray-based statistical tests for clumpy-torus models: eclipse events from 230 years of monitoring of Seyfert AGN. *Monthly Notices of the Royal Astronomical Society*, 439(2):1403.

Mathur, S., 2000. Narrow-line Seyfert 1 galaxies and the evolution of galaxies and active galaxies. *Monthly Notices of the Royal Astronomical Society*, 314(4):L17.

Mazoochi, F., Miraghaei, H., and Riazi, N., 2022. The relation between the radio emission of the core and host galaxy properties in fanaroff–riley type ii radio galaxies. *Publications of the Astronomical Society of Australia*, 39:e021.

McMullin, J.P., Waters, B., Schiebel, D., et al., 2007. CASA Architecture and Applications. In R.A. Shaw, F. Hill, and D.J. Bell, editors, *Astronomical Data Analysis Software and Systems XVI*, volume 376 of *Astronomical Society of the Pacific Conference Series*, page 127.

Meier, D., 2012. *Black Hole Astrophysics: The Engine Paradigm*. Springer Praxis Books. Springer Berlin Heidelberg.

Meier, D.L., 1999. A magnetically switched, rotating black hole model for the production of extragalactic radio jets and the fanaroff and riley class division. *The Astrophysical Journal*, 522(2):753.

Meier, D.L., 2002. Grand unification of agn and the accretion and spin paradigms. *New Astronomy Reviews*, 46(2-7):247.

Mingo, B., Croston, J.H., Hardcastle, M.J., et al., 2019. Revisiting the Fanaroff–Riley dichotomy and radio-galaxy morphology with the LOFAR Two-Metre Sky Survey (LoTSS). *Monthly Notices of the Royal Astronomical Society*, 488(2):2701.

Mingo, B., Hardcastle, M.J., Croston, J.H., et al., 2014. An X-ray survey of the 2 Jy sample – I. Is there an accretion mode dichotomy in radio-loud AGN? *Monthly Notices of the Royal Astronomical Society*, 440(1):269.

Miraghaei, H. and Best, P.N., 2017. The nuclear properties and extended morphologies of powerful radio galaxies: the roles of host galaxy and environment. *MNRAS*, 466(4):4346.

Morabito, L.K. and Harwood, J.J., 2018. Investigating the cause of the α–z relation. *Monthly Notices of the Royal Astronomical Society*, 480(2):2726.

Morganti, R., Oosterloo, T.A., Tadhunter, C.N., et al., 2005a. The location of the broad H i absorption in 3C 305: clear evidence for a jet-accelerated neutral outflow. *A&A*, 439(2):521.

Morganti, R., Tadhunter, C.N., and Oosterloo, T.A., 2005b. Fast neutral outflows in powerful radio galaxies: a major source of feedback in massive galaxies. *A&A*, 444(1):L9.

Mushotzky, R.F., 1982. The X-ray spectrum and time variability of narrow emission line galaxies. *ApJ*, 256:92.

Napier, P.J., 1994. The very long baseline array. In J.G. Robertson and W.J. Tango, editors, *Very High Angular Resolution Imaging*, pages 117–124. Springer Netherlands, Dordrecht.

Narayan, R. and Yi, I., 1994. Advection-dominated Accretion: A Self-similar Solution. *ApJ*, 428:L13.

Neeser, M.J., Eales, S.A., Law-Green, J.D., et al., 1995. The Linear-Size Evolution of Classical Double Radio Sources. *ApJ*, 451:76.

Nelson, C.H., MacKenty, J.W., Simkin, S.M., et al., 1996. Seyfert Galaxies. IV. Nuclear Profiles of Markarian Seyfert Galaxies from Hubble Space Telescope Images. *ApJ*, 466:713.

Nenkova, M., Sirocky, M.M., Nikutta, R., et al., 2008. AGN Dusty Tori. II. Observational Implications of Clumpiness. *ApJ*, 685(1):160.

Northover, K.J.E., 1973. The radio galaxy 3C 66. *MNRAS*, 165:369.

O'Dea, C.P., 1998. The Compact Steep-Spectrum and Gigahertz Peaked-Spectrum Radio Sources. *PASP*, 110(747):493.

O'Dea, C.P. and Baum, S.A., 1997. Constraints on Radio Source Evolution from the Compact Steep Spectrum and GHz Peaked Spectrum Radio Sources. *AJ*, 113:148.

O'Dea, C.P., Baum, S.A., and Stanghellini, C., 1991. What Are the Gigahertz Peaked-Spectrum Radio Sources? *ApJ*, 380:66.

O'Dea, C.P., Baum, S.A., Stanghellini, C., et al., 1990. Multifrequency VLA observations of GHz-peaked-spectrum radio cores. *A&A Supp.*, 84:549.

O'Dea, C.P. and Saikia, D.J., 2021. Compact steep-spectrum and peaked-spectrum radio sources. *Astronomy and Astrophysics Reviews*, 29(1):3.

Oemler, A., J., 1979. Space Telescope observations of normal galaxies. In *NASA Conference Publication*, volume 2111 of *NASA Conference Publication*, pages 165–180.

Oke, J.B. and Gunn, J.E., 1974. The Distance of BL Lacertae. *ApJ*, 189:L5.

Orienti, M. and Dallacasa, D., 2008. Are young radio sources in equipartition? *A&A*, 487(3):885.

Osterbrock, D. and Ferland, G., 2006. *Astrophysics Of Gas Nebulae and Active Galactic Nuclei*. University Science Books.

Osterbrock, D.E. and Pogge, R.W., 1985. The spectra of narrow-line Seyfert 1 galaxies. *ApJ*, 297:166.

Pacholczyk, A.G., 1970. *Radio astrophysics. Nonthermal processes in galactic and extragalactic sources*. San Francisco: W. H. Freeman.

Padovani, P., 2016. The faint radio sky: radio astronomy becomes mainstream. *Astronomy and Astrophysics Reviews*, 24(1):13.

Padovani, P. and Giommi, P., 1995. A sample-oriented catalogue of BL Lacertae objects. *MNRAS*, 277:1477.

Panessa, F., Baldi, R.D., Laor, A., et al., 2019. The origin of radio emission from radio-quiet active galactic nuclei. *Nature Astronomy*, 3:387.

Patil, P., Whittle, M., Nyland, K., et al., 2022. Radio Spectra of Luminous, Heavily Obscured WISE-NVSS Selected Quasars. *ApJ*, 934(1):26.

Peirani, S., Dubois, Y., Volonteri, M., et al., 2017. Density profile of dark matter haloes and galaxies in the horizon–agn simulation: the impact of AGN feedback. *Monthly Notices of the Royal Astronomical Society*, 472(2):2153.

Perley, R.A. and Butler, B.J., 2017. An accurate flux density scale from 50 MHz to 50 GHz. *The Astrophysical Journal Supplement Series*, 230(1):7.

Perley, R.A., Dreher, J.W., and Cowan, J.J., 1984. The jet and filaments in Cygnus A. *ApJ*, 285:L35.

Peterson, B.M., 1997. *An introduction to active galactic nuclei*. Cambridge University Press.

Peterson, B.M., 2015. Measuring the Masses of Supermassive Black Holes. In M. Falanga, T. Belloni, P. Casella, M. Gilfanov, P. Jonker, and A. King, editors, *The Physics of Accretion onto Black Holes*, volume 49, pages 253–275.

Pierce, J.C.S., Tadhunter, C.N., and Morganti, R., 2020. The radio properties of high-excitation radio galaxies with intermediate radio powers. *MNRAS*, 494(2):2053.

Pierce, J.C.S., Tadhunter, C.N., Ramos Almeida, C., et al., 2019. Do AGN triggering mechanisms vary with radio power? - I. Optical morphologies of radio-intermediate HERGs. *MNRAS*, 487(4):5490.

Prandoni, I., Parma, P., Wieringa, M.H., et al., 2006. The ATESP 5 GHz radio survey. I. Source counts and spectral index properties of the faint radio population. *A&A*, 457(2):517.

Randall, K.E., Hopkins, A.M., Norris, R.P., et al., 2012. Spectral index properties of milliJansky radio sources. *Monthly Notices of the Royal Astronomical Society*, 421(2):1644.

Rani, B., Krichbaum, T.P., Fuhrmann, L., et al., 2013. Radio to gamma-ray variability study of blazar S5 0716+714. *A&A*, 552:A11.

Richardson, M.L.A., Scannapieco, E., Devriendt, J., et al., 2016. Comparing Simulations of AGN Feedback. *ApJ*, 825(2):83.

Rigby, E.E., Best, P.N., Brookes, M.H., et al., 2011. The luminosity-dependent high-redshift turnover in the steep spectrum radio luminosity function: clear evidence for downsizing in the radio-AGN population. *MNRAS*, 416(3):1900.

Ros, E. and Pérez-Torres, M.Á., 2012. VLBI imaging of M 81* at 43 GHz. *A&A*, 537:A93.

Rowan-Robinson, M., 1977. On the unity of activity in galaxies. *ApJ*, 213:635.

Ryle, M., 1952. A New Radio Interferometer and Its Application to the Observation of Weak Radio Stars. *Proceedings of the Royal Society of London Series A*, 211(1106):351.

Sabater, J., Best, P.N., and Hardcastle, M.J., 2019. The LoTSS view of radio AGN in the local Universe. The most massive galaxies are always switched on. *A&A*, 622:A17.

Sadler, E.M., Ekers, R.D., Mahony, E.K., et al., 2014. The local radio-galaxy population at 20 GHz. *MNRAS*, 438(1):796.

Scheuer, P.A.G. and Readhead, A.C.S., 1979. Superluminally expanding radio sources and the radio-quiet QSOs. *Nature*, 277:182.

Schilizzi, R.T., 1995. EVN and Global VLBI. In J.A. Zensus, P.J. Diamond, and P.J. Napier, editors, *Very Long Baseline Interferometry and the VLBA*, volume 82 of *Astronomical Society of the Pacific Conference Series*, page 397.

Schmidt, M., 1963. 3C 273 : A Star-Like Object with Large Red-Shift. *Nature*, 197(4872):1040.

Schmidt, M., 1968. Space Distribution and Luminosity Functions of Quasi-Stellar Radio Sources. *ApJ*, 151:393.

Schmidt, M. and Green, R.F., 1983. Quasar evolution derived from the Palomar bright quasar survey and other complete quasar surveys. *ApJ*, 269:352.

Seyfert, C.K., 1943. Nuclear Emission in Spiral Nebulae. *ApJ*, 97:28.

Shimwell, T.W., Hardcastle, M.J., Tasse, C., et al., 2022. The LOFAR Two-metre Sky Survey. V. Second data release. *A&A*, 659:A1.

Shimwell, T.W., Tasse, C., Hardcastle, M.J., et al., 2019. The LOFAR Two-metre Sky Survey. II. First data release. *A&A*, 622:A1.

Silk, J. and Rees, M.J., 1998. Quasars and galaxy formation. *A&A*, 331:L1.

Singh, V., Shastri, P., and Risaliti, G., 2011. X-ray spectral properties of Seyfert galaxies and the unification scheme. *A&A*, 532:A84.

Smith, D.J.B., Haskell, P., Gürkan, G., et al., 2021. The LOFAR Two-metre Sky Survey Deep Fields. The star-formation rate-radio luminosity relation at low frequencies. *A&A*, 648:A6.

Smolčić, V., Zamorani, G., Schinnerer, E., et al., 2009. Cosmic Evolution of Radio Selected Active Galactic Nuclei in the Cosmos Field. *ApJ*, 696(1):24.

Snellen, I.A.G., Schilizzi, R.T., Miley, G.K., et al., 2000. On the evolution of young radio-loud AGN. *Monthly Notices of the Royal Astronomical Society*, 319(2):445.

Snellen, I.A.G., Schilizzi, R.T., Miley, G.K., et al., 2000. On the evolution of young radio-loud AGN. *MNRAS*, 319(2):445.

Somerville, R.S. and Davé, R., 2015. Physical Models of Galaxy Formation in a Cosmological Framework. *Annual Review of Astronomy and Astrophysics*, 53:51.

Stroe, A., Catlett, V., Harwood, J.J., et al., 2022. The host galaxies of hybrid morphology radio sources. *The Astrophysical Journal*, 941(2):136.

Szuszkiewicz, E., Malkan, M.A., and Abramowicz, M.A., 1996. The Observational Appearance of Slim Accretion Disks. *ApJ*, 458:474.

Tadhunter, C., 2008. An introduction to active galactic nuclei: Classification and unification. *New Astronomy Review*, 52(6):227.

Tasse, C., Le Borgne, D., Röttgering, H., et al., 2008. Radio-loud AGN in the XMM-LSS field. I. Optical identification and sample selection. *A&A*, 490(3):879.

Taylor, G., Carilli, C., Perley, R., et al., 1999. *Synthesis Imaging in Radio Astronomy II*, volume 180 of *Astronomical Society of the Pacific conference series*.

Thompson, A.R., Moran, J.M., and Swenson, George W., J., 2017. *Interferometry and Synthesis in Radio Astronomy, 3rd Edition*. Springer.

Turner, R.J., Rogers, J.G., Shabala, S.S., et al., 2018. RAiSE II: resolved spectral evolution in radio AGN. *MNRAS*, 473(3):4179.

Ubertosi, F., Gitti, M., Torresi, E., et al., 2021. A Chandra study of Abell 795 – a sloshing cluster with an FR0 radio galaxy at its centre. *Monthly Notices of the Royal Astronomical Society*, 503(3):4627.

Ulrich, M.H., Maraschi, L., and Urry, C.M., 1997. Variability of active galactic nuclei. *Annual Review of Astronomy and Astrophysics*, 35(1):445.

Urry, C.M. and Padovani, P., 1995. Unified Schemes for Radio-Loud Active Galactic Nuclei. *PASP*, 107:803.

Valtonen, M.J., Lehto, H.J., Nilsson, K., et al., 2008. A massive binary black-hole system in OJ287 and a test of general relativity. *Nature*, 452(7189):851.

van Haarlem, M.P., Wise, M.W., Gunst, A.W., et al., 2013. LOFAR: The LOw-Frequency ARray. *A&A*, 556:A2.

Villarreal Hernández, A.C. and Andernach, H., 2018. A Search for Extended Radio Sources in 1.3 sr of the VLA Sky Survey (VLASS). *arXiv e-prints*, arXiv:1808.07178.

Visvanathan, N., 1969. The Continuum of BL Lac. *ApJ*, 155:L133.

Viswanath, G., Stalin, C.S., Rakshit, S., et al., 2019. Are Narrow-line Seyfert 1 Galaxies Powered by Low-mass Black Holes? *ApJ*, 881(1):L24.

Vollmer, B., Davoust, E., Dubois, P., et al., 2005. A method for determining radio continuum spectra and its application to large surveys. *A&A*, 431(3):1177.

Wang, Y., Knigge, C., Croston, J.H., et al., 2011. The entrainment-limited evolution of FR II sources: maximum sizes and a possible connection to FR Is. *MNRAS*, 418(2):1138.

Wardle, J.F.C., Moore, R.L., and Angel, J.R.P., 1984. The radio morphology of blazars and relationships to optical polarization and to normal radio galaxies. *ApJ*, 279:93.

Webster, B., Croston, J.H., Harwood, J.J., et al., 2021a. Investigating the spectra and physical nature of galaxy scale jets. *MNRAS*, 508(4):5972.

Webster, B., Croston, J.H., Mingo, B., et al., 2021b. A population of galaxy-scale jets discovered using LOFAR. *MNRAS*, 500(4):4921.

Whysong, D. and Antonucci, R., 2004. Thermal emission as a test for hidden nuclei in nearby radio galaxies. *The Astrophysical Journal*, 602(1):116.

Wilkinson, P.N., Polatidis, A.G., Readhead, A.C.S., et al., 1994. Two-sided Ejection in Powerful Radio Sources: The Compact Symmetric Objects. *ApJ*, 432:L87.

Williams, W.L., Hardcastle, M.J., Best, P.N., et al., 2019. The LOFAR Two-metre Sky Survey. III. First data release: Optical/infrared identifications and value-added catalogue. *A&A*, 622:A2.

Willis, A.G., Strom, R.G., and Wilson, A.S., 1974. 3C236, DA240; the largest radio sources known. *Nature*, 250(5468):625.

Wilman, R.J., Miller, L., Jarvis, M.J., et al., 2008. A semi-empirical simulation of the extragalactic radio continuum sky for next generation radio telescopes. *MNRAS*, 388(3):1335.

Wilson, A.S. and Colbert, E.J.M., 1995. The Difference between Radio-loud and Radio-quiet Active Galaxies. *ApJ*, 438:62.

Windhorst, R.A., Fomalont, E.B., Partridge, R.B., et al., 1993. Microjansky Source Counts and Spectral Indices at 8.44 GHz. *ApJ*, 405:498.

Windhorst, R.A., Miley, G.K., Owen, F.N., et al., 1985. Sub-millijansky 1.4 GHz source counts and multicolor studies of weak rado galaxy populations. *ApJ*, 289:494.

Woltjer, L., 1959. Emission Nuclei in Galaxies. *ApJ*, 130:38.

Wright, L., E., and et al, 2010. The Wide-field Infrared Survey Explorer (WISE): Mission Description and Initial On-orbit Performance. *AJ*, 140(6):1868.

Xiong, D., Zhang, X., Bai, J., et al., 2015. From the 'blazar sequence' to unification of blazars and radio galaxies. *MNRAS*, 451(3):2750.

Xu, D. and Komossa, S., 2010a. Low-Mass AGN at High Accretion Rates. In B.M. Peterson, R.S. Somerville, and T. Storchi-Bergmann, editors, *Co-Evolution of Central Black Holes and Galaxies*, volume 267, pages 338–338.

Xu, D. and Komossa, S., 2010b. New insights into AGNs with low-mass black holes and high accretion rates: the case of narrow-line Seyfert 1 galaxies. *Science China Physics, Mechanics, and Astronomy*, 53(1):216.

Yuan, W., Zhou, H.Y., Komossa, S., et al., 2008. A Population of Radio-Loud Narrow-Line Seyfert 1 Galaxies with Blazar-Like Properties? *ApJ*, 685(2):801.

Zhang, L., Cheng, K.S., and Fan, J.H., 2001. The Radio and Gamma-Ray Luminosi0074ies of Blazars. *Publications of the Astronomical Society of Japan*, 53(2):207.

Zinn, P.C., Middelberg, E., Norris, R.P., et al., 2012. The Australia Telescope Large Area Survey: 2.3 GHz observations of ELAIS-S1 and CDF-S. Spectral index properties of the faint radio sky. *A&A*, 544:A38.